E-140

Fermilab Library
0 1160 0023869

UR-1309
ER-40685-758

191

A Study of Electromagnetic and Hadronic Shower Shapes and Position Resolution, and the Jet Energy Response of the D-Zero Calorimeter

by

Sarah Joy Durston

UNIVERSITY OF ROCHESTER

3/93

DEPARTMENT OF PHYSICS AND ASTRONOMY

ROCHESTER, NEW YORK 14627

LIBOFFCE
FERMI
THESIS

AACOO93

Fermilab Library
0 1160 0023869 5

A Study of Electromagnetic and Hadronic Shower Shapes and Position Resolution, and the Jet Energy Response of the D-Zero Calorimeter

by

Sarah Joy Durston

Submitted in Partial Fulfillment
of the
Requirements for the Degree
Doctor of Philosophy

Supervised by
Professor Thomas Ferbel
Department of Physics and Astronomy
College of Arts and Science

University of Rochester
Rochester, New York
1993

196
AACO093
F140

To my parents

Colin and Stephanie Joy Durston

"The pursuit of truth and beauty is a sphere of activity in which we are permitted to remain children all of our lives." Albert Einstein

CURRICULUM VITAE

The author was born in Weymouth, England on October 21, 1964. She attended the State University of New York at Albany from 1982 to 1986, and graduated Summa Cum Laude with a Bachelor of Science degree in Physics in 1986. She came to the University of Rochester in the fall of 1986 and began graduate studies in Physics. She received a Rush Rhees Fellowship for 1987-1989. She pursued her research in Particle Physics under the direction of Professor Thomas Ferbel and received the Doctor of Philosophy degree in 1993.

ACKNOWLEDGMENTS

Because the D-Zero experiment is a large collaborative effort, there are many people I would like to thank, but I must also thank the United States Department of Energy who funded the research presented in this thesis. First, I would like to thank my advisor Prof. Thomas Ferbel for his guidance and first-class editing. He has taught me that every question is worth asking. I would like to thank Prof. Fred Lobkowicz for imparting his knowledge of so many topics. I also thank Profs. Ashok Das and Mark Bocko for serving on my committee.

I would like to thank the Rochester post-docs and students (past and present) with whom I have worked: Jerry Blazey, John Borders, Paul Draper, Kathy Hodel, Bob Hirosky and Betsey Pitts; especially Bob and John who made the test beam bearable. I also thank the Rochester support staff including the high energy secretaries and the guys in the Cyclotron Lab. I would like to thank Kathy Streets for her friendship and help with TeX. I am grateful to everyone in the D-Zero collaboration who made the test beam possible. I would like to thank the crew that helped me install the high voltage cabling and gave me rides while I was on crutches; especially Joan Guida with whom I proved that you could debug one CCEM module a day. I would especially like to thank Roger Dixon for his advice, sense of humor and friendship.

Special thanks go to Ottis for making sure I woke up every morning for the last year and a half. Most of all, I would like to thank Mark for his love and support. I couldn't have done it without him.

ABSTRACT

The D-Zero experiment at Fermi National Accelerator Laboratory examines proton-antiproton collisions at a center of mass energy of 1.8 TeV. An analysis of the response of the D-Zero calorimeter to single electrons and pions has been performed. The data were obtained from beam tests performed on end calorimeter modules between May and August of 1990.

The shapes of electromagnetic and hadronic energy showers were as expected, and agreed with Monte Carlo simulations of the detector. Many methods were investigated to determine the transverse position of the centroid of a particle shower. A corrected-center-of-gravity method gave good results for electromagnetic showers. For hadronic showers, the best algorithm for determining shower centroid position was a center-of-gravity type of calculation with specific weights using all the longitudinal layers of the calorimeter. In both the electromagnetic and hadronic case, the magnitudes of optimized readout tower thresholds indicated that the tails of the transverse energy distributions could be ignored in calculations of position. The energy dependence of the electromagnetic position resolution was found to be $\sigma(r \cdot \phi) = (17.9 \pm 0.4)E^{-0.685 \pm 0.005}$ mm and of the hadronic position resolution was $\sigma(r \cdot \phi) = (54.9 \pm 1.3)E^{-0.551 \pm 0.005}$ mm. The energy dependence of the hadronic position resolution in the current D-Zero Monte Carlo does not follow the idealized $E^{-1/2}$ behavior. The angular dependence of the position resolution was as expected.

The energy response for jets in the D-Zero calorimeter can be estimated from the energy response of the calorimeter to single particles, convoluted

with the particle content of jets. The transverse energy of jets calculated by summing simulated single particles reproduced the energy dependence for jets produced in the calorimeter using the event generator ISAJET. To use test-beam data as input for calculating the jet energy expected in the collider environment, the Monte Carlo will have to be tuned to match the test beam data, a reliable simulation of jet fragmentation must be found, and effects due to energy leakage in and out of the jet cone must be measured in each event.

TABLE OF CONTENTS

List of Tables x

List of Figures xii

CHAPTER 1: INTRODUCTION 1

1.1 The Standard Model and Beyond 2

1.2 High Energy Collisions 5

1.3 Recent Results from Colliders 10

CHAPTER 2: GOALS OF THE D-ZERO PHYSICS PROGRAM AND A GENERAL DESCRIPTION OF THE D-ZERO DETECTOR 20

2.1 Physics Goals 20

2.1.1 Detection of Charged Leptons 21

2.1.2 Detection of Hadronic Jets 22

2.1.3 Detection of Missing Transverse Energy 23

2.2 The D-Zero Detector 25

2.2.1 The Central Tracking System 27

2.2.2 The Muon Tracking System 30

2.2.3 The Calorimeters 33

CHAPTER 3: CALORIMETRY AND PARTICLE SHOWERS 39

3.1 Calorimeter Design 40

3.1.1 Purpose of Calorimetry 40

3.1.2 Sampling vs Homogeneous Calorimeters 40

3.2 Electromagnetic Calorimetry 41

3.2.1 Electromagnetic Interactions 41

3.2.2 Characteristics of Electromagnetic Showers 44

3.2.3 Electromagnetic Energy Resolution 48

3.2.4 Electromagnetic Position Resolution 50

3.3 Hadronic Calorimetry 51

3.3.1 Hadronic Interactions 51

3.3.2 Characteristics of Hadronic Showers 56

3.3.3 Hadronic Energy Resolution 59

3.3.4 Hadronic Position Resolution 62

3.4 D-Zero Calorimetry 64

CHAPTER 4: DESCRIPTION OF THE EXPERIMENTAL APPARATUS AT THE TEST BEAM 67

4.1 The Calorimeter Modules 68

4.2 The Neutrino West Beamline 76

4.3 The Cryostat and Transporter 80

4.4 The Electronics 84

4.5 The Data Acquisition System 89

4.6 Detector Calibration 93

CHAPTER 5: ANALYSIS OF SHOWER SHAPES AND POSITION RESOLUTION 97

5.1 Analysis of the Shape of Electromagnetic Showers 98

5.1.1 Longitudinal Shape of Electromagnetic Showers 99

5.1.2 Transverse Shape of Electromagnetic Showers 103

5.1.3 Methods for Determining Transverse

Electromagnetic Position 106

5.1.4 Results for Electromagnetic Position Resolution 109

5.1.5 Conclusions 117

5.2 Analysis of the Shape of Hadronic Showers 118

5.2.1 Longitudinal Shape of Hadronic Showers 119

5.2.2 Transverse Shape of Hadronic Showers 121

5.2.3 Methods for Determining Transverse Hadronic Position 130

5.2.4 Results for Hadronic Position Resolution 134

5.2.5 Conclusions 147

CHAPTER 6: ANALYSIS OF JET ENERGY RESPONSE 150

6.1 Energy Response to Single Particles 153

6.1.1 Response of the Monte Carlo 153

6.1.2 Transverse Energy Bias 154

6.1.3 Response of the Test Beam Data 167

6.2 Single Particle Content of Jets 170

6.3 Jet Energy Response 171

CHAPTER 7: CONCLUSIONS 181

7.1 Shower Shapes and Position Resolution 181

7.2 Jet Energy Response 183

REFERENCES 185

APPENDIX A: Monte Carlo Simulations 192

A.1 Event Simulation 192

A.2 Detector Simulations 193

A.2.1 Simulation of Test Beam Measurements 194

A.2.2 Simulation of the Full D-Zero Detector 195

LIST OF TABLES

1.1	First Order Parton Sub-processes	9
1.2	Experimental Masses of Gauge Bosons	15
1.3	Experimental Widths of Gauge Bosons	16
1.4	Experimental Measurements of $\sin^2 \theta_W$	16
1.5	Experimental Limits on Top Quark Mass	18
3.1	Characteristic Properties of the Hadronic Cascade	53
4.1	Calorimeter Depths in Radiation and Absorption Lengths	73
4.2	Ranges of Motion of the 1990 Test Beam Transporter	82
4.3	Change in α and β Test Cell Response During the 100 Day Run	84
5.1	Electromagnetic Position Resolution at $\eta = 1.95$	117
5.2	Parameters for Convoluted Double Exponential Fit to Transverse Hadronic Shower Shape	127
5.3	Parameters for Modified Lorentzian Fit to Transverse Hadronic Shower Shape	128
5.4	Hadronic Azimuthal Position Resolution at $\eta = 2.55$	137
5.5	Hadronic Radial Position Resolution at $\eta = 2.55$	138
5.6	Estimated Optimum Tower-Energy Threshold Values	140
5.7	Hadronic Azimuthal Position Resolution at $\eta = 2.55$ in the Monte Carlo	145
5.8	Hadronic Radial Position Resolution at $\eta = 2.55$ in the Monte Carlo	146
6.1	Parameters for Fits to Single-Particle Energy Response in the Monte Carlo	164

6.2 Parameters for Fits to Single-Particle Transverse Energy Response in the Monte Carlo 165

6.3 Parameters for Fits to Single-Particle Energy Response in the Monte Carlo R=0.7 Cone Imposed 166

6.4 Parameters for Fits to Single-Particle Transverse Energy Response in the Monte Carlo R=0.7 Cone Imposed 166

6.5 Parameters for Fits to Single-Particle Energy Response in the Test Beam 170

6.6 Parameters for Fits to Single-Particle Content of Jets (E dN/dE) from ISAJET 174

LIST OF FIGURES

1.1 Quark and gluon distribution functions at $q^2 = 10GeV^2$ [5] 7

1.2 Feynman diagrams contributing to lowest order parton-parton scattering 8

1.3 The production cross section for a variety of $p\bar{p}$ physics processes plotted as a function of p_T (transverse momentum) of the hard scattering system. As expected, jet production dominates by several orders of magnitude [7]. 11

1.4 Typical strong, electromagnetic and weak processes in hard $p\bar{p}$ collisions, and their interpretation in terms of typical parton-parton scattering diagrams 12

1.5 The measured inclusive jet cross section plotted as a function of E_{Tjet}. Superimposed is a fit using NLO (next-to-leading order, α_s^3) QCD calculations of Ellis et al. [4]. 14

1.6 Diagrams for the decay of $W^{\pm}$ and Z^0 into two leptons 15

1.7 Diagrams for the decay of $t\bar{t}$ 17

1.8 Diagrams of contact interactions that would increase the jet production cross section 19

2.1 The coordinate system of D-Zero 24

2.2 An overview of the D-Zero detector indicating the location of the different detection systems 26

2.3 Cross-sectional view of the central detector, including the forward drift chambers is shown. This is one quarter of the whole detector. 28

2.4 A sketch of the D-Zero dectector spread apart to see the details of the muon tracking system 32

2.5 The modules that comprise the D-Zero central and end calorimeters 34

2.6 The composition of the basic sampling cell of a calorimeter module 37

2.7 A cross-sectional view of the central and end calorimeters 38

3.1 The cross sections for pair production, Compton scattering and photo-electric effect, as a function of photon energy (a-c) and the fractional energy loss by radiation and ionization as a function of electron energy (d-f) [24,25] 43

3.2 The longitudinal shower development (left scale) of 6 GeV/c electrons shows scaling in units of radiation length. On the right, the shower radius for 90% energy containment is plotted as a function of depth [26]. 46

3.3 The lateral distribution of the energy deposited by a 1 GeV e.m. shower in lead at various depths is shown. These are results of an EGS4 Monte Carlo calculation [22]. 48

3.4 Relative contributions of the most important processes to the energy dissipated by hadronic showers as evaluated from three Monte Carlo calculations [33] 55

3.5 Hadron longitudinal shower development (left scale) showing approximate scaling in absorption length is shown, as well as transverse hadronic distributions as a function of shower depth (right scale) [26]. 57

3.6 The leakage as a function of detector depth for 5-210 GeV pions as measured in a uranium/plastic scintillator calorimeter [22]. 58

3.7 The e/h ratio for uranium calorimeters as a function of the ratio of the thicknesses of absorber and readout layers [37] 65

4.1 The arrangment of the modules within the cryostat 69

4.2 The End Calorimeter Electromagnetic Module (ECEM) 71

4.3 The End Calorimeter Inner Hadronic Module (ECIH) and the End Calorimeter Middle Hadronic Module (ECMH) in the D-Zero cryostat 75

4.4 A schematic of the NWA beamline 77

4.5 A sketch of the test-beam cryostat and transporter

4.6 Outline of the instrumented region of the ECEM and ECIH 85

4.7 A flow diagram of the D-Zero data acquisition system 92

4.8 A schematic of the pulser input to the calorimeter preamp 94

5.1 Distribution of energy in ECEM layers 1-4 and ECIH layer 1 and the total energy in the ECEM and ECIH layer 1 combined for 100 GeV electrons at $\eta = 2.3$ and $\phi = 3.0$ rad. 100

5.2 $\langle E_{layer}\rangle/\langle E_{total}\rangle$ plotted as a function of energy for ECEM layers 1-4 at $\eta = 2.3$. The asterisks are data and the open squares are from a fit to the data that is described in the text. 101

5.3 The longitudinal shower shape for 50 GeV electrons at $\eta = 1.95$ as a function of depth in the calorimeter. The asterisks are data and the open triangles are the results of a Monte Carlo simulation. 103

5.4 The pad layout of a 22.5° multilayer signal board in ECEM layer 3 showing r-ϕ segmentation. 104

5.5 Transverse profile for 50 GeV electron showers in ECEM layer 3. The points are data and the histogram represents a Monte Carlo simulation [44]. 105

5.6 The difference between the impact position x_0 and the estimated position $\bar{x}$, $x_0 - \bar{x}$, and the difference between x_0 and the corrected position x_{ccog}, $x_0 - x_{ccog}$, plotted as a function of $x_0 - x_{edge}$, where x_{edge} is the pad edge closest to x_0. 107

5.7 The position resolution for 75 GeV electrons entering the ECEM at a pseudorapidity of $\eta = 1.95$. The Gaussian fit has a mean of $\mu = -.009 \pm 0.014$ mm and a standard deviation 1.03 ± 0.01 mm. 110

5.8 The electromagnetic position resolution plotted as a function of energy for the corrected-center-of gravity method with the three sets of parameters given in the legend. The dotted line is a fit to the resolution obtained using the optimized parameter set (asterisks) for the phenomenological form $\sigma(r \cdot \phi) = (17.9 \pm 0.4)E^{-0.685\pm0.005}$ mm. 112

5.9 Optimized values of corrected-center-of-gravity parameters S and threshold cut, τ, plotted as functions of energy. The fits are those given in Eqs. (5.10) and (5.11). 114

5.10 Optimized values of corrected-center-of-gravity parameters plotted as a function of pseudorapidity η. The arrow indicates where the calorimeter tower size changes from $\Delta\eta \times \Delta\phi = 0.05 \times 0.05$ to 0.1×0.1. 115

5.11 The position resolution for electromagnetic showers is plotted as a function of pseudorapidity for the corrected-center-of-gravity method using two sets of parameters. One from the values obtained at $\eta = 1.95$ and the other optimized at each energy. 116

5.12 The energy distributions in five longitudinal layers of the calorimeter and the total energy deposited in the ECEM and ECIH combined for a 150 GeV pion run at $\eta = 2.55$ and $\phi = 3.0$ rad. 120

5.13 Longitudinal development of pion showers at four energies. The results from the data and Monte Carlo simulation are compared with the parametrization of Eq. (3.6) [52]. 121

5.14 The transverse hadronic shower shape in ECEM layers 1-4, $x = |x_i - x_0|$. The dotted line is the convoluted double exponential fit and the solid line is the modified Lorentzian fit, both described in the text. 124

5.15 The transverse hadronic shower shape in ECIH layers 1-5, $x = |x_i - x_0|$. The dotted line is the convoluted double exponential fit and the solid line is the modified Lorentzian fit, both described in the text. 125

5.16 The first and second terms in the modified Lorentzian fit to the transverse shower shape plotted separately. 126

5.17 Modified Lorentzian fits to the transverse shower shape seen in the data (solid line) and the Monte Carlo (dotted line). 129

5.18 E_R/E_T plotted as a function of impact position $x = x_0 - x_{edge}$ for four calorimeter layers. The solid line is a double exponential fit and the dotted line is the curve from the convoluted double exponential parameters. 131

5.19 The position resolution determined using two methods for 150 GeV pions entering at a pseudorapidity of $\eta = 2.55$. For the method using only one longitudinal layer, the Gaussian fit has a mean of $\mu = .01 \pm 0.05$ mm and a standard deviation 4.49 ± 0.06 mm; using all the layers the Gaussian fit has a mean of $\mu = -.13 \pm 0.04$ mm and a standard deviation 3.80 ± 0.04 mm. 135

5.20 Hadronic position resolution as a function of threshold cut T. Typical results are plotted for both the radial and azimuthal coordinate. 141

5.21 The azimuthal and radial hadronic position resolution plotted as a function of energy for data and for Monte Carlo. The dashed lines are best fits to the data, and the dotted lines are best fits to the Monte Carlo for the case when all layers are used in the calculation of position. 144

5.22 The radial and azimuthal hadronic position resolution plotted as a function of energy, with $T = T(\eta = 2.55)$ at $\eta = 2.55$ and $T = 1.7 \cdot T(\eta = 2.55)$ at $\eta = 2.30$. 148

6.1 The systematic uncertainty in jet energy for the CDF experiment. The total and the contributions from different sources are shown separately. 152

6.2 The ratios of reconstructed to incident single-particle total energies and transverse energies for electrons obtained in the Monte Carlo. 155

6.3 The ratios of reconstructed to incident single-particle total energies and transverse energies for pions obtained in the Monte Carlo. 156

6.4 If a hadron shower is circularly symmetric, a particle entering the end calorimeter at an angle θ deposits more energy outside the arc of constant θ than inside it. 157

6.5 The integration of the deposited energy over the extent of a particle shower. 159

6.6 The bias in transverse energy due to shower size, shown as a function of $|\eta|$, for simulated 50 GeV pions without a cone restriction, with a cone of R=0.7 and calculated using Eq. 6.4. 160

6.7 The fractional difference between the reconstructed energy in D-Zero obtained with (E_J) and without (E_R) a cone of R=0.7 imposed for simulated 4 GeV and 50 GeV pion showers, shown as a function of $|\eta|$. 162

6.8 The results for and fits to, $R_{E_T}(E)$ for pions generated in the Monte Carlo. 163

6.9 The arrangement of calorimeter modules in the 1991 test beam. 168

6.10 Fits to the ratios R(E) for the Monte Carlo events at $|\eta| = 0.3$, and for test-beam data at $\eta = .45$, for both pions and electrons. 169

6.11 Fragments of jets and fits to the inclusive single-particle content (E dN/dE) for electromagnetic particles fragmenting from 50 GeV E_T jets in five pseudorapidity regions. 172

6.12 Fragments of jets and fits to the inclusive single-particle content (E dN/dE) for hadronic particles fragmenting from 50 GeV E_T jets in five pseudorapidity regions. 173

6.13 R_{JMC} and R_{JMC_T} as a function of $|\eta|$, with and without an imposed cone requirement. 176

6.14 A comparison of the calculated jet transverse energy response in the Monte Carlo with that measured for jets created by ISAJET. 177

6.15 A comparison of the jet energy response calculated from the test-beam single particle response with the response calculated from the Monte Carlo. 178

FOREWORD

The D-Zero experiment is a collaborative effort involving over 300 physicists and students from 36 institutions. The University of Rochester group has been involved in several aspects of the construction and running of the experiment. These include being responsible for the design, construction and installation of the liquid argon purity and temperature monitoring system, making significant contributions to both the 1990 and 1991 single particle beam tests and being deeply involved in the analysis conducted by D-Zero's quantum chromodynamics (QCD) group.

I worked on several different projects besides the analyses presented in this thesis. I was responsible for the design and installation of the D-Zero central calorimeter high voltage cabling. I also made contributions to the design of the high voltage filter and shielded conduit system. I worked as part of the team that debugged and installed the central calorimeter modules. My largest contribution was to the 1990 test beam where I was in charge of the entire high voltage supply and monitoring system. I also worked on various other hardware and software projects such as the monitoring of the temperatures of the electronics, assuming the role of data-taking shift captain and analyzing the affects of pile-up on the energy resolution. Another of my projects has been the analysis of Monte Carlo data as a member of D-Zero's QCD group.

CHAPTER 1

INTRODUCTION

Elementary particle physics concerns the study of the constituents of matter and how they interact. The basic method employed to study such issues involves a scattering experiment. Large particle accelerators and correspondingly large detectors are the tools used in experimental particle physics. Collider experiments, where two beams of particles interact, and fixed target experiments, where a beam collides with a stationary target, constitute the majority of particle physics experiments. The field is also known as high energy physics because it is necessary to accelerate particles to high energies in order to investigate the very small distance scales associated with elementary particles. Very small distances can only be probed by radiation of a comparably small wavelength and high energy. Large energies are also necessary to create and examine the fundamental constituents because many of them have large masses. Collider experiments have an advantage over fixed target experiments in that high center of mass energies are easier to attain with two colliding beams.

This dissertation concerns the D-Zero experiment at the Fermilab proton-antiproton collider. In particular, it concerns beam tests performed on several detector components in the Neutrino-West beamline, Building A, at Fermilab,

between May and August 1990. These beam tests were performed to calibrate the energy and other characteristics of three end-calorimeter modules, which have since been installed in the D-Zero detector. The calorimeter is the detector element in D-Zero that measures the energy of particles. These studies involved the illumination of calorimeter modules at various orientations relative to electron, pion and muon beams, over a momentum range of 10-150 GeV/c. The work presented here involves an analysis of the response of the D-Zero calorimeters to pions and electrons. In addition to investigating the characteristics of the resulting individual energy deposit signatures known as "showers", we also include a study of what can be inferred about the energy response of the calorimeters to hadronic "jets" of particles, which are important signals in the collider environment; the latter is based upon the energy response to single particles observed in these beam tests.

This introduction covers a brief discussion of the Standard Model of particle physics, the physics of high energy collisions and a short survey of recent results from proton-antiproton collisions. Chapter 2 details the physics goals of D-Zero, and provides a general description of the D-Zero detector. The physics of particle showers and the ideas behind calorimetry, and the D-Zero calorimeter in particular, are described in Chapter 3. A description of the experimental configuration and properties of the test beam are contained in Chapter 4. The data analysis and results from the beam tests are presented in Chapters 5 and 6. Chapter 7 contains the conclusions reached from this analysis.

1.1 The Standard Model and Beyond

The Standard Model of particle physics has recently emerged as the guiding theory of weak, electromagnetic and strong interactions. It includes the Glashow-Weinberg-Salam (GWS) model of the unified weak and electromagnetic forces (electroweak theory) and the theory of quantum chromodynamics (QCD), which involves interactions of quarks and gluons. In the standard model, all matter is composed of three types of elementary particles: quarks, leptons and force mediators. The six flavors of quarks are classified by their quantum numbers such as charge, strangeness, charm, bottom and top flavor content. They can be grouped into three "generations", and all have antiquark partners with quantum numbers of opposite sign. Quarks also possess a color "charge" that can take on three values. This degree of freedom is necessary if the fermionic quarks are to describe the structure of hadrons, and be subject to the Pauli exclusion principle. Only colorless hadrons have ever been observed in nature: baryons that are made up of three different colored quarks, and mesons that are made up of a quark-antiquark pair. The leptons and antileptons can also be grouped into three generations: the electron, muon and tau families.

The force mediators of the standard model consist of the photon for the electromagnetic force, W^+,W^- and Z^0 for the weak force, gluons for the strong force and the graviton (as yet to be detected) for gravity. The W and Z gauge bosons were discovered at CERN in 1982, confirming the GWS theory of electroweak interactions [1]. A proposed mechanism, called the Higgs mechanism, is invoked to understand the masses of these bosons. In this pro-

posal, a massive scalar boson, called the Higgs, provides the mass through a process called spontaneous symmetry breaking [2]. There is at present no evidence for the existence of the Higgs boson. Also, there are 28 free parameters (e.g. coupling constants, masses of the W,Z etc.) in the standard model that cannot be evaluated from first principles, so the model is far from complete. One of the most perplexing aspects of the model is the difference observed in various mass scales. The electroweak theory can be characterized by the W and Z masses of ≈ 100 GeV/c^2, while the scale for leptons is ≤ 1 GeV/c^2. In comparison, the simplest Grand Unification Theories (GUTs) which unify quarks and leptons, have mass scales of the order of 10^{15}GeV/c^2. Thus, if the strong and electroweak theories have a common origin, an idea that is very appealing, one would be hard-pressed to explain how mass-generating mechanisms could yield fundamental particles with the small observed mass values from term cancellations to 15 decimal places.

Grand Unification theories go beyond the standard model to account for the disparate strengths and properties of the four fundamental interactions (strong, electromagnetic, weak and gravity) that are observed at low energies, but which would disappear at the scale of 10^{15} GeV. The most interesting models for the grand unification of the first three forces involve an additional symmetry known as supersymmetry. This symmetry would be broken in a fashion similar to the breaking of the electroweak symmetry, but at the energy scale of 10^{15} GeV, resulting in different coupling strengths for the different forces at lower energies. At the unification scale, the three forces would have equal couplings. Supersymmetry (SUSY) involves a symmetry between fundamental fermions and bosons. For every fermion there is a bosonic partner,

with the same couplings, and likewise for every boson there is a fermionic partner. These supersymmetric partners are expected to have masses on the order of 1 TeV/c^2, and provide cancellations in the radiative corrections to the masses of the Higgs, W and Z in the electroweak sector [2]. In most models, the new particles would be produced in pairs, with a new quantum number R (+1 for natural particles, -1 for SUSY particles). At least one of these superpartners, the lightest, must be stable because of this R symmetry; this is most likely the superpartner of the photon, or the photino. There is no experimental evidence of SUSY particles to date although lower limits of $\sim$ 150 GeV/c^2 exist on their masses [3]. Hopefully, supersymmetry and other GUT ideas can eventually be shown to provide the reason for the great success of the standard model.

1.2 High Energy Collisions

The aspects of the standard model that D-Zero expects to examine are quite numerous and varied. The events with the largest cross sections ("minimum bias" events) involve phenomena referred to as low transverse momentum (p_T) physics. Topics of general interest include elastic and diffractive scattering, studies of multiparticle production and the possible formation of quark-gluon plasma. The events which comprise a very small fraction of the total cross section, involving large p_T (hard scattering), are the ones of interest to D-Zero. Such rare hadronic processes have to do with constituent interactions, and are likely to be the ones to provide important surprises, particularly if there are departures from the standard model. These are also the processes that can be calculated through perturbative QCD, and are therefore

relatively well understood.

Over the past several decades, a lot of work has gone into probing the inner structure of nucleons; for example, by scattering leptons off nucleon targets. These "deep inelastic scattering" experiments have been used to determine the momentum distribution of the constituents within the nucleon. Typical results of such experiments are given in Fig. 1.1. In this figure, distribution functions for gluons, up and down valence quarks (in neutrons and protons) and sea quarks are shown as a function of x, the fraction of momentum carried by each type of parton. These distributions change with the hardness of scattering (q^2) because of scaling violations expected in quantum chromodynamics (QCD). QCD provides an evolution of the structure functions with q^2. Since the evaluation of this evolution in QCD is non-perturbative, the Altarelli-Parisi equations are used to evolve the structure functions to the appropriate q^2 values [2,4]. QCD is characterized by the coupling constant α_s (that governs quark and gluon interactions), which is also a function of q^2. $\alpha_s(q^2)$ is known as a running coupling constant. Because of the non-Abelian nature of QCD, gluons produce an antishielding effect that causes α_s to decrease as q^2 increases. This effect is referred to as asymptotic freedom, a situation where quarks at large q^2 behave as though they were weakly coupled free particles.

To calculate any particular hadron-hadron hard scattering process, one needs to know the parton distribution functions and the appropriate elementary (point-like) parton-parton cross section. From dimensional analysis [6] one gets that the cross sections for elementary subprocesses must be proportional to $\alpha_s^2/\hat{s}$, where α_s is the strong coupling constant, and $\hat{s}$ is the square of

the energy in the parton-parton collision center of mass. (The coupling constant appears squared because the process has two strong vertices separated by a propagator.) The typical cross section for such subprocesses at $\sqrt{s} = 100$ GeV is about 0.5 nanobarns. Many cross sections for such hard scattering reactions have been tabulated in a recent review[2].

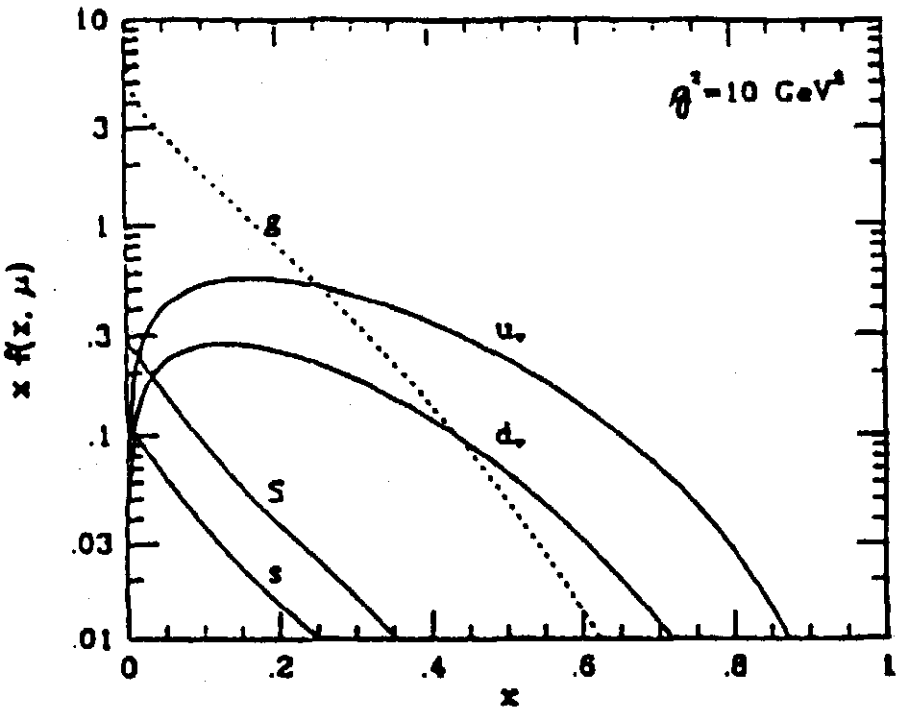

Figure 1.1 Quark and gluon distribution functions at $q^2 = 10\ GeV^2$ [5]

One of the most important hard scattering processes at the Fermilab Tevatron is jet production. High energy jets of hadrons are produced when a parton from one proton scatters elastically off a parton from the antiproton. The partons then "dress" themselves into two jets of hadrons in a pro-

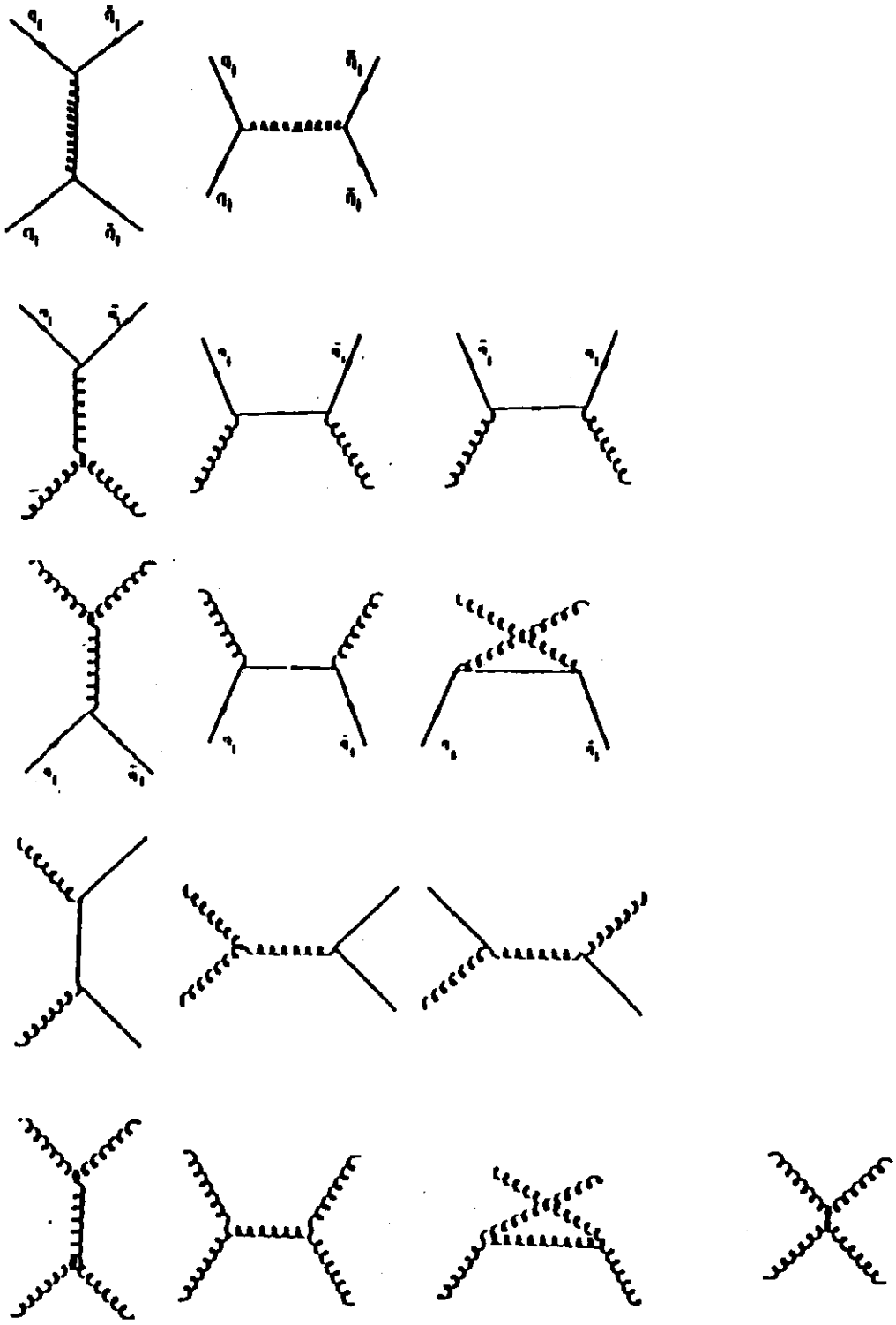

Figure 1.2 Feynman diagrams contributing to lowest order parton-parton scattering

Table 1.1

First Order Parton Sub-processes

Process	$\Sigma\lvert M\rvert^2$	$\Sigma\lvert M\rvert^2$ $\theta^*=\frac{\pi}{2}$
$qq' \to qq'$	$\frac{4}{9}\frac{s^2+u^2}{t^2}$	2.22
$qq \to qq$	$\frac{4}{9}\left(\frac{s^2+u^2}{t^2}+\frac{s^2+t^2}{u^2}\right)-\frac{8}{27}\frac{s^2}{ut}$	3.26
$q\bar{q} \to q'\bar{q}'$	$\frac{4}{9}\frac{t^2+u^2}{s^2}$	0.22
$q\bar{q} \to q\bar{q}$	$\frac{4}{9}\left(\frac{s^2+u^2}{t^2}+\frac{t^2+u^2}{s^2}\right)-\frac{8}{27}\frac{u^2}{st}$	2.59
$q\bar{q} \to gg$	$\frac{32}{27}\frac{t^2+u^2}{tu}-\frac{8}{3}\frac{t^2+u^2}{s^2}$	1.04
$gg \to q\bar{q}$	$\frac{1}{6}\frac{t^2+u^2}{tu}-\frac{3}{8}\frac{t^2+u^2}{s^2}$	0.15
$gq \to gq$	$-\frac{4}{9}\frac{s^2+u^2}{su}+\frac{u^2+s^2}{t^2}$	6.11
$gg \to gg$	$\frac{9}{2}\left(3-\frac{tu}{s^2}-\frac{su}{t^2}-\frac{st}{u^2}\right)$	30.4

2-to-2 parton sub-processes. $|M|^2$ is the squared invariant matrix element. The color and spin indices are averaged (summed) over initial (final) states. All partons are assumed massless. The scattering angle in the center-of-mass frame is denoted by $\theta^* = \pi/2$, t = u = -s/2 [4].

cess called hadronization or fragmentation. This elastic scattering can occur through exchange in the $\hat{t}$ channel, $\hat{u}$ channel, or the direct $\hat{s}$ channel (See Fig. 1.2). The contributions from each of these sub-processes is given in Table 1.1 [4]. The inclusive cross section for any particular process can be written as:

$$E\frac{d^3\sigma}{dp^3} = \sum_{ij} \int dx_1 dx_2 f_i(x_1, q^2) f_j(x_2, q^2) |M|^2 \frac{\alpha_s^2(q^2)}{\hat{s}}$$

where the subscripts i and j indicate the type of incoming parton, $f_i(x_1, q^2)$ is the parton distribution function for parton type i, and the matrix element $|M|^2$ is evaluated according to QCD. At collider energies, gluon-gluon and gluon-quark scattering dominate. The production cross sections for other interesting proton-antiproton processes, such as direct photon production, vector boson production, top quark production etc, are smaller by two or more orders of magnitude as can be seen in Fig. 1.3.

1.3 Recent Results from Colliders

The CDF (Collider Detector at Fermilab) experiment is the only other experiment besides D-Zero to examine the hard scattering of protons on antiprotons at the Fermilab Tevatron. The D-Zero detector was built to compliment the CDF detector and so maximize the opportunities that can be gained from looking at collisions at 1.8 TeV. CDF has already completed two data-taking runs at the Tevatron for a total integrated luminosity of $L = \int \mathcal{L} dt \geq 5pb^{-1}$. The now completed UA1 and UA2 experiments at the CERN proton-antiproton collider achieved total integrated luminosities of 7.8 and 13 pb^{-1}, respectively. The CERN collider had a center of mass energy of 630 GeV. A short summary of recent results from these experiments will

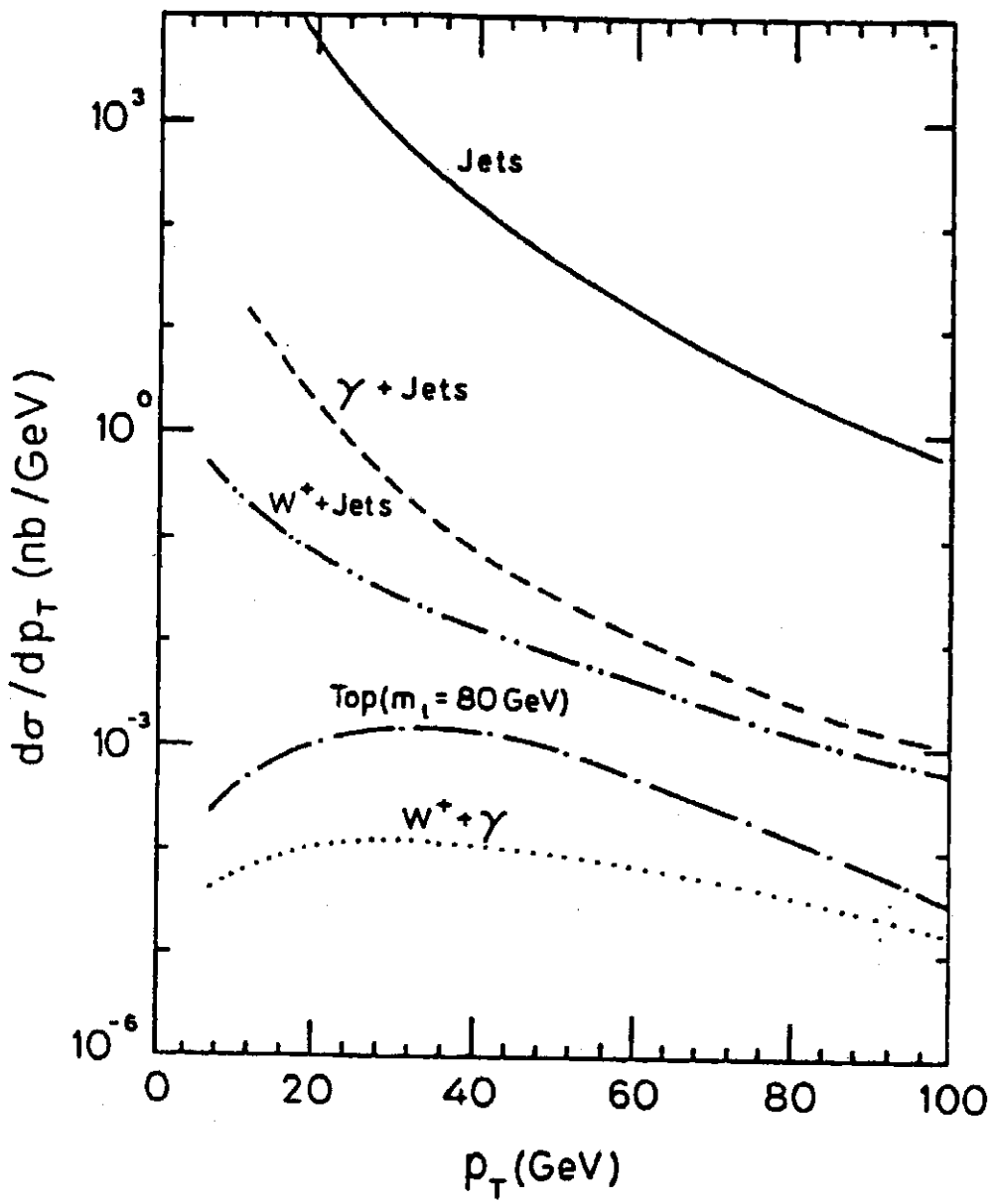

Figure 1.3 The production cross section for a variety of $p\bar{p}$ physics processes plotted as a function of p_T (transverse momentum) of the hard scattering system. As expected, jet production dominates by several orders of magnitude [7].

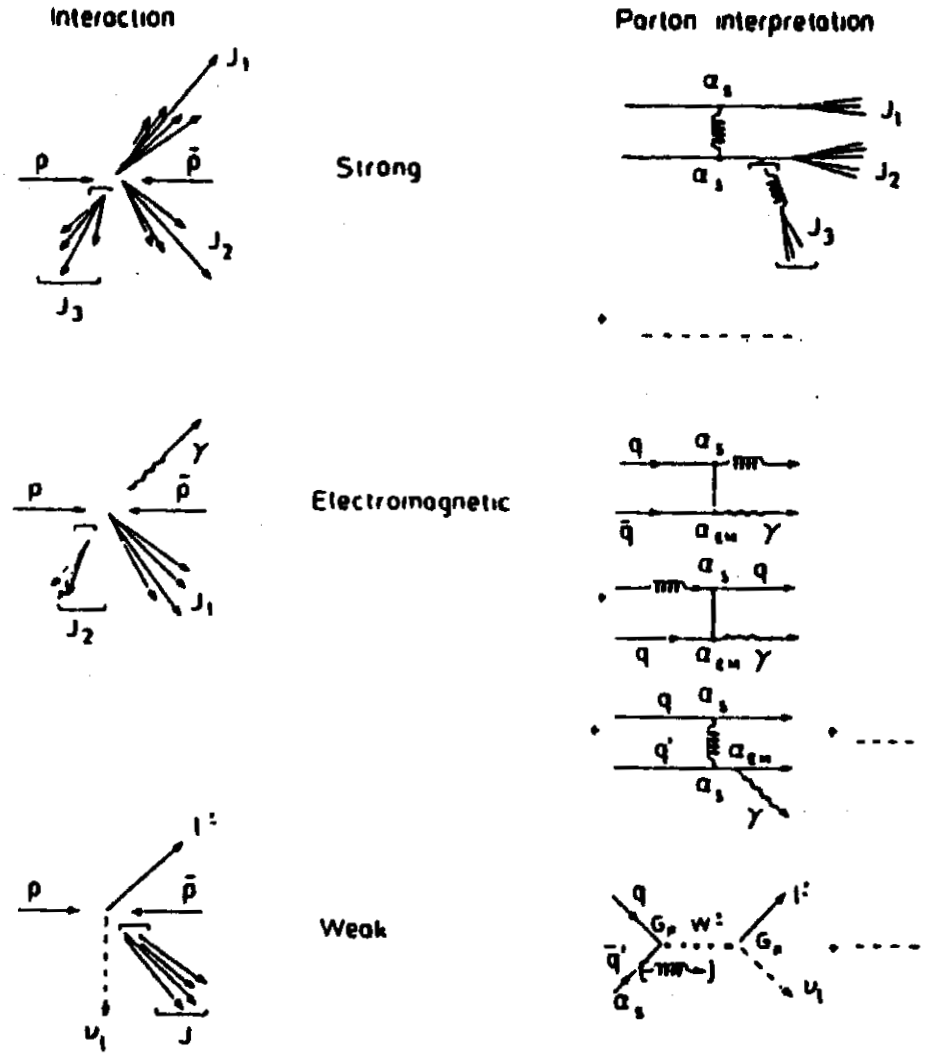

Figure 1.4 Typical strong, electromagnetic and weak processes in hard $p\bar{p}$ collisions, and their interpretation in terms of typical parton-parton scattering diagrams.

be presented below. D-Zero plans to perform similar analyses of its upcoming data.

There are many different processes that can be studied in hard proton-antiproton collisions. Figure 1.4 shows examples of typical strong, electromagnetic and weak processes that occur. The properties of hadronic jet production are studied in proton-antiproton colliders to understand how well the data agrees with the theory of quantum chromodynamics that governs the interactions of quarks and gluons. CDF has measured the inclusive jet production cross section for a transverse energy (E_{Tjet}) range of 30 GeV to 400 GeV with an estimated overall uncertainty of $\leq$ 36%. (The transverse energy is defined as the energy flow perpendicular to the beam direction.) See Fig. 1.5. The result agrees very well with a QCD calculation of order α_s^3 [8], that uses a range of structure function parametrizations for the proton and antiproton [9]. UA1 and UA2 have measured the value of the strong coupling constant by examining the ratio of the observed cross sections for three and two jet events. The cross section for the production of three jets is reduced by a factor of α_s compared to that for two jets, because of the three strong vertices present. Their results are:

$$UA1: \quad \alpha_s = 0.22 \pm 0.02 \pm 0.03 \quad at \quad \langle q^2 \rangle \sim 4000 \quad GeV^2 \ [10]$$

$$UA2: \quad \alpha_s = 0.23 \pm 0.01 \pm 0.04 \quad at \quad \langle q^2 \rangle \sim 1700 \quad GeV^2 \ [11]$$

These hadron collider experiments have also measured the masses and widths of the intermediate vector bosons, $W^{\pm}$ and Z^0. These measurements were based on events where the bosons decay into two leptons. Diagrams for

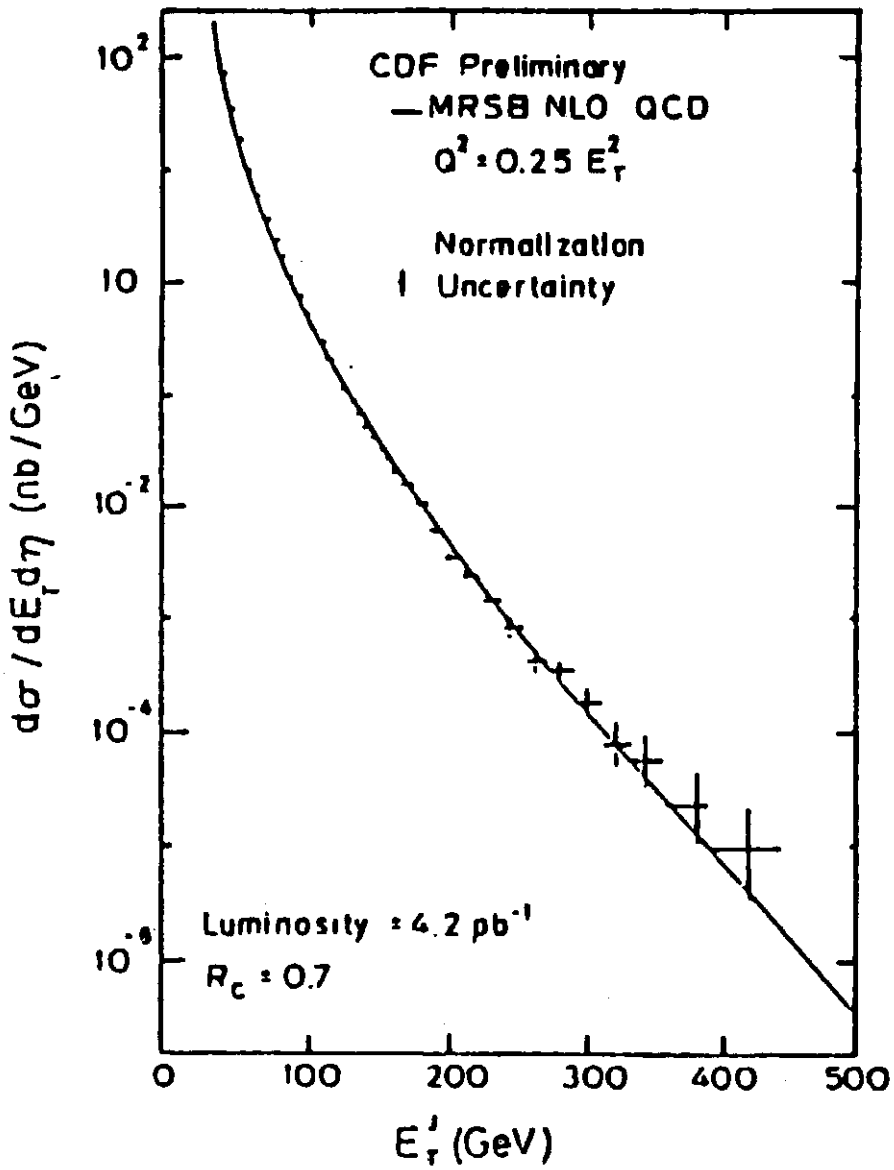

Figure 1.5 The measured inclusive jet cross section plotted as a function of E_{Tjet}. Superimposed is a fit using NLO (next-to-leading order, α_s^3) QCD calculations of Ellis et al. [4].

these processes are shown in Fig. 1.6. Although restricting the analysis to the lepton channels reduces the statistics, the channels that include jet decays of the vector bosons have large backgrounds from QCD multi-jet events and so are more difficult to handle. The results for the masses are given in Table 1.2 and the widths in Table 1.3. Also presented are the Z results from the LEP (large electron-positron) collider at CERN. The hadron collider data cannot compete with LEP's measurement accuracies for the Z, but they are important because the measurements of (M_W/M_Z) required to evaluate the value of $\sin^2\theta_w$. The electroweak mixing angle, θ_w, one of the parameters of the electroweak theory, is defined as $\cos\theta_w = M_W/M_Z$ The values for $\sin^2\theta_w$ from UA2, CDF and LEP (from the leptonic decay width for Z) are shown in Table 1.4, and compared with the recent world average [12] derived from electron-positron collider experiments not performed at LEP.

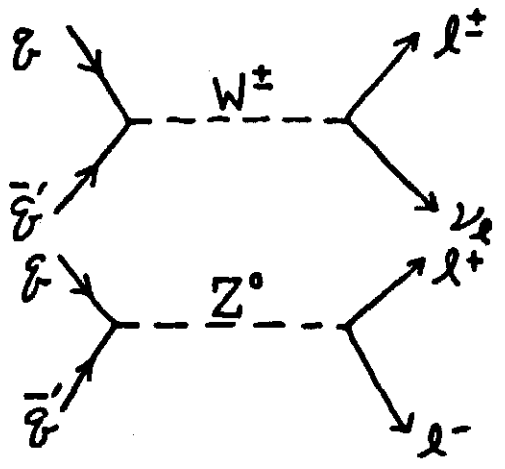

Figure 1.6 Diagrams for the decay of $W^\pm$ and Z^0 into two leptons

Table 1.2 Experimental Masses of Gauge Bosons

Experiment	M_Z (GeV)	M_W (GeV).
UA2	$91.49 \pm 0.35(stat)$	$80.79 \pm 0.31(stat)$
	$\pm 0.12(sys) \pm 0.92(scale)$	$\pm 0.21(sys) \pm 0.81(scale)$
CDF	$91.37 \pm 0.34(stat)$	$79.91 \pm 0.35(stat)$
	$\pm 0.24(sys + scale)$	$\pm 0.24(sys) \pm 0.19(scale)$
LEP	$91.161 \pm 0.031(scale)$	

Table 1.3 Experimental Widths of Gauge Bosons

Experiment	Γ_Z (GeV)	Γ_W (GeV)
UA2	$2.96 + 0.98 - 0.78(stat)$	$1.89 + 0.47 - 0.40(stat)$
CDF	$3.8 \pm 0.8(stat) \pm 1.0$	$2.17 \pm 0.20(stat) \pm 0.10(sys)$
LEP + SLC	2.546 ± 0.032	

Table 1.4 Experimental Measurements of $\sin^2\theta_W$

Experiment	$\sin^2\theta_W$
UA2	$0.2202 \pm 0.0095(stat + sys)$
CDF	$0.2317 \pm 0.0075(stat + sys)$
LEP	$0.2302 \pm 0.0021(stat + sys)$
World Average	$0.2309 \pm 0.0029(stat) \pm 0.0049(sys)$

The top quark and the tau neutrino are the two elements of the standard model that have not yet been directly identified. The electron-positron collider experiments at LEP and SLC (the Stanford Linear Collider) have set a lower limit on the top mass from the decay of Z^0 to top-antitop, of $m_t > 45.8$ GeV [1,13] The hadron colliders have the advantage of being able to look in different channels, but have also not yet identified the top quark. The cleanest channel to search for the top is in the decay of a produced top-antitop pair into W^+b and $W^-\bar{b}$ which decay to two charged leptons, two neutrinos and 2 jets (See Fig. 1.7). The three collider experiments have also searched for the decay of one of the tops entirely to jets and the other to leptons and a jet. The latter processes are also shown in Fig. 1.7. The results of the searches are listed in Table 1.5; the best limit being obtained by CDF, which has the highest center of mass energy. With the expected integrated luminosity of $25pb^{-1}$ for the 1992 D-Zero and CDF runs, a limit of $m_t > 140$ GeV should be achievable. A combination of all existing data pertaining to the standard model suggests $m_t \approx 137 \pm 40$ GeV[4].

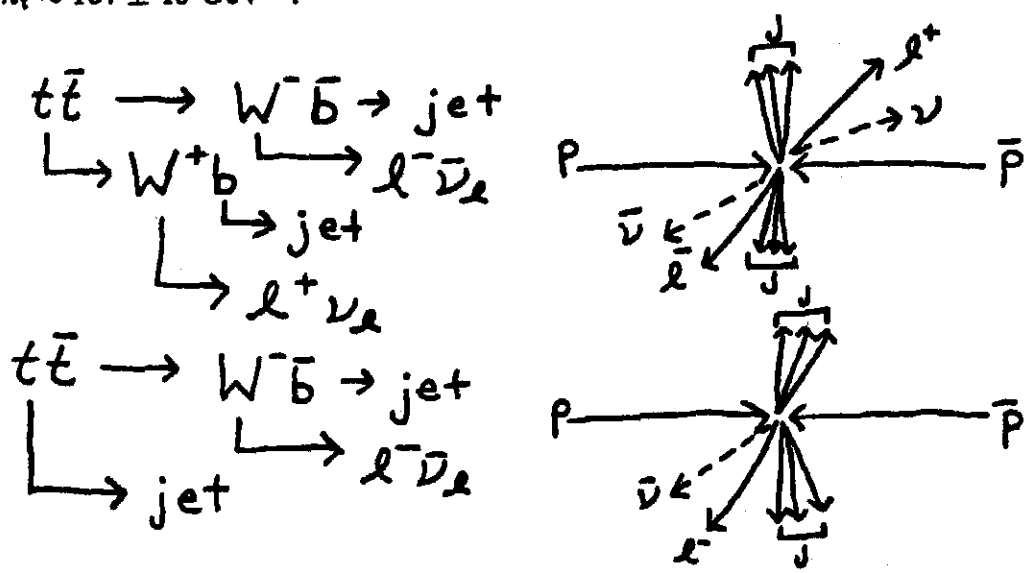

Figure 1.7 Diagrams for the decay of $t\bar{t}$

Table 1.5

Experimental Limits on Top Quark Mass

Experiment	Mass Limit
UA1	$m_t > 60GeV$ (95% CL)
UA2	$m_t > 67GeV$ (95% CL)
CDF	$m_t > 89GeV$ (95% CL)

The hadron collider experiments have also searched for possible deviations from the standard model that could signal the presence of new physics such as supersymmetry. No deviation from QCD has yet been seen in measurements of gauge boson production or jet production at high q^2, where any new substructure might affect the expected cross sections [4]. Because of its small expected yield, the Higgs H^0 of the standard model is not expected to be discovered at the Tevatron[14]. A minimal supersymmetric extension of the standard model predicts two charged Higgs particles, $H^{\pm}$. The LEP experiments have set a mass limit, at a 95 % confidence level, for $m_{H^{\pm}} > 42.0$ GeV; the hadron colliders have included the hypothesized decay $t \rightarrow H^+ b$ in their top searches. Additional gauge bosons are also expected from extensions of the standard model. CDF has set preliminary limits on the masses of any new Z and W bosons of $m_{Z'} > 380$ GeV and $m_{W'} > 480$ GeV at the 95% confidence level. Evidence has also been sought for compositeness of quarks, leptons and gauge bosons via the contact interactions that would result. These contact interactions, shown in Fig. 1.8, would increase the production cross

section for jets, the cross section dependence being $\approx (\frac{1}{p_T^2+\Lambda^2})^2$ where Λ is the compositeness scale. Limits on the quark-quark contact amplitude from the 2-jet spectrum at hadron colliders are as follows:

$$UA1: \quad \Lambda^{qq} > 410GeV \quad (95\%CL)^{[15]}$$

$$UA2: \quad \Lambda^{qq} > 370GeV \quad (95\%CL)^{[16]}$$

$$CDF: \quad \Lambda^{qq} > 950GeV \quad (95\%CL)^{[17]}$$

The most extensive searches at hadron colliders have been for supersymmetric particle production. These investigations have concentrated on the creation of gluino and squark pairs, the strongly interacting supersymmetric partners of gluons and quarks, respectively. CDF sets the highest mass limits, these being: $m_{squark} > 150$ GeV and $m_{gluino} > 150$ GeV (90% CL) [3]. With the additional data to be taken during the next collider run at Fermilab, all of these analyses will be greatly extended. The following chapter describes how the design of the D-Zero detector is matched to the above physics goals.

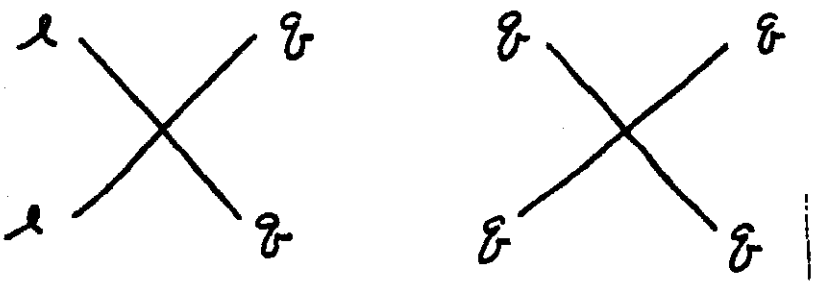

Figure 1.8 Diagrams of contact interactions that would increase the jet production cross section

CHAPTER 2

GOALS OF THE D-ZERO PHYSICS PROGRAM AND A GENERAL DESCRIPTION OF THE D-ZERO DETECTOR

The D-Zero experiment is the second large general purpose detector to study proton-antiproton collisions at the Fermilab Tevatron collider. CDF, the Collider Detector at Fermilab, the first such experiment, has been taking data at the Tevatron since 1987. One aspect influencing the design of D-Zero was to make the experiment complimentary to CDF, and thereby maximize the rewards of having two such detectors examining proton-antiproton collisions at the center of mass energy of 1.8 TeV of the Tevatron. The design features were also chosen to meet the needs of the physics goals of D-Zero, in particular, to detect leptons, hadronic jets of particles, and signatures involving missing transverse energy ($\not{E}_T$), all of which reflect important signals in collisions of constituents within the protons and antiprotons. In the following sections, the physics goals of D-Zero and the design features will be described, and it will be shown how the design of D-Zero meets the desired physics goals.

2.1 Physics Goals

There are three major physics signatures that the D-Zero detector was designed to study. These are charged leptons, such as muons and electrons, hadronic jets of particles and the missing transverse energy signal that char-

acterizes weakly-interacting particles like neutrinos. These signals are important because they indicate the occurrence of rare physics processes in proton-antiproton scattering, such as the decay of a top quark, that D-Zero hopes to examine. The details of the significance of each of these physics signatures are given below.

2.1.1 Detection of Charged Leptons

Because charged leptons appear in the cleanest decay modes of high mass states such as the gauge bosons, the top quark and the Higgs particle, the detection and measurement of the properties of high energy charged leptons is of primary importance to D-Zero. Lepton identification was taken into consideration in the design of almost every component of the detector. Precise measurement of both muons and electrons over the fullest possible solid angle is essential for separating interesting signals from the backgrounds due to QCD jets (expected to be the source of the largest background). Electrons and muons are measured differently which means that systematic uncertainties in their measurement differ, and consequently using both leptons provides a good check on the consistency of any new high mass phenomenon. As we will see, electron energies are measured in D-Zero using the electromagnetic calorimeters, and muons are detected outside of all the calorimeters. Thus electrons usually have to be relatively well isolated in order to be well measured, while muons can be observed even when produced within a hadronic jet. The top quark is likely to be discovered in either the electron or muon channel.

2.1.2 Detection of Hadronic Jets

As stated in Chapter 1, the dominant process in high energy proton antiproton collisions involves the production of hadronic jets. Precise measurements of jet-production properties, such as the cross section as a function of transverse momentum, and ratios of rates for different numbers of jets in an event, provide important checks of the theory of quantum chromodynamics (QCD). In particular, they provide insight into the nature of the running of the strong coupling constant α_s. Deviations from expectations of QCD could signify the onset of new physics processes beyond the standard model. Since such effects would depend on energy and momentum transfers, the precise measurement of jet energies is of particular importance. This requires a uniform calorimeter with good overall coverage. The device must also have good energy resolution and linearity of response as well as an equal response to photons and hadrons that make up the jets.

With very precise measurement of jets, one can also hope to compare jets that originate from quarks to those that arise from the fragmentation of gluons; it is expected that gluon jets will be spatially broader because they have a higher hadron multiplicity [2]. The fragmentation of constituents into jets of particles is at present poorly understood, consequently the energy of jets is often mismeasured. Studying two and three-jet events can lead to a better understanding of the backgrounds caused by such jet events for rare processes whose signatures include undetected energy from weakly-interacting neutral particles that escape detection.

2.1.3 Detection of Missing Transverse Energy

Neutral, weakly interacting particles such as neutrinos or the lowest mass neutral supersymmetric particle, (the photino) can be detected through the presence of an energy imbalance in an event, or as a "missing" energy. Longitudinal momentum in the collision is uncertain due to the a priori unknown relative motion of the constituents within the proton. Missing transverse momentum in any event can however, serve as an important signature for such physics processes. Transverse momentum (P_T) is defined as $P_T = |P| sin\theta$ where P is the total momentum and θ is the angle from the beam direction. Figure 2.1 shows the coordinate system of D-Zero: z is the direction of the proton beam; ϕ is the azimuthal angle in the x-y plane; and θ, is the polar angle measured relative to the z-axis. Transverse energy is also used instead of total energy because of the unmeasurable amount of energy carried by particles that are emitted at small angles (down the beam pipes). Excellent calorimeter energy resolution is required for precise measurements of E_T, as is an equal response to the electromagnetic and hadronic parts of hadronic showers. The latter will minimize the contribution of inherent fluctuations that occur in the evolution of particle showers to a missing-energy signal. The origins of such fluctuations will be discussed in Chapter 3. Most important, have as hermetic as possible calorimeter with as few cracks, holes or "hot spots" so that a minimum amount of energy is mismeasured or undetected. Fine transverse segmentation in tracking is desired so that errors in determining angles do not lead to large uncertainties in transverse momenta.

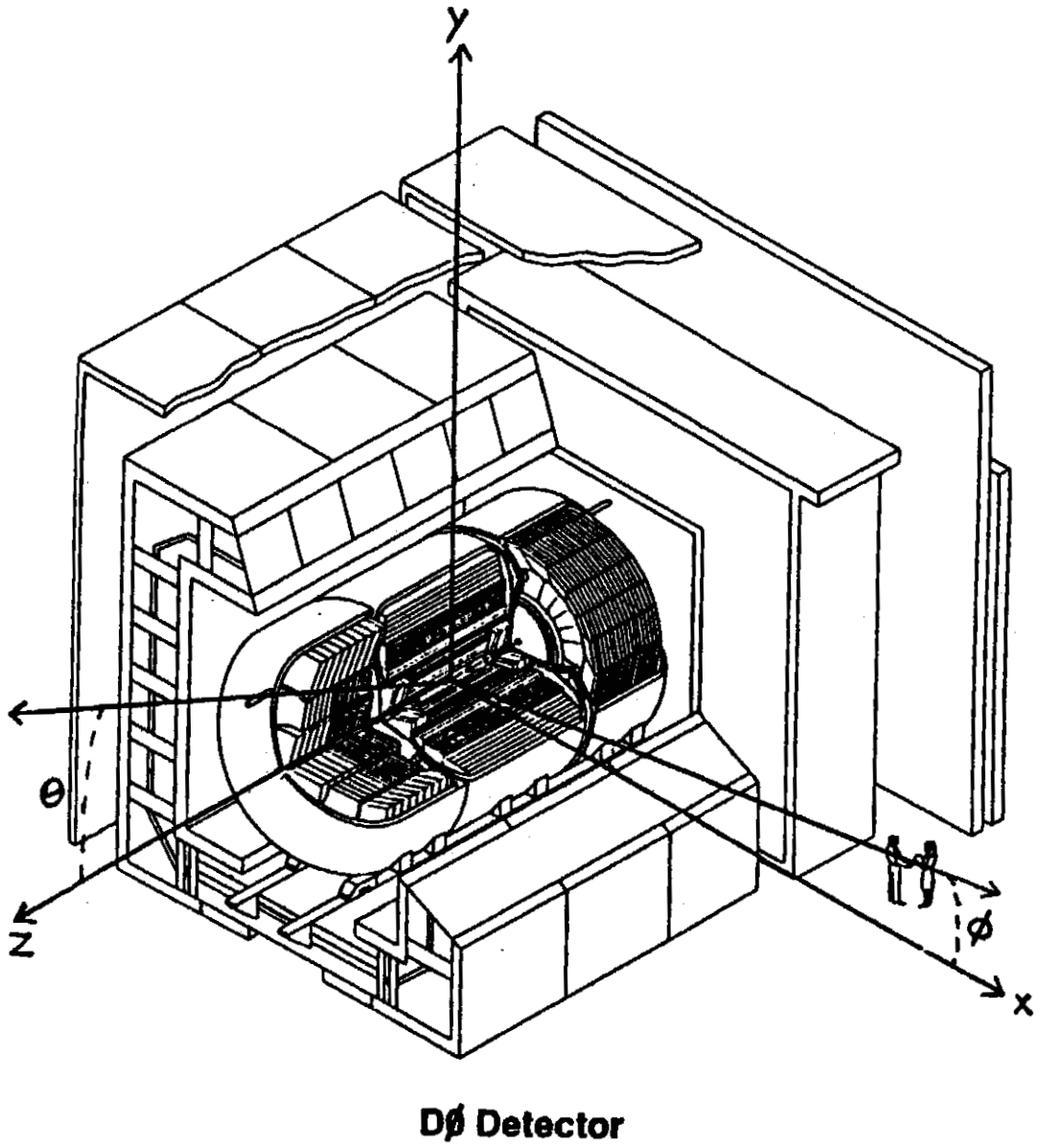

Figure 2.1 The coordinate system of D-Zero

2.2 The D-Zero Detector

As discussed in the previous sections, the D-Zero detector was designed to accomplish many different physics goals. In order to do so, it is composed of several different detector elements which combine to form a "hybrid" detection system. These detector elements include a central tracking system, a calorimeter and a muon tracking system. The central and forward tracking systems contain drift chambers that are designed to effectively track charged particles. The central tracking system also contains a vertex detector, and a transition radiation detector that can distinguish between electrons (e) and pions (π) and so compensates for the lack of a magnetic field. The calorimetry has been designed to precisely measure the energy of charged and neutral particles with energies greater than a few hundred MeV. It is "hermetic" to enable an almost 4π solid-angle measurement of the total energy of an event. The calorimetry is also many absorption lengths deep (typically > 7) to minimize the possible loss of hadrons that do not interact. Muons are measured outside of the calorimetry using magnetized iron toroids and specially configured proportional drift chambers.

A central magnetic field is often used in this type of detector to help determine the momentum of charged particles. D-Zero chose instead to do without a central magnetic field and use precise calorimetry for energy measurement. The tracking chambers require less volume without a magnetic field, so D-Zero has a smaller, and a more cost-effective calorimeter surrounding them. This approach is complimentary to CDF, which has a central magnetic field.

When these components are installed, they form one large, compact unit,

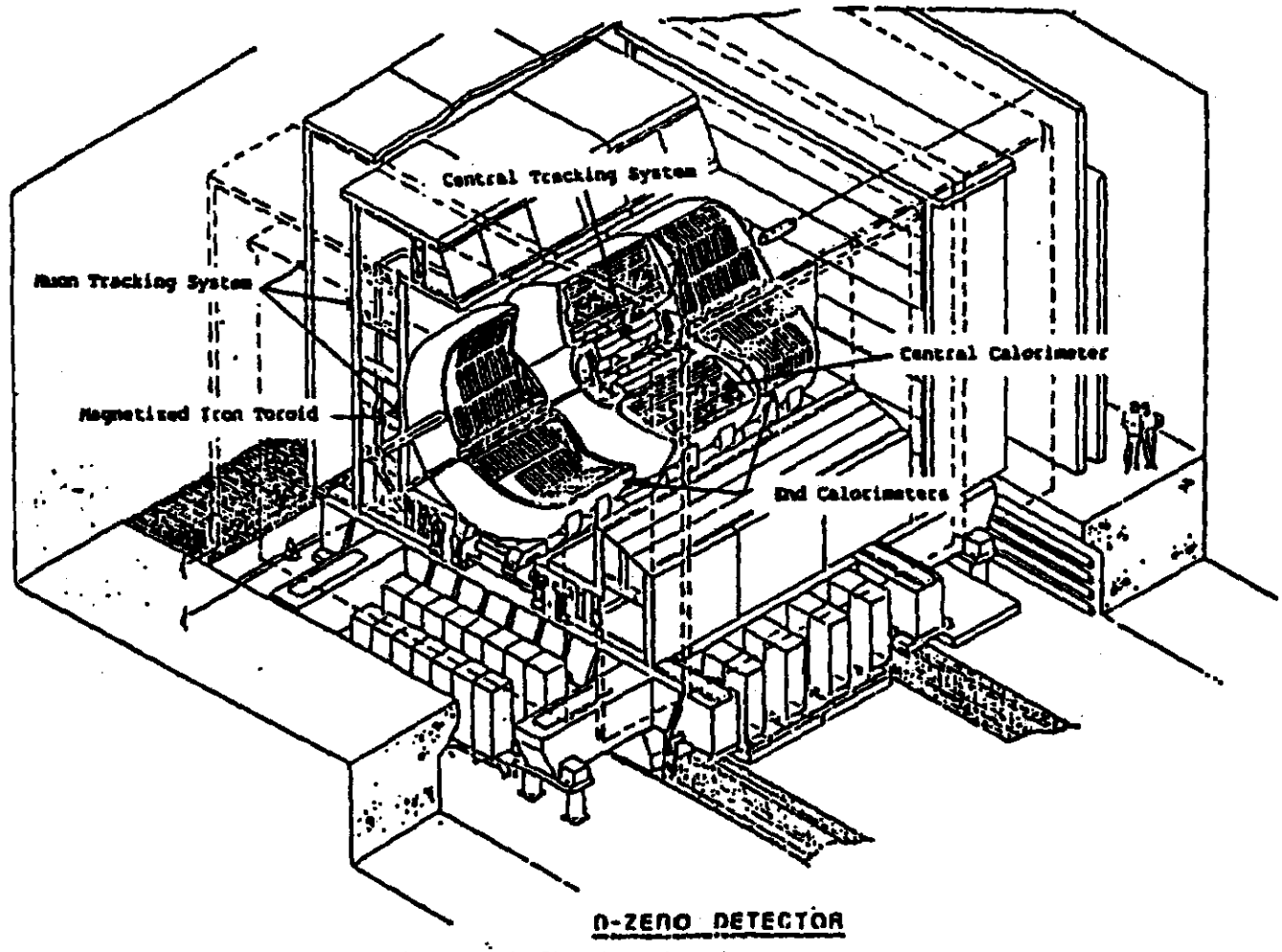

Figure 2.2 An overview of the D-Zero detector indicating the location of the different detection systems

approximately 16 × 12 × 12 meters in size and > 5000 tons in weight, which resides on a platform that can be rolled into the collision hall on tracks. A sketch of D-Zero is shown in Fig. 2.2. The first stage of the readout electronics and distribution boxes for the power lines for every segment of the detector are also located on the platform. A movable counting-house that contains the second stage of the readout electronics, the power supplies and the trigger logic, also rolls on tracks and follows the motion of the detector.

2.2.1 The Central Tracking System

The central tracking system, sketched in Fig. 2.3, consists of several parts: a set of vertex chambers, a transition radiation detector (TRD), an outer cylindrical drift chamber, and both forward and backward drift chambers. All the components, except the TRD, are drift chambers, where a charged particle creates ionization in a gas and this ionization charge drifts over a few centimeters in an electric field (≈1 kV/cm) towards an anode wire, where a high field around the anode wire causes an "avalanche" of ions and free electrons that are deposited on the anode. This avalanche causes a large pulse that is used to determine the position of the charged particle that caused the initial ionization.

The vertex detector is composed of three high precision drift chambers. Located just outside the beam tube, its purpose is to precisely measure track positions close to the interaction point in order to reconstruct event vertices. It was designed with close sense wire spacing (4.6 mm), short drift distances ($\approx 1.5cm$) and uses a gas with a low drift velocity (95% CO_2-5% ethane, for which v = 9.7 $\mu m/nsec$) to achieve excellent spatial precision and good two-

track resolution. The results from a test of the chamber using 10-150 GeV electron and pion beams indicated that the position resolution was 60 μm and the two track resolution was 630 μm at 90% efficiency [18] This precision should allow identification of multiple interactions and secondary decays by measuring positions of secondary vertices. This detector will also be used to veto photons that leave no track in the vertex chamber but convert to electron-positron pairs and give an electron-like signal in the transition radiation detector. A detailed description of the performance of this chamber can be found in [18].

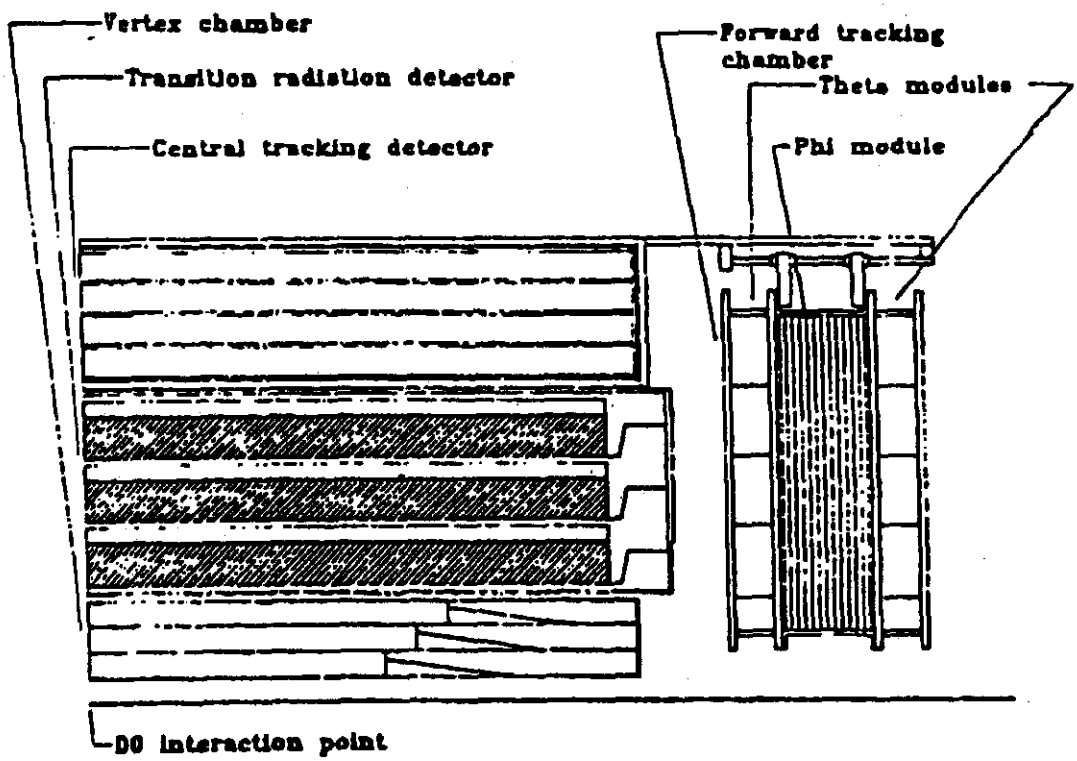

Figure 2.3 Cross-sectional view of the central detector, including the forward drift chambers is shown. This is one quarter of the whole detector.

The next layer of detection in the central tracking system is the transition radiation detector. The TRD consists of three concentric sets of thin (18

μm) polypropylene foils, followed by a radial drift x-ray detector. The total charge collected from the ionization of the detector gas (xenon), the time of arrival of the signal at the anode wire, and the time structure of the ionization clusters are used to discriminate between x-rays produced by electrons and by minimum ionization produced by hadrons. The e/π discrimination ratio is about 50:1 at 90% electron efficiency for energies below 200 GeV. Reference [19] gives a complete description of the TRD system of D-Zero.

The outermost layer of the central tracking system is the central drift chamber (CDC). It covers the rapidity range from η = -1 to 1, where $\eta = -\ln\tan(\theta/2)$*. It is made of four layers, each with 32 cells, with drift distances of less than 7 cm. Each cell contains 7 sense wires that measure the azimuthal angle. Resistive delay lines run along the length of each cell to determine the z position of a track. The CDC provides tracking information and precise measurement of the energy loss of a particle as it traverses the gas in the chamber (dE/dx). The resolutions obtained during the 1990 beam test of three CDC modules containing 8 full cells were: azimuthal position resolution of 200 μm, z position resolution of 2.5 mm, and two track resolution of 2 mm at 90% efficiency. Precise measurement of dE/dx is useful for separating unopened e^+e^- pairs (due to photon conversions or π^0 Dalitz decays) from single electrons. Based on dE/dx, the anticipated discrimination of two overlapping tracks from single tracks is 50:1. A detailed account of the CDC is available in Reference [20].

---

* The Lorentz invariant rapidity is defined as $y \equiv \frac{1}{2}\ln\frac{(E+P_z)}{(E-P_z)}$. The pseudorapidity η is the rapidity of a particle with zero mass. It is a more easily determined parameter used in D-Zero data analysis.

The forward and backward drift chambers (FDC's) provide tracking information similar to the CDC, but in forward and back directions, and also determine the dE/dx of the charged particles that pass through it. The FDC's cover the rapidity range $1 < |\eta| < 4$. They each contain 18 layers of cells along z using two different wire orientations. There is a radial section that measures drifts in the transverse direction and consists of 16 layers of 36-wire planes strung in the radial direction. This section is sandwiched between two 8-wire sections that approximately measure the θ coordinate. (See Fig. 2.3) These θ layers are instrumented with delay lines to provide both the orthogonal coordinates of a hit and the position along the wires. One of the two FDC chambers was tested in the 1990 test beam run. It exhibited the following characteristics: spatial resolution of 200 μm, two hit resolution of 3.2 mm at 90% efficiency, and two track resolution of 4.8 mm at 90% efficiency. A recent dissertation on these test beam results is available in Reference [21].

2.2.2 The Muon Tracking System

The muon tracking system is composed of proportional drift chamber tubes (PDTs) placed on either side of magnetized toroids. Figure 2.4 shows these chambers and the toroids spread apart. Muon momentum is determined by measuring the deflection of the trajectories in the r-θ plane caused by the 2 Tesla azimuthal magnetic field in the toroids. There are four layers of PDTs in front of the toroids to measure incident muons, and two sets of three layers, each separated by 1-2 meters, to find the exiting muons' directions. The central muon system spans an angular range of $\theta = 45°$ to $135°$ and the end systems (EF and EMC) cover from $\theta = 45°$ down to $11°$ from the beam

axis. Smaller angle coverage is provided by additional muon detectors located around the beamline down to $\theta = 3°$. This configuration of chambers covers a large fraction of the solid angle and so provides excellent coverage of any produced muons.

The combined depth of the toroids and calorimeters varies from 13 absorption lengths at $\theta = 90°$ to 18 absorption lengths at small angles. (The absorption length is the characteristic length for hadronic interactions.) This feature helps in identifying muons within the cores of hadron jets, since usually only muons will exit the calorimeter. The muon system can discriminate between muons and secondary hadrons that "punch through" the calorimeter by examining the vertex location of the track and the intersection point of the tracks that enter and exit the toroids. Tests made using the D-Zero muon geometry found a rejection factor against a hadron simulating a muon that exceeds 10^4 for momenta of $p \geq 10$ GeV/c.

The proportional drift tubes that form the layers have a rectangular cross section ($\approx 4 \times 10cm^2$) and vary in length from 2.4 to 6 m. Tubes at different radii in a layer are staggered to help untangle left-right drift ambiguities in the cell. A sophisticated readout system is utilized to ascertain exactly where along its length the hits on each wire occur. This system uses cathode pad strips above and below the anode wire that are cut in a repetitive diamond pattern. The ratio of charge on the inner and outer pads of this array, and the time difference in the arrival of the signals at either end of the chamber, provide a measurement of the transverse and longitudinal coordinates of the hit. Performance data for the muon system from tests are: transverse position

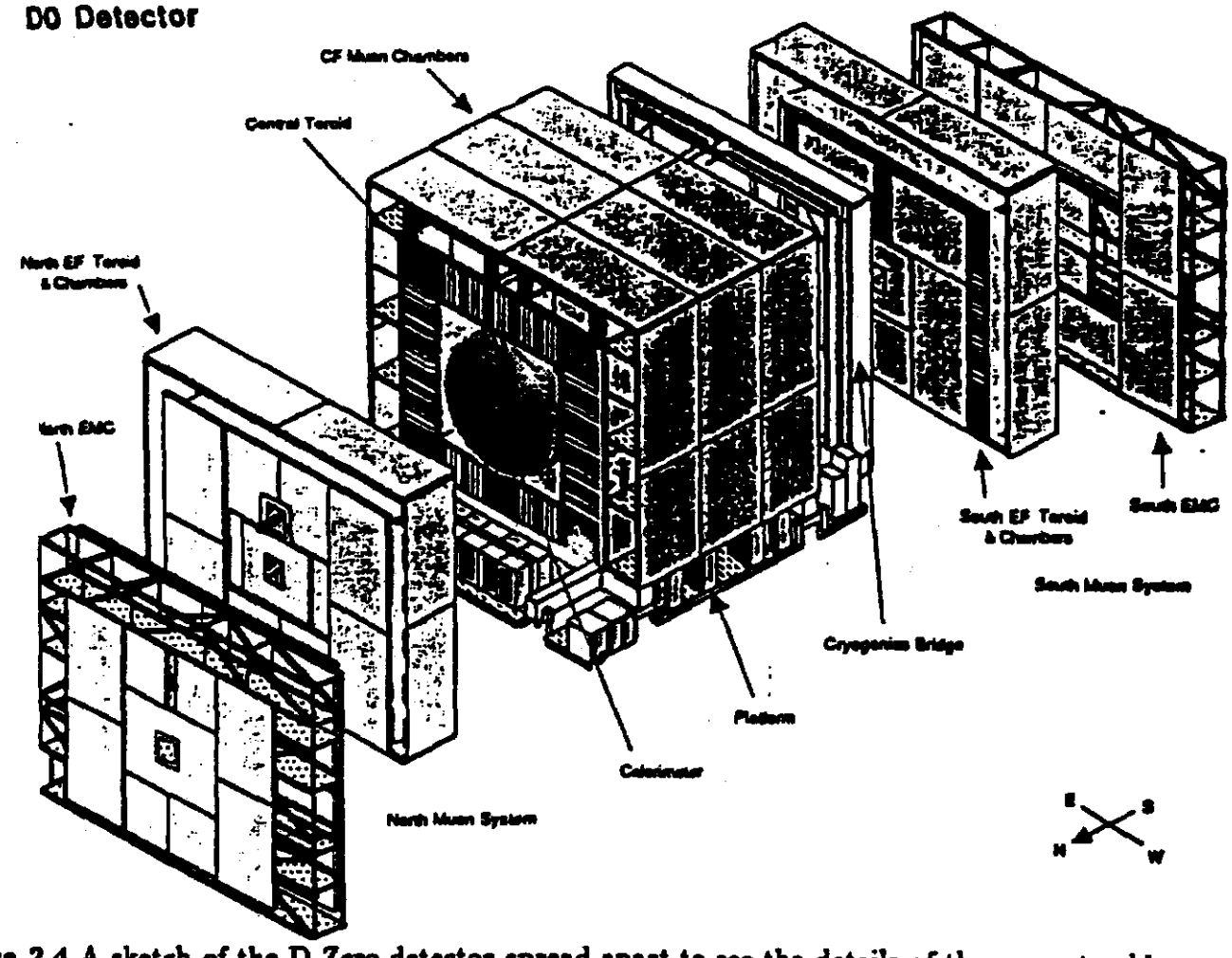

Figure 2.4 A sketch of the D-Zero detector spread apart to see the details of the muon tracking system

resolution of 200 μm, longitudinal position resolution of 3 mm, and momentum resolution using all three layers of $\Delta p/p \approx 18$ % for $p \leq 300$ GeV/c [20].

2.2.3 The Calorimeters

The performance of the D-Zero calorimetry is the central topic of this dissertation. D-Zero's calorimetry consists of a central calorimeter (CC) and two end calorimeters (EC); each consists of an assembly of modules that resides in its own separate cryostat, as shown in Fig. 2.5. The central calorimeter covers an angular range between $\theta = 35°$ and $145°$, or $|\eta| \leq 1.2$; the end calorimeters (ECN and ECS, north and south) extend the coverage down to $\theta \approx 1°$ or $0.9 \leq |\eta| \leq 5$ to form a highly hermetic system.

The electromagnetic modules (32 CCEM and one ECEM in ECN and in ECS) reside closest to the interaction region and detect the energy from electromagnetically interacting particles such as electrons, photons and π^0s. These modules are divided longitudinally into four layers for a total of ≈ 21 radiation lengths in depth. The transverse segmentation of the EM modules is $\Delta\eta \times \Delta\phi = 0.1 \times 0.1$. In the third layer, where EM showers have maximum energy deposition, the segmentation is decreased to $\Delta\eta \times \Delta\phi = 0.05 \times 0.05$. The next layer of the calorimetry is made up of fine hadronic modules (16 CCFH and the first four layers of ECIH, inner hadronic and 16 ECMH, middle hadronic, for each of the ECs, as shown in Fig. 2.5); these range from 3.2 to 4.9 absorption lengths in depth. This segment of the calorimeter detects leakage from the EM sections and detects and measures the energies of hadronic particle showers. The four fine-hadronic longitudinal layers have lateral segmentation of $\Delta\eta \times \Delta\phi = 0.1 \times 0.1$. The outermost section, away

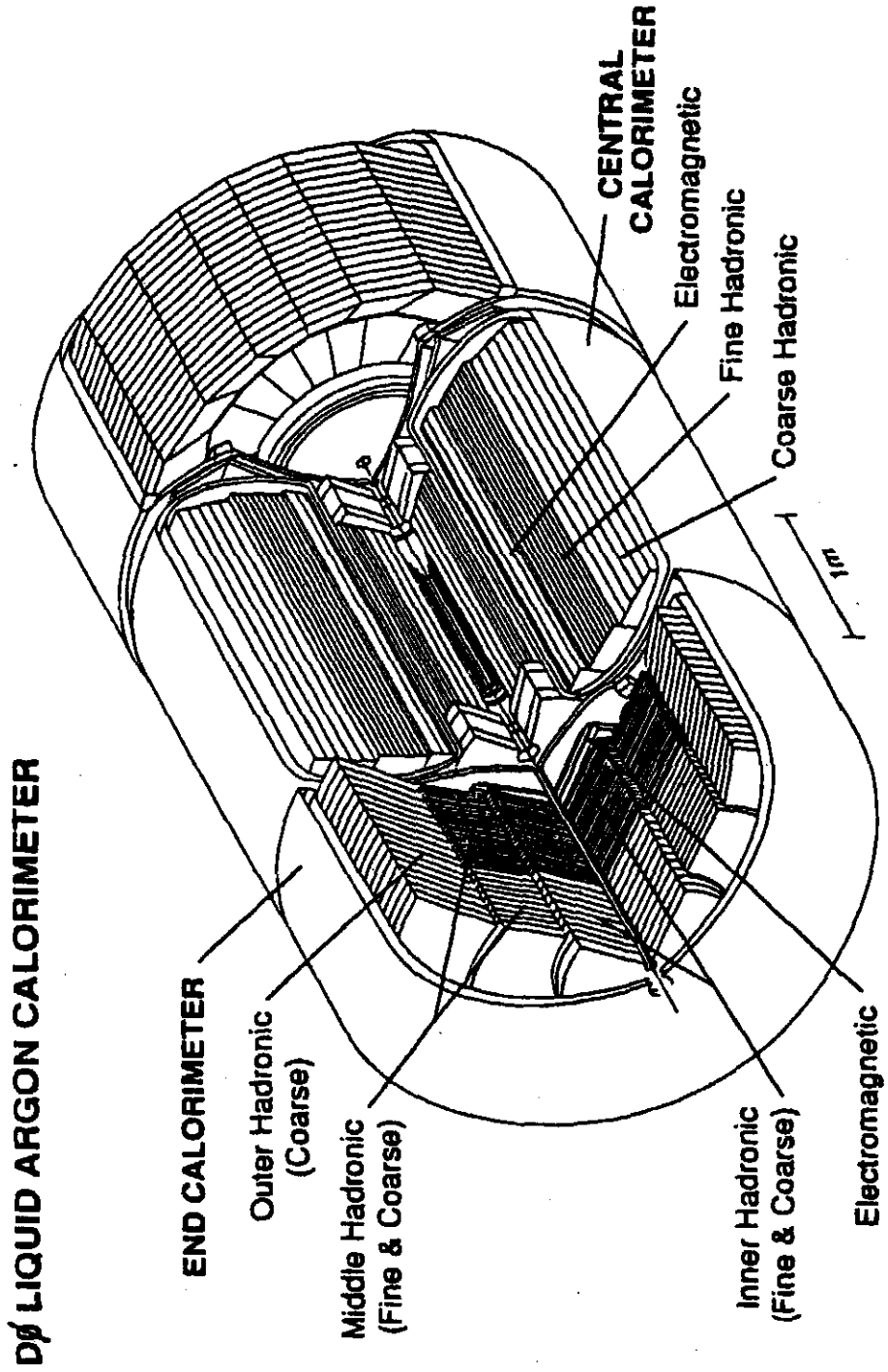

Figure 2.5 The modules that comprise the D-Zero central and end calorimeters

from the collision point, contains the coarse hadronic modules (16 CCCH and 16 ECOH per EC, outer hadronic and the fifth layer of the ECIH and ECMH modules). These modules have the same lateral segmentation as the FH modules but only have one longitudinal layer ≈ 4 absorption lengths in depth. The purpose of these modules is to detect energy leakage outside of the FH modules.

The D-Zero calorimeter is what is known as a sampling calorimeter. In this type of calorimeter the energy deposited by the particles traversing the calorimeter is detected only in sensitive layers that are interspersed with layers that have passive absorber. Only a small fraction of the energy is deposited in the sensitive regions in the form of ionization of the medium, and this is read out and serves to sample the entire energy deposition. More aspects of calorimetry are given in Chapter 3. The parameters that govern the design are the required electromagnetic-shower resolution, hadronic-shower resolution, and the ratio of the response to electrons as opposed to hadrons (known as e/h). The detecting medium chosen for D-Zero, uranium-liquid argon (U-LAr), was dictated by the need for a highly segmented, dense calorimeter with good energy resolution. Another important attribute of LAr calorimetry is that, as long as the liquid is kept reasonably pure (< 2 ppm O_2), the signal will not degrade over the course of the run. This is because LAr is not susceptible to radiation damage. Also, if the response is uniform from module to module, this means that not all modules have to be calibrated. How well U-LAr satisfies D-Zero's resolution and response requirements will be discussed in the next chapter.

Each module is enclosed in a thin steel case, and is made up of a stack of absorber plates (uranium for EM, FH, and IH, copper for CH, steel for OH), separated from NEMA G-10 signal boards by 2.3 mm LAr gaps. Figure 2.6 shows the layout of the basic sampling cell. The details of the construction of several of the end calorimeter modules are given in Chapter 4. The readout cells in these modules are aligned either parallel to the collision axis, as in the central calorimeter, or perpendicular to the axis as in most of the end calorimeters (EM,IH,MH), or at 45° for ECOH modules. This is illustrated in Fig 2.7.

This dissertation concerns the study of the response of three end calorimeter modules to electron and pion beams for different angles of entry into the stack. The data were accumulated during 1990 fixed target run at Fermilab. As stated in Chapter 1, Chapter 4 gives a detailed description of the test beam apparatus and Chapter 5 gives the results of the measurements of the performance of these calorimeter modules.

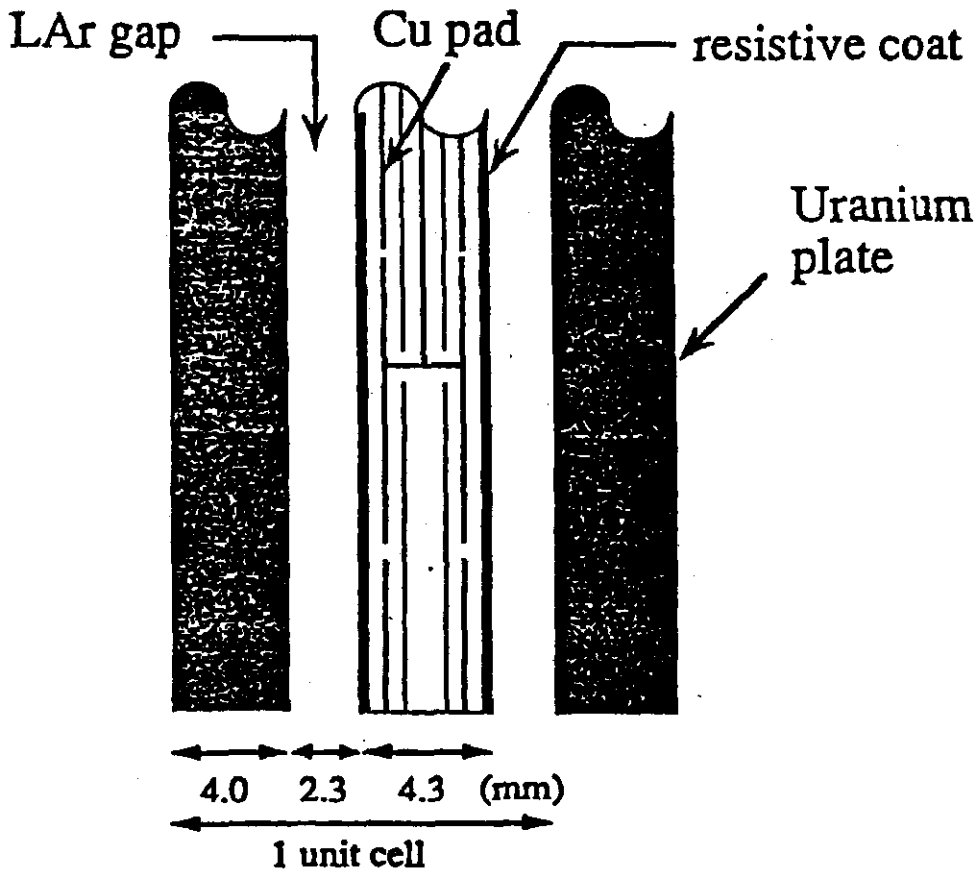

Figure 2.6 The composition of the basic sampling cell of a calorimeter module

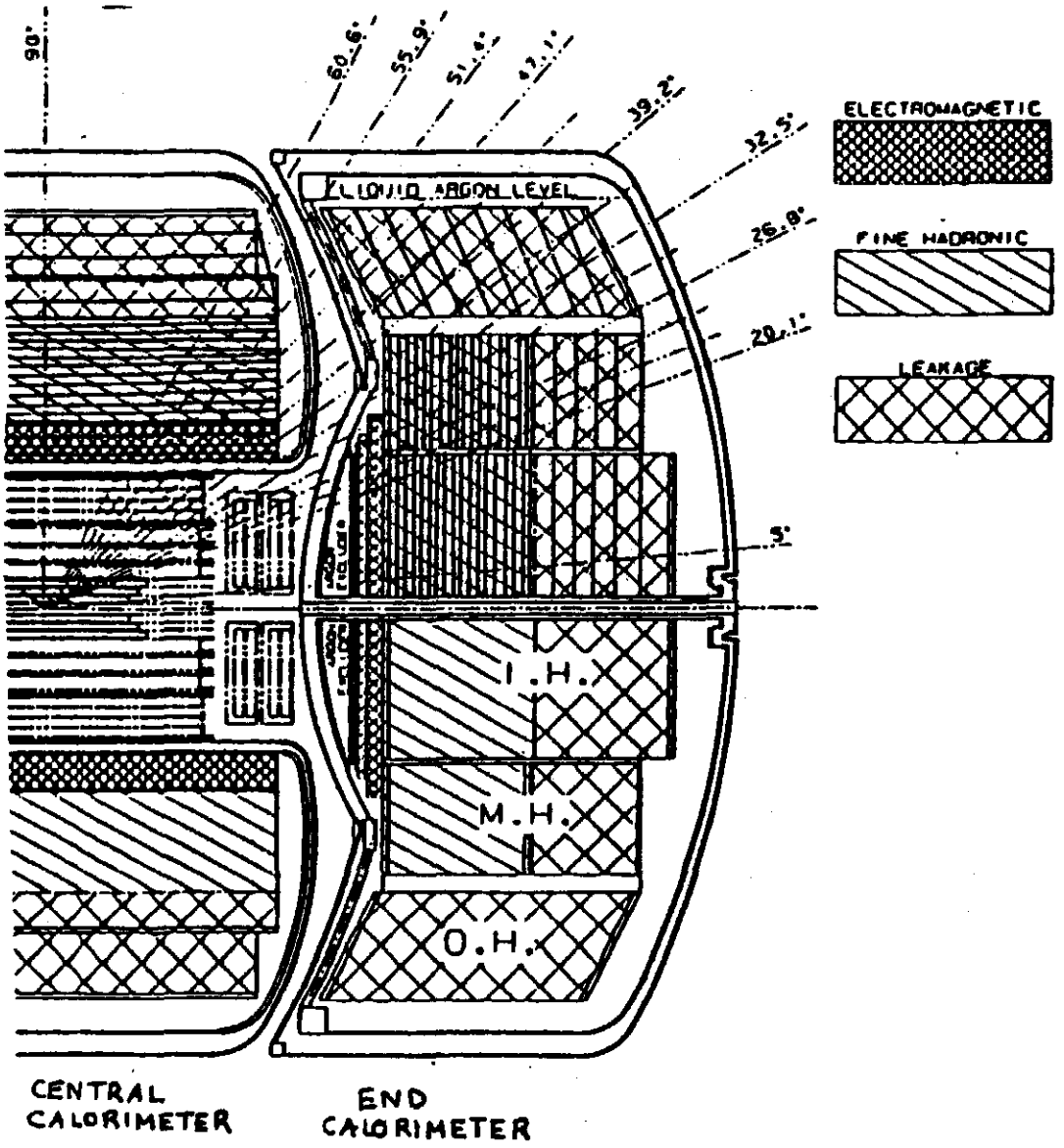

Figure 2.7 A cross-sectional view of the central and end calorimeters

CHAPTER 3

CALORIMETRY AND PARTICLE SHOWERS

Particle physicists use devices known as calorimeters to measure energies of elementary particles. Calorimeters are blocks of matter in which a particle interacts and deposits all of its energy, some in the form of a measurable quantity. This signal is generally in one of the following forms: electrical, optical, thermal or acoustical. The importance of calorimeters and aspects of their design characteristics will be discussed in section 3.1.

When particles interact in matter their energy becomes degraded and develops into a cascade or shower of low energy particles. Different types of elementary particles have different characteristic shower patterns because of the different processes that are involved in their interactions. The processes can involve electromagnetic, strong and occasionally, weak forces between the particle and the detector media. In section 3.2, we will describe the energy loss mechanisms for electromagneticly interacting particles and their resulting signatures, as well as the resolution characteristics that result from these types of interactions. Section 3.3, will deal with hadronic showers. Finally, we will discuss the impact of the different particle interactions on the design choice of the D-Zero calorimeter.

3.1 Calorimeter Design

3.1.1 Purpose of Calorimetry

Calorimeters comprise a major component of any modern high energy physics experiment. There are several reasons for this. One is that calorimeters are sensitive to both charged and neutral particles. Their measurement accuracy improves with increasing energy because calorimetry is based on statistical sampling properties. Because the dimensions needed to contain the energy deposited by a particle, increase only logarithmically with energy, compact instruments can be used at high energies. It is also possible to distinguish different types of particles because their interaction characteristics ("showers") can be quite different. Also important is that calorimeters do not require a magnetic field to measure energy. They can be highly segmented so that good position information can also be made available, and interesting events can be triggered with a high degree of selectivity. As detailed in the previous chapter, good calorimetry is important for the physics that D-Zero hopes to study.

3.1.2 Sampling vs Homogeneous Calorimeters

Calorimeters can be of two types: homogeneous devices, whose entire volume is sensitive, and sampling devices, where only a fraction of the volume is sensitive. Homogeneous calorimeters tend to be expensive and so are only used to detect electromagnetically interacting particles whereas sampling calorimeters are more economical for all particle types. Examples of homogeneous devices are lead glass shower counters that are based on the detection

of Cherenkov light and large crystal arrays based on the detection of scintillation light. The D-Zero calorimeter, as described in the previous chapter, is an example of a sampling calorimeter. It is made of a dense, passive absorber, depleted U^{238}, and an active material, liquid argon (LAr). The uranium and liquid argon take the form of a sandwiched layer structure of passive and active media, which is the most common design employed. Typically 5 - 10 % of an incident particle's energy is deposited in the active layers through ionization of the liquid.

Although sampling fluctuations in the amount of energy deposited in the active material often limit the energy resolution of the detector (especially the electromagnetic part), sampling calorimeters have other very useful attributes. These include the ability to make very compact devices if one uses dense absorber mediums. Unlike homogeneous devices, sampling calorimeters can be designed to have equal energy response to both electrons and hadrons. This is often refered to as compensation, and it will be shown in Section 3.3 why this is important. We also wish to point out that sampling fluctuations become less important at higher energies because the energy resolution tends to become dominated by systematic effects.

3.2 Electromagnetic Calorimetry

3.2.1 Electromagnetic Interactions

The electromagnetic interaction manifests itself in many ways. The primary energy loss process for high energy electrons and positrons is bremsstrahlung. This is the process by which electrons (and positrons) radiate pho-

tons as a result of their interaction with the nuclear Coulomb fields. These photons can convert to e^+e^- pairs, which can radiate again, etc. This results in the particle multiplication that is typical of a high energy electromagnetic (e.m.) cascade. At lower particle energies, ionization takes over as the primary energy loss process for electrons and positrons.

Photons interact with matter through three different processes. At energies less than $\approx$ 10 MeV the most prevalent are the photoelectric effect and Compton scattering. In these interactions, all or some of the photon's energy is transferred to an atomic electron. Once the photon energy is higher than twice the electron rest mass, pair production can occur. This is the process wherein a photon converts into an electron-positron pair (e^+e^-), contributing to particle multiplication in a developing shower.

The electromagnetic shower process is completely understood on the basis of quantum electrodynamics (QED) [23]. It depends upon the electron density in the absorber medium which is roughly proportional to the atomic number, Z, of the medium. Figure 3.1 shows the results of calculations of the cross sections for the various energy loss processes described above as a function of energy for electrons and photons in three different media [24,25]. These materials differ greatly in Z-value (carbon: Z=6, iron: Z=26, uranium Z=92) so the Z-dependence of the energy range of these processes can be easily seen. Above 100 MeV, radiation loss dominates for electrons and pair production dominates for photons in all three media. Above 1 GeV, these two processes become weakly energy dependent [26]. Below 100 MeV, the individual cross sections are quite Z dependent. The energies at which Compton scattering

begins to dominate over the photoelectric effect, and pair production dominates over Compton for photons, are quite different. Also, the point at which radiation loss surpasses ionization loss as the primary process for energy loss by electrons depends very strongly on Z.

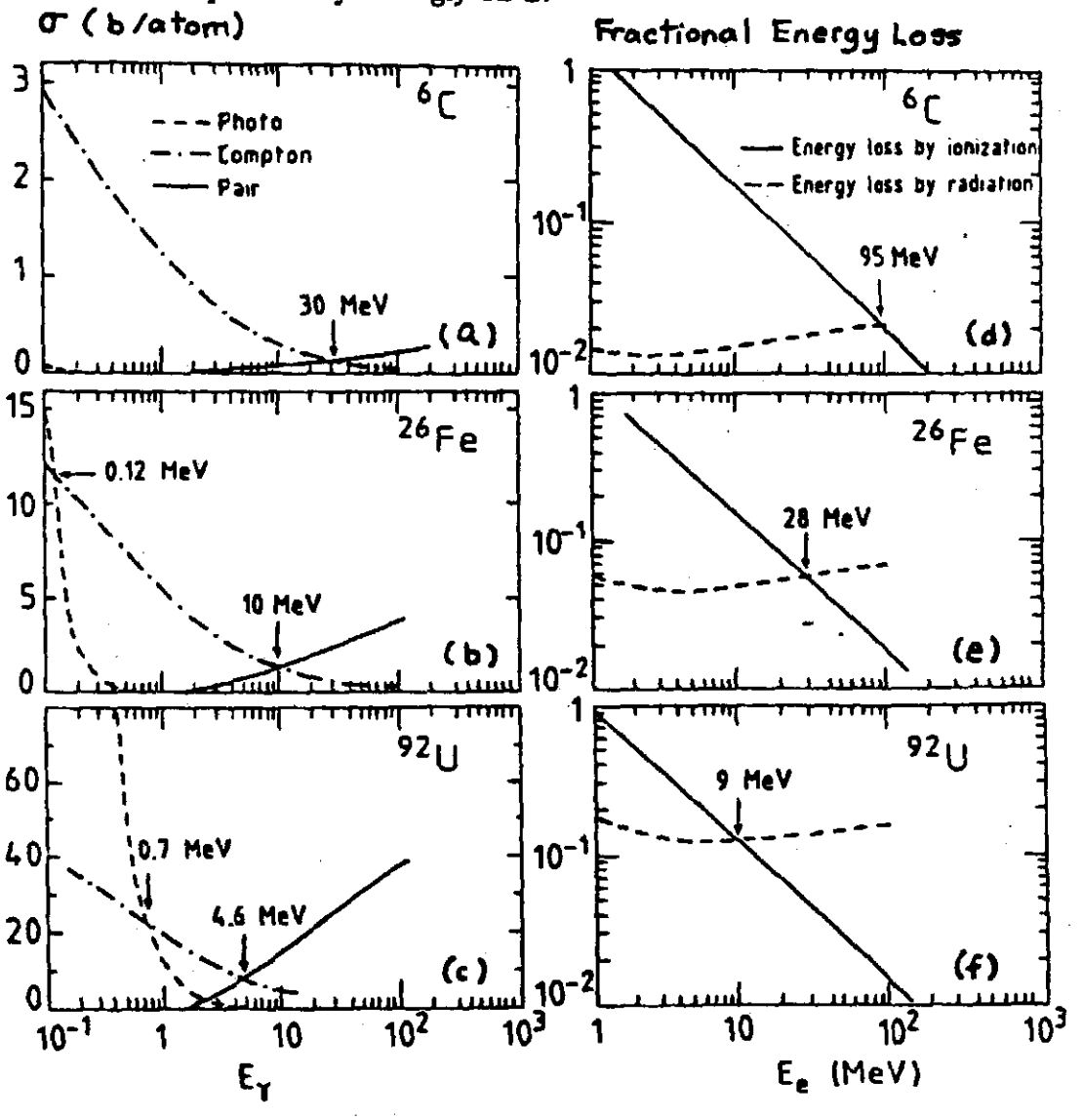

Figure 3.1 The cross sections for pair production, Compton scattering and photo-electric effect, as a function of photon energy (a-c) and the fractional energy loss by radiation and ionization as a function of electron energy (d-f) [24,25]

The energy at which an electron loses as much energy in collisions (with atomic electrons) as in radiation (induced by the nuclear Coulomb field) is called the critical energy, ϵ_c. This is the value of energy below which very little particle multiplication occurs, and the remaining energy of an electron is absorbed through molecular excitation and ionization of the medium.

3.2.2 Characteristics of Electromagnetic Showers

Because electromagnetic shower development is governed by the electron density of the absorber, one can describe the characteristics of these showers in a material-independent way. Longitudinal dimensions can be described using the radiation length, X_0. This is the distance over which the energy of an electron drops to 63.2% of its initial value. This energy is lost primarily through the radiation of photons (Bremsstrahlung). The radiation length of a material can be approximated by the following relation:

$$X_0 \approx 180\ A/Z^2\ g\ cm^{-2} \text{ (to better than 20\% for } \approx Z > 13) \qquad (3.1)$$

where A is the atomic weight. Figure 3.2 shows the longitudinal shower development for 6 GeV/c electrons in four different materials. The scaling of the energy deposition with radiation length can clearly be seen in the figure. This shape can be understood, in that the steep rise corresponds to the increase in the number of particles in the early part of the shower (up to when all secondaries reach the critical energy), after which essentially no multiplication occurs, followed by a slow decrease in energy deposition as more and more particles are completely absorbed in the medium. The appearance of the shower maximum at slightly increasing depth for high Z absorbers occurs because particle multiplication continues to lower energies due to the smaller

value of ϵ_c. This shape can be described by the form [27]

$$\frac{dE}{dz} = \frac{E_0}{\Gamma(\alpha+1)} b^{\alpha+1} z^{\alpha} e^{-bz}, \quad z = x/X_0, \quad \alpha = bz_{max}, \tag{3.2}$$

where E_0 is the incident particle energy, Γ is the gamma function, z is depth in radiation lengths, x is the depth in cm, z_{max} is the depth of the shower maximum in radiation lengths, and α and b are the parameters to be fitted.

Figure 3.2 shows that it takes $\approx 22X_0$ to contain at least 99% of a shower of this energy. This is equivalent to 7.0 cm of uranium. Because the position of the shower maximum is proportional to Log E_0 plus a constant, only a small increase in material thickness is needed to contain higher energy showers. The length required to contain 98% of an electromagnetic particle's energy can be parametrized as

$$L(98\%)_{av} \approx t_{max} + 4\lambda_{att} \tag{3.3}$$

where λ_{att} describes the slow exponential fall off of the energy in the shower [26]. Experimental values for λ_{att} are all about $3.4 \pm 0.5X_0$. It is important to contain all the energy in the shower because fluctuations about the average longitudinal energy loss can limit resolution.

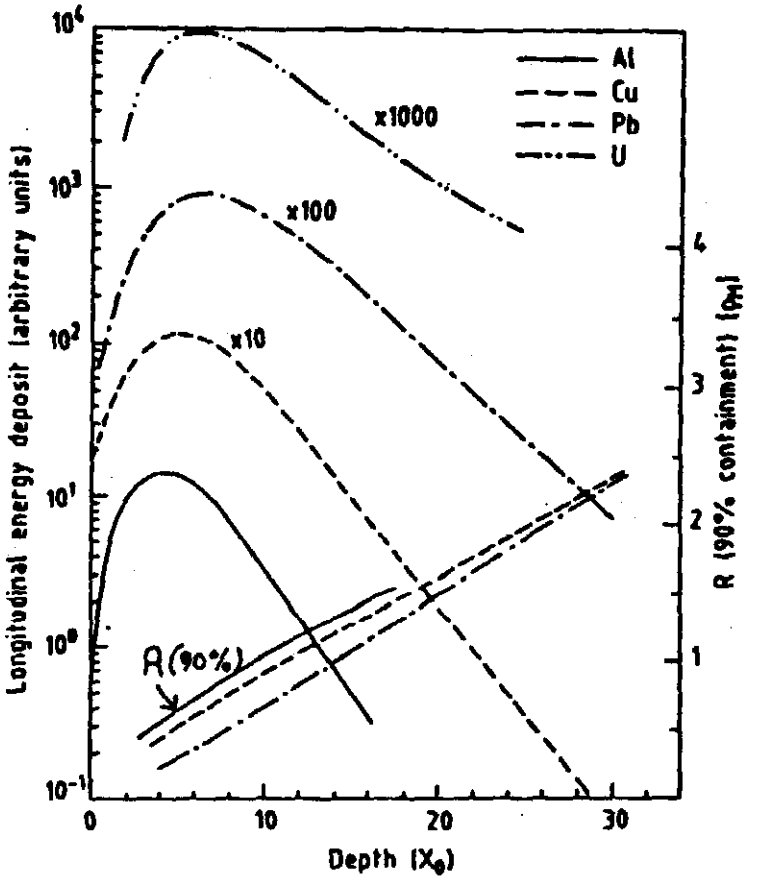

Figure 3.2 The longitudinal shower development (left scale) of 6 GeV/c electrons shows scaling in units of radiation length. On the right, the shower radius for 90% energy containment is plotted as a function of depth [26].

The transverse unit used to characterize an electromagnetic cascade is the lateral spread of an electron induced shower at the critical energy after it traverses one radiation length of material. This is called the Moliere radius :

$$R_M = \frac{E_S}{\epsilon_c} X_0 \quad E_S = 21 MeV \tag{3.4}$$

where ϵ_c is the critical energy, and $E_S = \sqrt{4\pi \times 137} mc^2$ is the multiple scat-

tering theory constant. R_M just like X_0 is dependent only on the A and Z of the material and can be approximated as $R_M \approx 7$ A/Z g cm^{-2}. Multiple scattering of electrons is the dominant cause of lateral spreading in the early part of an e.m. shower . The decreasing energy of the shower particles causes a gradual widening of the shower with depth. Beyond the shower maximum of an e.m. cascade, particularly in high Z media [22], bremsstrahlung photons that can travel quite far from the shower axis define the shower spread. The spatial distribution of this component has no simple dependence on A and Z [28]. These two processes combine to create a lateral shower profile that has a central core that scales as R_M surrounded by a wide lower energy "halo". Figure 3.3 shows the radial shower profile at varying depths for 1 GeV electrons in lead (simulated by an EGS4 Monte Carlo calculation). The shape is as expected. We see that 90% of the shower energy is contained within a radius of 2 R_M. Figure 3.2 displays the radius for 90% containment plotted as a function of depth for 3 different materials. The radial dimensions scale with R_M in the later stages of the cascade. The Moliere radius for uranium is ≈ 1 cm.

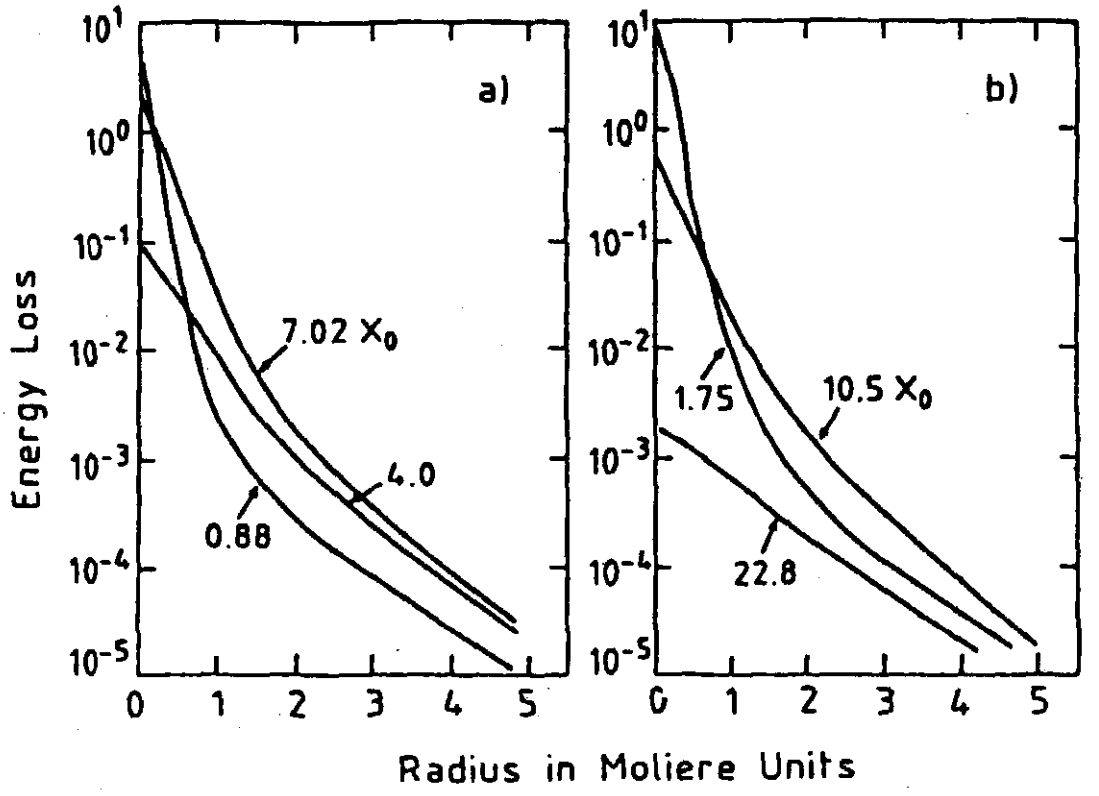

Figure 3.3 The lateral distribution of the energy deposited by a 1 GeV e.m. shower in lead at various depths is shown. These are results of an EGS4 Monte Carlo calculation [22].

3.2.3 Electromagnetic Energy Resolution

Particle showers involve statistical processes and are detected in calorimeters through the the production of electron-hole pairs, ionization, light etc., depending on the medium. The resolution for determining a particle's energy is limited by fluctuations in these elementary processes as well as in their sam-

pling. The width (σ) of any signal (S) for detecting mono-energetic particles can often be related to the number (n) of ionization electrons produced, as $\sigma(S)/S \approx \sqrt{n}/n$; for a calorimeter that has a linear response with energy, this leads to $\sigma(E)/\mathrm{E} \approx \mathrm{C}/\sqrt{E}$. The energy resolution improves with increasing E, which is one reason why calorimeters are so useful.

Fluctuations in the number of primary processes that contribute to the calorimeter signal limit the achievable energy resolution. For fully contained showers in a fully active calorimeter, this intrinsic energy resolution can be shown to be *[27].

$$\frac{\sigma(E)}{E} \approx \frac{0.7\%}{E(GeV)} \tag{3.5}$$

In most calorimeters, including that of D-Zero, the resolution is dominated by other factors such as sampling fluctuations, instrumental noise, nonuniformities or incomplete shower containment. These factors cause departures from Eq. 3.5. Electronics noise and in D-Zero's case, noise from the U^{238}, contribute an energy independent ($\Delta E \approx$ constant) term to the resolution $\sigma(E)$. A term proportional to $\Delta(E)/E$ results from energy dependent noise sources such as fluctuations in the electronics gains.

For sampling calorimeters, the energy resolution is dominated by the fact that only a fraction of the incident particle energy is measured. Fluctuations in this fraction are statistical, and consequently are expected to contribute to the total energy resolution in proportion to $\sqrt{E}$. In calorimeters using relatively dense active material, such as LAr, the contribution to the resolution from sampling fluctuations for substantial variations in design scales as $\sigma(E)/\mathrm{E}$

* Energy in all these resolution formulas is measured in GeV.

$=\sqrt{t_{abs}/E}$, where t_{abs} is the thickness of absorber, for any specified thickness active material. Sampling fluctuations also depend upon the thickness of the active (read out) planes, t_{act}, in a similar manner, namely $\sim \sqrt{t_{act}/E}$. The signal and the fluctuations depend, of course, on both thicknesses and on the Z values of the active and passive layers [22]. The resolution and signal response can therefore be tuned by the choice of calorimeter design.

The best energy resolutions are obtained using homogeneous, fully sensitive devices that do not involve sampling fluctuations. Scintillating crystals, such as NaI, remain unsurpassed in energy resolution at low energies, yielding $\sigma(E)/E \approx 0.02\ E^{-1/4}$ [22]. Lead glass shower Cherenkov counters have been found to have resolutions in the range of $5\%/\sqrt{E}$ to $12\%\sqrt{E}$ [22]. For sampling calorimeters, with dense active material (LAr or plastic scintillator), the resolutions range from $7\%/\sqrt{E}$ to $20\%\sqrt{E}$ [22]. The constant term in the resolution from gains fluctuations is $\approx 1\%$ for systems using photomultiplier tubes, such as plastic scintillator calorimeters. For LAr readout, it is $\leq 0.5\%$.

3.2.4 Electromagnetic Position Resolution

The position of the impact point of a particle that creates an electromagnetic shower in a calorimeter can be determined from measurements of the transverse and longitudinal shower shape. The position resolution is limited by the transverse and longitudinal granularity and the signal/noise ratio of the calorimeter. Because the position is often determined using a weighting technique involving the transverse distribution of energy, fluctuations in the energy measurement, detailed above, contribute to the position resolution. For a sufficiently fine-grained detector, the position resolution $\sigma(x)$ would

scale with energy as $\sigma(x) \approx \sigma_0/\sqrt{E}$ due to the inherent statistical nature of shower development. Other noise sources can cause deviations from this $E^{-1/2}$ scaling.

Before the maximum development of an electromagnetic shower, more than 90% of the energy is contained in a cylinder of radius $r = 0.5R_M$. Examining the shower in the early part of development can provide a high level of position accuracy and two shower discrimination. Position resolutions of the order of a few millimeters have been obtained for few-GeV showers with a $3.5 \times 3.5\ cm^2$ segmented lead glass array [29]. Dependence of the resolution on the size of the transverse segmentation has been studied [30], and it was observed that, for energies > 20 GeV, the position resolution of an iron-scintillator calorimeter did not deteriorate when the width of a readout cell varied from 5 mm to 15 mm. Better spatial resolutions have been obtained by inserting a high resolution detector into the calorimeter at $\approx 5X_0$, where the early part of e.m. cascades occur. Using this technique, an spatial accuracy of $\approx 100\mu m$ was obtained for a 100 GeV shower [31]. With information on both the transverse and longitudinal shower development, the angle of incidence of a shower can be reconstructed. A typical angular resolution is $\sigma(\theta) \leq 20/\sqrt{E}$ mrad [32].

3.3 Hadronic Calorimetry

3.3.1 Hadronic Interactions

Hadrons, which are subject to the strong interaction, must interact hadronically if all their energy is to be absorbed in matter. After the strong

interaction takes place (through many secondary collisions) the absorption of energy becomes similar to that of electromagnetic cascades. The much more varied and complex particle-production mechanisms of hadronic showers, and the long interaction mean free paths, makes their development more complex. Also, because the elementary processes are not well understood, there is no simple analytical treatment of hadronic cascades.

When a hadron interacts with a nucleus, mesons are usually produced, π's, K's, etc. Half of the available energy in each collision is consumed in this type of particle production (the inelasticity K being ≈ 0.5), and the rest is carried by the forward-going leading particles. This hadron production is relatively insensitive to the type or energy of the incident hadron, and the multiplicity increases slowly with the atomic mass of the absorber. The excited nucleus releases energy by emitting nucleons and low energy photons and deposits its recoil energy by ionization. The hadrons produced in turn interact with nucleii and lose energy by ionization so the shower develops. The characteristic properties of hadronic cascade development are listed in Table 3.1 [26].

A sizable fraction of the secondaries produced in a hadronic interaction are π^0s; the fraction is typically 16-23% at 5-10 GeV and 40% at 50 GeV. The size of this π^0 component is greatly influenced by the nature of the first interaction, consequently event-to-event fluctuations about the average value are very important. Because π^0s decay immediately into two photons, which interact electromagnetically, there is therefore always an electromagnetic component to hadronic showers that fluctuates in size from event to event.

Table 3.1

Characteristic Properties of the Hadronic Cascade

Reaction	Properties	Influence on Energy Resolution
Hadron Production	Multiplicity $\approx A^{0.1} \ln s$ Inelasticity $\approx 1/2$	π^0/π^+ ratio Energy lost in breaking nucleii apart
Nuclear De-excitation	Fraction of excitation energy: Evaporation energy $\approx 10\%$ Binding energy $\approx 10\%$ energetic neutrons $\approx 40\%$ energetic protons $\approx 40\%$	Energy lost in breaking nuclear bonds Poor or different response to charged particles, neutrons and γ's
Pion and Muon Decays	Fractional energy of μ's and ν's $\approx 5\%$	Loss of ν's
Decay of c,b Particles from Multi-TeV Cascades	Fractional energy of μ's and ν's a few percent	Loss of ν's Non-Gaussian tails in resolution.

As can be seen in Table 3.1, although the energy dissipated by charged hadrons and electrons in ionizing the medium can be well sampled, a large fraction of the initial hadron's energy often is lost and cannot be measured (up to 40 % of the non-electromagnetic energy). For example, energy is required to break nucleii apart. This energy , which cannot be retrieved, is known as lost binding energy. Neutrons of several MeV energy, that are released during nuclear break up, have low interaction cross sections and consequently can escape detection. Many of the other non-relativistic particles that result from nuclear de-excitation, are not well measured because they do not escape the absorber material.

Another contribution to lost energy is recombination (LAr) or saturation (scintillator) effects in the sensitive material. These effects occur when a densely ionizing particle, such as a low energy proton, creates such a large number of ionization electrons that either the the electrons recombine with the ions in the active medium (LAr) or the saturation level of the scintillator is reached. Both of these conditions lead to nonlinearities in energy response. It should be noted that at low energies (< 2 GeV), where the cross section for multiple-pion production is small, the probability that charged hadrons lose their kinetic energy just by ionization of the medium increases greatly. This difference in production characteristics is expected to lead to non-linearities in response at low energy.

Neutrinos and muons from pion decay also contribute to unmeasured energy. As stated in Chapter 2, neutrinos escape detection completely because they only interact by the weak force. Muons are minimumly ionizing particles

and so deposit only a small amount of their energy in the active material of the calorimeter.

The energy dependences of the three principal processes of energy loss in hadronic interactions can be seen in Fig. 3.4. These plots show the relative contributions of electromagnetic showers, charged particles and the products of nuclear breakup to energy loss as calculated using three different simulation programs. The differences in the two results for protons illustrate the variation in the models used for describing hadronic cascades.

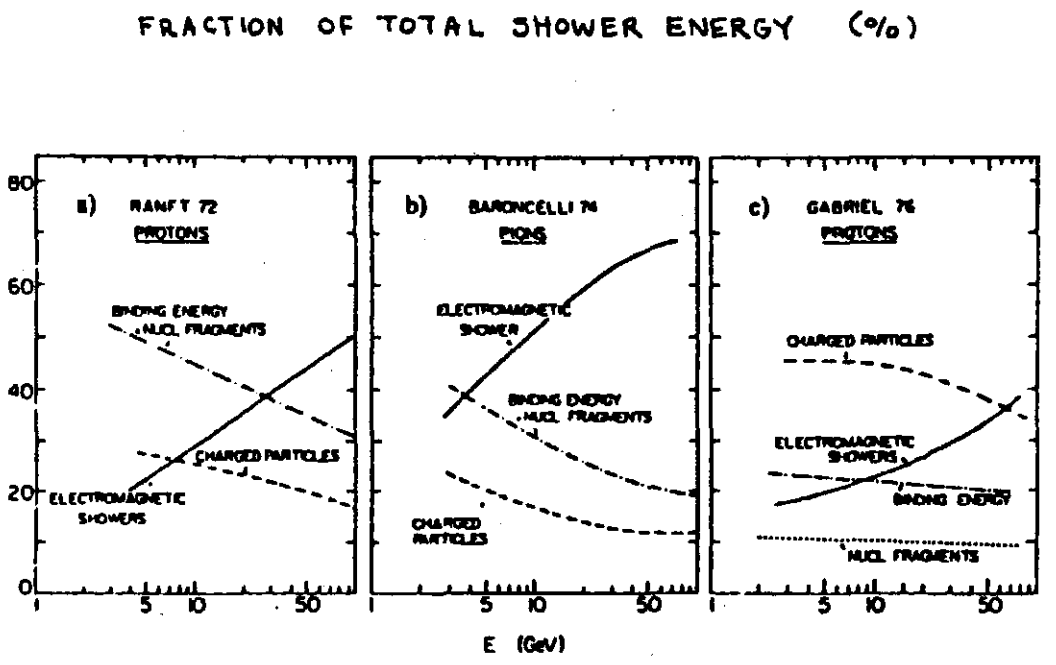

Figure 3.4 Relative contributions of the most important processes to the energy dissipated by hadronic showers as evaluated from three Monte Carlo calculations [33]

3.3.2 Characteristics of Hadronic Showers

Hadronic shower development is mostly based on nuclear interactions and consequently, the physical extent of the showers are expected to scale with the nuclear absorption length λ_{abs}. Because the hadronic cross section (σ) essentially is determined by the geometrical size of a nucleus, and since the interaction mean free path (λ_{abs}) scales as A/σ, where A is the atomic weight, λ_{abs} scales with the nuclear radius, as $A^{1/3}$. For uranium, the absorption length in centimeters is $\lambda_{abs} \approx 10.5cm$.

Figure 3.5 shows the average longitudinal and transverse distributions of hadrons in four different materials [26]. The longitudinal distributions have been measured from the starting point (interaction point) of the shower rather than the front face of the calorimeter. The resemblance to the longitudinal shape of electromagnetic showers and the scaling with λ_{abs} are evident. This shape results from the early rise in energy deposition due to the electromagnetic component of the cascade, followed by a slow decrease after the maximum where the energy loss is due primarily to ionization produced by the hadronic component of the shower. A common parametrization of this shape is the one given by Bock et al. [34]:

$$\delta E = \frac{E_0}{\Gamma(a)} w (bz_r)^{a-1} e^{-bz_r} b\delta z_r + \frac{E_0}{\Gamma(c)} (1-w)(dz_a)^{c-1} e^{-dz_a} d\delta z_a \qquad (3.6)$$

where E_0 is the incident particle energy, z_r is the distance from the origin of the shower in radiation lengths, z_a is that distance in absorption lengths, Γ is the gamma function, and a,b,c,d,w are the parameters to be fitted.

Figure 3.6 shows the longitudinal leakage as a function of detector depth

for a range of hadron energies. As for electromagnetic showers, relatively small increases in thickness are needed to contain higher energy showers [35]. An adequate expression that combines available data for 95% containment is:

$$L(95\%)_{av} \approx t_{max} + 2.5\lambda_{att} \tag{3.7}$$

where t_{max}, the position of the shower maximum, is measured from the face of the calorimeter in absorption lengths, and λ_{att}, which describes the exponential decay, goes as $\lambda_{att} \approx \lambda_{abs}[E(GeV)]^{0.13}$ [26]. Longitudinal containment is more important than lateral containment for hadrons, as it was in the case of electromagnetic showers.

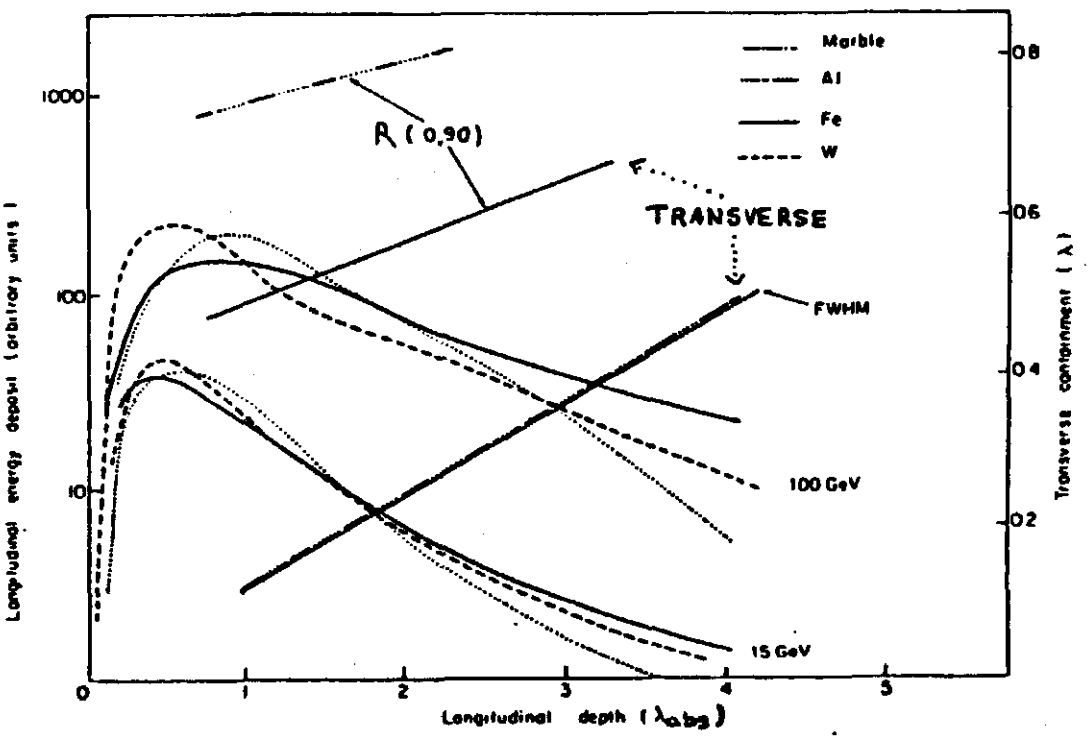

Figure 3.5 Hadron longitudinal shower development (left scale) showing approximate scaling in absorption length is shown, as well as transverse hadronic distributions as a function of shower depth (right scale) [26].

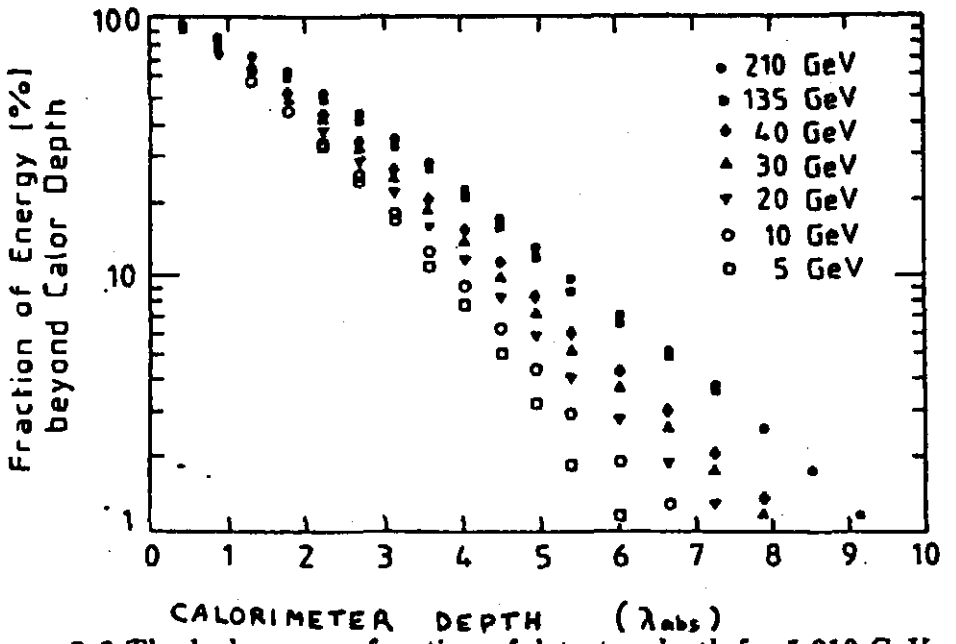

Figure 3.6 The leakage as a function of detector depth for 5-210 GeV pions as measured in a uranium/plastic scintillator calorimeter [22].

The transverse profile of hadronic cascades is also similar to that of electromagnetic ones. The transverse shape widens with depth into the calorimeter, and there is a narrow core that has a width that ranges from 0.1-0.5 λ_{abs}. This high energy core is surrounded by a halo of low energy particles that scatter out to quite large radii. The narrow core of hadronic showers, as measured by the FWHM (full width at half maximum) of the transverse distributions, also scales approximately as λ_{abs} as can be seen in Fig 3.5. This figure also shows that the radius of a cylinder needed for 90% lateral containment however, does not scale as λ_{abs}. For 95% lateral containment one needs a radius of $r \approx \lambda_{abs}$, and smaller values for high-Z material [28].

3.3.3 Hadronic Energy Resolution

As discussed in section 3.3.1, there is a sizable electromagnetic component in most hadronic showers and a large fraction of the initial hadron's energy is often not measured. Both of these facts play a significant role in the energy resolution of a hadronic calorimeter. In fact, fluctuations in the size of each of these components dominate the energy resolution. A major contribution to the fluctuations is amount of energy that goes into nuclear break-up. This can be attributed to the great variety of possible nuclear interactions. Another, less important factor, is the escape of secondary particles such as μs and νs due to incomplete shower containment. The combination of these effects are usually referred to as intrinsic fluctuations, and they contribute a term that scales as $\sqrt{E}$ for the total energy resolution.

The average number of π^0s in hadronic interactions are relatively small [28], so the fluctuations about this number are correspondingly large. For a complex calorimeter, the fluctuations in the location that the π^0 content of a shower begins contribute a non-Gaussian component to the energy fluctuation and a constant term in $\Delta E/E$ to the energy resolution. This term can vanish only if the calorimeter has an equal response to electrons and hadrons, $e/\pi = 1$, an attribute known as compensation.

There is of course a contribution to the energy resolution of hadron calorimeters from sampling fluctuations. This contribution is larger than that for electromagnetic showers observed in the same calorimeter. One reason is that the number of particles that contribute to a hadronic signal is smaller. This is because hadronic cross sections are small compared to electromag-

shown in Fig. 2.6, and discussed in section (2.2.3). The absorber plates for the modules in the 1990 test beam are constructed of depleted uranium or stainless steel, and the signal boards made from NEMA G-10. These signal boards are 5-layer printed-circuit boards with copper signal pads on the outer surfaces and signal traces on the innermost layer; the traces bring the signals from the pads to connectors located at the circumference of the module. Ground planes between the two outer layers and the innermost layer reduce crosstalk to a negligible level. The signal boards consist of 22.5° wedges that are assembled into disks and then covered with face-sheets of 0.5 mm thick G-10 that has been screen-printed with a thin layer of high resistivity carbon-loaded epoxy. This coat of epoxy serves as the positive high voltage electrode. The signal pads and absorber plates are at ground potential and the G-10 face-sheets serve as blocking capacitors. The operating voltage for the calorimeters is 2.5 kV, corresponding to a drift field of 1.1 kV/mm in the gap.

The ECEM electromagnetic module [44] is a disk of about 1 m in radius and 23.8 cm in depth. (See Fig. 4.2.) It provides full azimuthal (ϕ) coverage in the forward direction, where ϕ is the angle in the plane perpendicular to the collision or beam axis. The module subtends $2.1° < \theta < 26°$, where θ is the polar angle relative to the beamline; this corresponds to a range in pseudorapidity $1.45 < \eta < 4.0$. It consists of 18 sampling cells in depth that are read out in four separate longitudinal layers (ECEM Layers 1-4), having 2,2,6 and 8 sampling gaps respectively. Table 4.1 lists these depths in radiation lengths traversed at normal incidence. The transverse segmentation is in pseudorapidity and azimuthal intervals of $\Delta\eta \times \Delta\phi = 0.1 \times 0.1$, except in the third longitudinal layer (ECEM Layer 3), where, typically, 65 % of

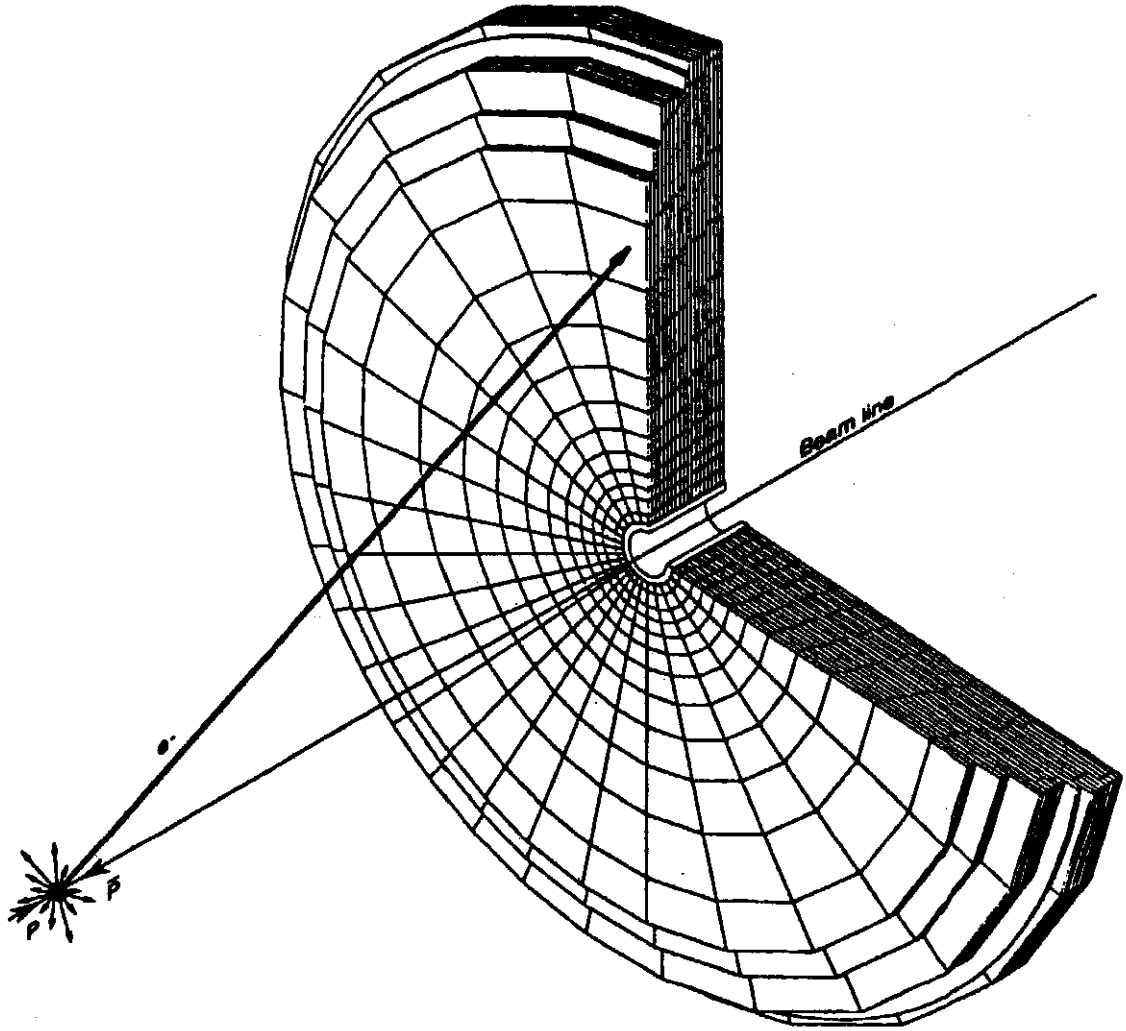

Figure 4.2 The End Calorimeter Electromagnetic Module (ECEM)

the shower energy is deposited, and where the segmentation is finer, $\Delta\eta \times \Delta\phi = 0.05 \times 0.05$, to provide better transverse position resolution. This segmentation is achieved using the copper electrode pads that are scribed on the signal boards. These electrodes are arranged in an almost projective manner, which lines up "towers" (all the signal pads at a given η and ϕ in one longitudinal layer) from the ECEM with those of the downstream ECIH hadronic module. These towers are considered semi-projective rather than projective because the same pad layout is used for pairs of adjacent read out boards (and for sets of four in the ECEM Layer 4). The boundaries between towers resemble staircases rather than continuous planes. The ECEM module was built as one monolithic unit to reduce the number of internal cracks which would cause nonuniformities in energy response. There are 7488 readout channels for each of the two modules of the D-Zero detector (North and South ends).

The first two absorber plates of the ECEM electromagnetic module, are made of 1.6 mm thick stainless steel (each about 0.1 radiation lengths) in order to be sensitive to particles that begin to shower in the walls of the cryostat upstream of the ECEM. All the other absorber plates are 4mm thick rolled depleted uranium (each of ~ 1.3 radiation lengths). The absorber and signal disks are supported by an aluminum tube surrounding the beam pipe. This tube is supported by a 2 cm thick stainless steel strongback that runs through the middle of the module and is attached to external mountings. A thin steel absorber disk is used instead of uranium behind the strongback, so that the average fraction of energy deposited in the argon for these two cells is the same as that in a normal uranium cell.

Table 4.1

Calorimeter Depths in Radiation and Absorption Lengths

module layer	radiation lengths	absorption lengths
ECEM layer 1	0.3	0.04
ECEM layer 2	2.6	0.10
ECEM layer 3	7.9	0.31
ECEM layer 4	9.3	0.39
Total ECEM	20.1	0.84
ECIH layer 1	30.9	1.3
ECIH layer 2	29.0	1.1
ECIH layer 3	29.0	1.1
ECIH layer 4	29.0	1.1
ECIH layer 5	35.1	3.8
Total ECIH	153	8.4

The thickness of the uranium plates and signal disks was measured using an ultrasonic probe at points on a 10 cm × 10 cm grid. The variation in thickness was found to be ~2.3% for the uranium plates and ~ 1 % for the signal disks. This information was used later for making local corrections to the response of the detector.

The ECIH inner hadronic module is a cylindrical unit with a radius of ~ 0.86 m and a length of ~ 1.7 m. (See Fig. 4.3.) It provides full azimuthal coverage (just like the ECEM module) and covers $2° < \theta < 22°$ ($1.6 < \eta < 4$) in angle from the beamline in the front and a different range $1° < \theta < 12°$

($2.25 < \eta < 5$) in the back, because of the thickness of the module. This module consists of five longitudinal layers; the first four layers (ECIH Layers 1-4) are comprised of 15, 6 mm-thick absorber plates made of a depleted uranium and 2% niobium alloy. The fifth layer (ECIH Layer # 5) is constructed from thirteen, 46.5 mm stainless steel absorber plates, and consequently provides a far coarser sampling of particle energy. Table 4.1 lists the depths of these layers in absorption lengths. These uranium absorber disks are comprised of two semicircular plates, with half-disks joining alternately in the horizontal and vertical plane along the stack. The transverse segmentation of the ECIH is in pseudorapidity and azimuthal intervals of $\Delta\eta \times \Delta\phi = 0.1 \times 0.1$ throughout the module, and has the same semi-projective geometry as the ECEM electromagnetic module. There are a total of 10,432 readout channels for each ECIH module.

The ECMH middle hadronic module is a wedge-shaped module about 1.5 m in length. (See Fig. 4.3.) In the full D-Zero end calorimeter, 16 of these modules completely surround the ECIH hadronic module, but in the test beam, as we indicated, the ECMH module was placed directly on the beam axis behind the ECIH module. The ECMH has the same material configuration as the ECIH. Because the ECMH module is smaller, traces on the same plane as the signal pads, rather than multilayer signal boards, are used to bring out signals to the edge. This module has 3712 readout channels.

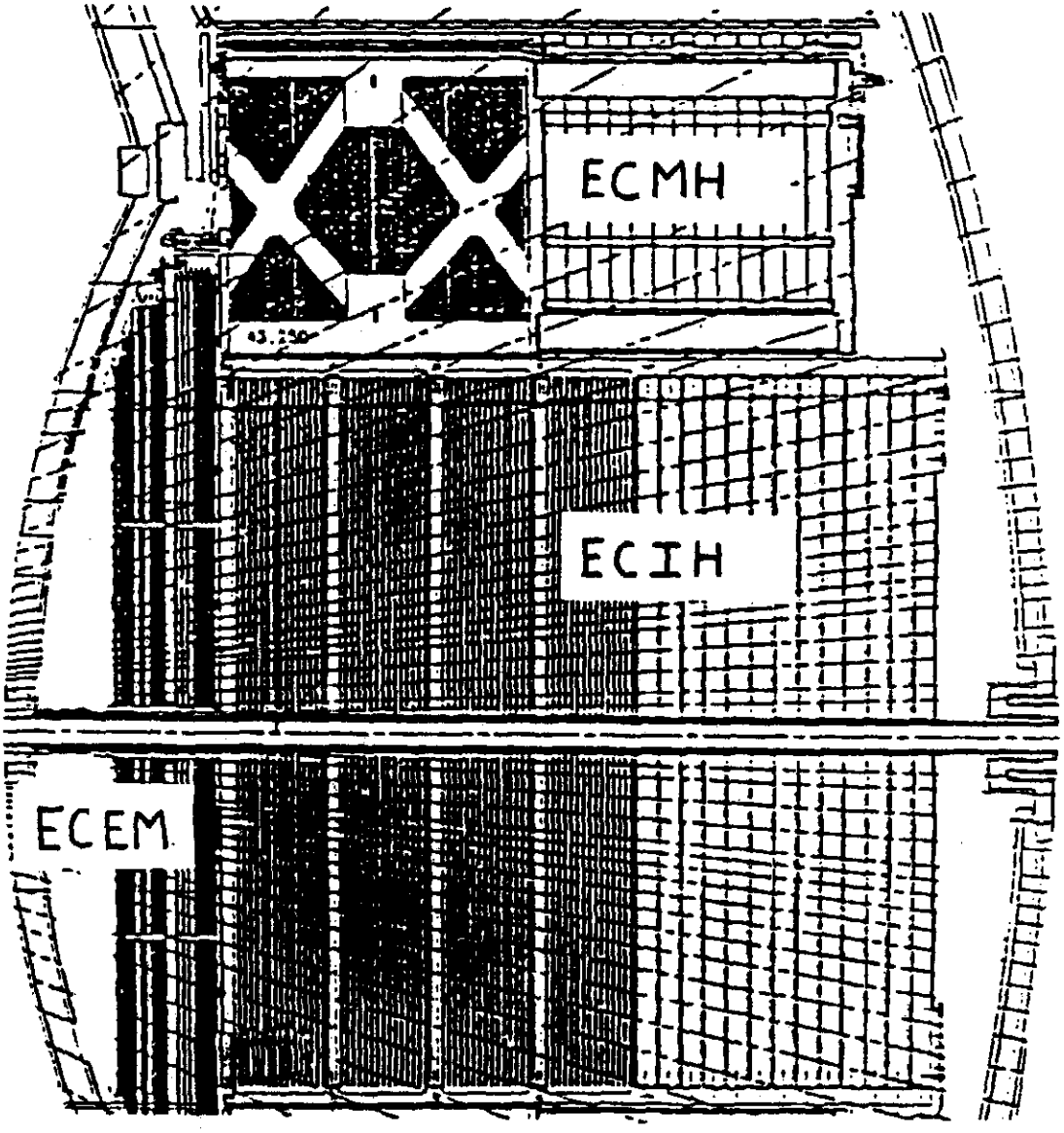

Figure 4.3 The End Calorimeter Inner Hadronic Module (ECIH) and the End Calorimeter Middle Hadronic Module (ECMH) in the D-Zero cryostat

4.2 The Neutrino West Beamline

The D-Zero test-beam calibration studies were carried out in the Neutrino West Area A (NWA). A schematic of the beamline is shown in Fig. 4.4. Beam momenta between 10 to 150 GeV/c were used in this study. The beam had negative polarity; e^-, π^- and μ^- particles were available. The beamline begins at the NW1W dipole where 800 GeV/c protons extracted from the Fermilab Tevatron are made to collide with an aluminium production target in the NW3 enclosure. The maximum allowed flux of protons on the target was 5×10^{12} protons/spill; the limit was based on the heat capacity of the target [45].

The beamline has two double bends in the horizontal plane that determine the momentum of the beam, this momentum selection is done by the dipole magnets NW4W, NW6E, NW7W and NW9E. Vertical corrections can be effected using trim magnets located in enclosures NW4, NW6 and NW9. There are two quadrupole (focusing) elements, one in NW4 and one in NW8. The beamline also contains NW4S, a magnet used to deflect particles out of the beam (referred to as a sweeper magnet), horizontal and vertical collimators and three remotely controlled target wheels that contain sheets of lead: NW4PB, NW6PB, and NW7PB. The EPICURE control system [46] was used to run the beam transport systems and most of the beamline instrumentation. Magnet currents were recorded during beam-spill, and other device settings at the start of each data run.

To reduce the electron content, and thereby increase the pion content of the beam, ~ 1.6 mm lead plates were placed in the two target wheels furthest

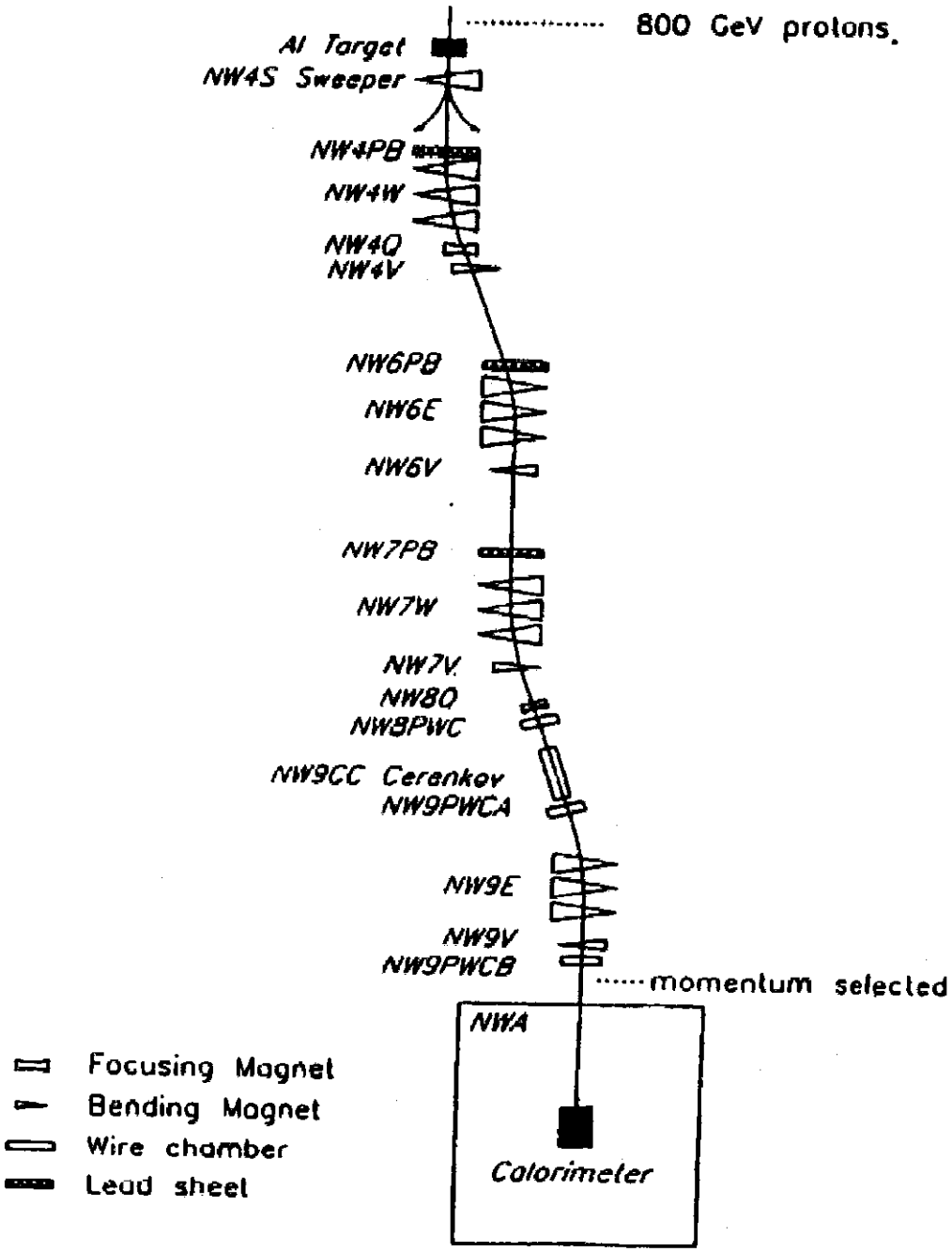

Figure 4.4 A schematic of the NWA beamline

downstream from the production target. The consequent multiple scattering also reduces the pion intensity by a factor of 20 or more, so, for energies below 25 GeV, only the furthest downstream plate was placed in the beam. To create a pure electron beam at NWA was more complicated. The sweeper magnet had to be turned on and set to sweep away all charged particles. A lead target was placed in the secondary beam just downstream of this sweeper magnet to convert photons in this beam to electron-positron pairs. No other lead targets were placed in the beam.

Several scintillation counters are located along the beamline to measure the beam intensity, and SWICs (Segmented Wire Ionization Chambers) were used to monitor the beam profile. There are also two helium Cherenkov counters (NW9CC and NWACC) that were used to identify electrons. During the 1990 test beam operation, three scintillation counters located in front of the cryostat in NWA hall were used in coincidence, and a counter that had a 5×10 cm^2 hole was used in veto, to form the primary trigger. Also included in the trigger was an array of scintillation counters to tag particles in the beam halo, a large area counter (called a MIP-for minimum-ionizing particle-counter) directly downstream of the cryostat to tag energy leakage, and another such counter further downstream behind a 3 meters thick block of steel to tag muons downstream of the cryostat.

With the exception of special muon runs, most of the data were taken over a 22 second beam spill with the instantaneous rate restricted to a few thousand particles per second. The intensity was kept at this level to limit the effects of pileup observed in the high intensity runs [47].

The mean momentum of the beam was determined from the current setting in the last bending magnet NW9E, and it was measured by the bend angle observed for any beam particle, obtained from the beam PWCs (Proportional Wire Chambers) positioned upstream and downstream of this magnet (NW9PWCA and NW9PWCB). The average momentum of the beam is given by [45]

$$p(GeV/c) = \frac{B \times L}{517.02 \times \sin\phi} \tag{4.1}$$

where B is the magnetic field in kilogauss, L is the effective length of the magnet in cm and ϕ is the bend angle of the beam in radians ($\approx$ 28.68 mr for the NW9E setting). The magnetic field B was measured by a Hall probe inserted into the magnet. These Hall probe measurements agree to well within 1% with NMR (Nuclear Magnetic Resonance) measurements of the magnetic field carried out during the 1987 test-beam run at NWA [48]. The precision of the momentum measurement on an event by event basis was about 0.25% [49]. The root-mean-square spread in the beam momentum was 1.5%, with essentially Gaussian profiles of 1.5 cm and 1.1 cm standard deviations in the horizontal and vertical directions, respectively.

A series of PWCs were located along the beamline to record beam particle trajectories for each event (NW8PWC, NW9PWCA, NW9PWCB and chambers in NWA). These were Fermilab standard "Fenker" chambers which were read out using a CAMAC latch system [50]. Each chamber had either one or two planes of 128 wires with 1 mm spacings; not all the wires in each plane were instrumented. There were a total of 11 planes, 5 for recording horizontal and 6 for recording vertical positions of trajectories. The chambers were surveyed in position, and their relative alignments were verified using particle

beam trajectories. Two planes of PWC were attached to a positioning table on the cryostat. This table moved in two orthogonal directions relative to the cryostat, and for certain settings of the cryostat, was therefore tilted out of the plane normal to the beamline. Each of these PWC planes was instrumented with 128 channels of electronics, and provided verification of the position of the cryostat with respect to the beamline.

4.3 The Cryostat and Transporter

The beam entered the double-walled cryostat through a specially designed thin entrance window, consisting of two 1.6 mm steel plates. The cryostat was mounted on a motorized, computer-controlled transporter system that was capable of the range of motion listed in Table 4.2. (See Figure 4.5.) The range of motion was chosen such that the beam could be directed into the modules along the wide range of trajectories expected in the D-Zero experiment (for a distribution of interaction vertexes of ± 30 cm about the center). Specially designed flexible conduits were used for the signal and high voltage cables to provide this wide range of motion. The control system for the transporter was PC-based. Given any desired D-Zero coordinates, the system was used to calculate and execute the required motions.

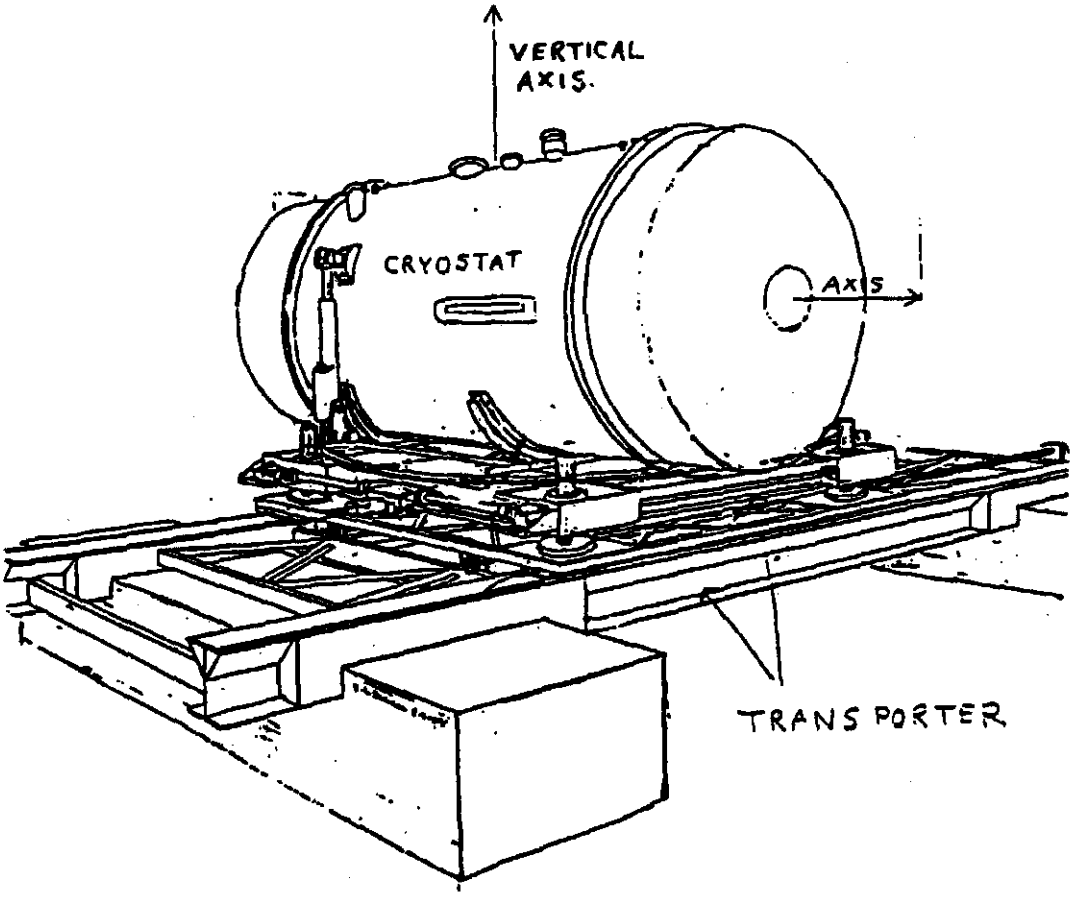

Figure 4.5 A sketch of the test-beam cryostat and transporter

Table 4.2

Ranges of Motion of the 1990 Test Beam Transporter

rotation about cyostat vertical axis	azimuthal rotation about cryostat axis	horizontal translation	vertical translation
190°	±15°	3.5 m	0.75 m

The cryogenic system was designed to supply the cryostat both with high purity liquid argon, and with liquid nitrogen that was used for its cooling. The system maintained the argon temperature to within ±1 K of the nominal temperature of 90 K, and the pressure within ±0.5 psi of the nominal 20 psi(a) throughout the run. The temperatures of the modules and of the cryostat were monitored during the cool down and data-taking using approximately 70 resistive temperature sensors located at various positions within the cryostat. It took on the order of four days to cool down the modules.

Argon purity was monitored using eight test cells, located in pairs, at four different locations in the cryostat. These cells contain radioactive sources that created ionization within the separate argon gaps. Each pair of cells included an "α cell", consisting of an ^{241}Am source and a single 2.3 mm argon gap in which the emitted α particle deposited all its energy, and a "β cell", consisting of a ^{106}Ru source, and two 2.3 mm argon gaps, one of which was used as a trigger for reading out the ionization deposited in the first gap. The complete purity monitoring system is described elsewhere[51]. The argon purity can be deduced from the ionization signal observed in these cells.

The percent changes in the responses of the α cells at a field of 13 kV/cm, from the start to the end of the run, are given in Table 4.3. The differences in the uncertainties for the four cells is due to variations in the local noise characteristics of the sensors and of the preamplifiers. A weighted average of the four values shows less than 0.25% loss of signal at the 95% confidence level over the duration of the run. The Table also lists the percent changes in the ratios of responses of the β cells at fields of 0.8 kV/cm to those at 10.9 kV/cm. Such ratios are used to minimize any effects from changes in pile-up rates for the ^{106}Ru sources over the course of the experiment (the β-source has a lifetime of days). The average of the ratios was observed to decrease by 0.9% over the duration of the run. This corresponds to a less than 0.1% loss of signal at a field of 10.9 kV/cm [51]. Because the voltage response of the calorimeter and that of the β cells is quite similar, the loss in calorimeter response was therefore assumed to be $\leq 0.1\%$ [52]. A comparison of α and β response as a function of oxygen contamination of the liquid argon indicates that the 0.25% loss for the case of ^{241}Am corresponds to 0.1% loss in β signal. (Oxygen in the liquid argon would cause a loss of signal because oxygen has a high electron affinity, and consequently has a tendency to combine with the ionized electrons.) The shape of the observed β response function corresponds to a an effective oxygen content in the LAr at the end of the run of < 1.0 ppm [52].

Table 4.3

Change in α and β Test Cell Response During the 100 Day Run

sensor pair	percent change in alpha response	percent change in beta response
1	-0.05 ± 0.11	-1.2 ± 0.5
2	+0.25 ± 0.89	-0.9 ± 0.1
3	-0.31 ± 0.13	-0.8 ± 0.5
4	-0.05 ± 0.11	(cell failed)
Average	-0.12 ± 0.07	-0.9 ± 0.1

4.4 The Electronics

Because of the lack of a sufficient number of amplifier channels for the test, only a fraction of the module array examined at the test beam could be instrumented. The fully instrumented region covered the full effective range of pseudorapidity, and $\approx 35°$ of azimuthal angle for the ECEM and $\approx 46°$ for the ECIH module. In addition, a border region surrounding these areas had the channels ganged together to gauge the effects of energy leakage. Also instrumented at all azimuths was the area around the beam pipe, as shown in Fig. 4.6. Our coverage was thought to be sufficiently large for containing hadronic showers and for measuring energy leakage in the region of the beam pipe. There were a total of $\approx$ 1450 ECEM channels, $\approx$ 2400 ECIH channels and 120 MH channels, which represents about 10% of the number of calorimeter channels in the full D-Zero detector.

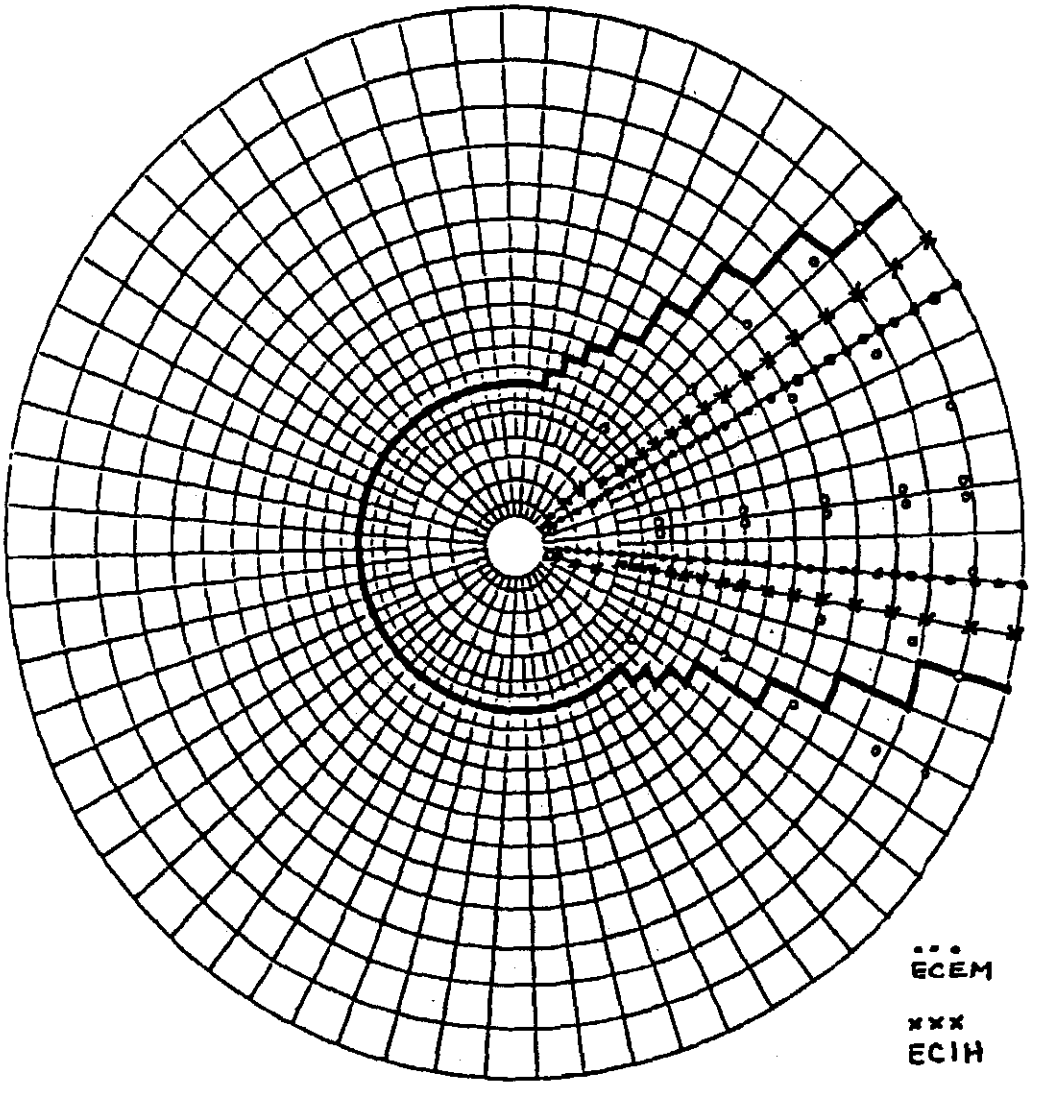

Figure 4.6 Outline of the instrumented region of the ECEM and ECIH

Calorimeter signals were brought out of the cryostat through feedthrough ports. The coaxial readout cables used inside the cryostat were the same length as those used in the D-Zero calorimeter. Before exiting through these ports, the signals were rearranged within the cryostat according to their location in the calorimeter, so that signals from towers that were physically close could appear near each other on the outside cables. In particular, the signals were arranged so that all the readout pads in a $\Delta\eta \times \Delta\phi = 0.2 \times 0.2$ semi-projective tower exited on two adjacent multiconductor cables, which facilitated the formation of a fast trigger. Signals from two η,ϕ towers can be transmitted on a single multiconductor cable. On the external side of the port, short cables were used to connect the feedthrough lines to low-noise hybrid charge-sensistive amplifiers (refered to as preamps). Two different kinds of preamps were used for matching the signals, one with a 5 pF feedback capacitor and one with a 10 pF capacitor. The 10 pF version was used for ECEM layers 3 and 4 where the largest signals occur.

The voltage outputs of the preamps were fed on twisted-pair cables into baseline subtractors (BLS)[53], which are shaping and sampling circuits. The shaping consisted of 430 ns integration and a 33 μs differentiation of the signal. There was also a gain of three provided to change the full scale from 3.3 volts at the output of the preamp to 10 volts at the sampling stage. The resulting shaped signals peak between 2 and 2.4 μs and have relatively broad maxima at 2.2 μs. The next step in signal processing involved dual sampling of the signal for performing a baseline subtraction. Two analog memory-cells were used to monitor the signal, and when a trigger was registered by the scintillation counters in the beam, the signal was sampled. One memory-cell

sampled the baseline before the delayed calorimeter signal had a chance to rise, and 2.2μs later, the second memory-cell sampled the peak of the signal. The differences between these baseline and peak signals were sent to the 12-bit analog-to-digital coverters (ADCs).

An effective dynamic range of fifteen bits was obtained for the 12-bit ADCs through the use of precision $\times 1$ or $\times 8$ amplifiers. Different gains of the amplifiers were used depending on the amplitude of the signal. When the input signal was less than 1.25 volts, it was amplified eightfold, and the result was digitized by the 12 bit ADC ($\times 8$ mode). If the signal was larger, then it was digitized directly without analog gain using the $\times 1$ amplifier, and the resulting ADC output was shifted up digitally by 3 bits, or in effect multiplied by eight ($\times 1$ mode), thereby achieving additional dynamic range. Because the amplification is done differently in each mode, and the ADC and BLS pedestals are different, the total pedestal levels also differ for each mode. (The pedestal level is the background electronics noise per channel.) Although the ADCs could perform pedestal subtraction and zero-suppression* directly for each channel, these functions were performed offline in this test-beam run. Each ADC card had 24 input channels that could process signals simultaneously in about 10μs. This was repeated 16 times to digitize all the channels utilizing one ADC card. The ADCs were housed in a VME crate that read the ADC outputs into a VME buffer, which drove a data cable. The data cable carried the data to dual-port memories of four DEC Micro Vax-II computers. This

* Zero-suppression is the process of eliminating channels, whose energy values are within a given range of their pedestal values, from the total energy sum.

system is similar to the full D-Zero electronics readout system which has been detailed elsewhere [54,55].

The D-Zero electronic system was designed to assure that both random and coherent noise remain low. This is important in a system with a large number of channels. The fluctuations in the signal obtained from summing N channels depends on the random noise of each channel, which can be assumed for simplicity to be the same for each channel, and the cross-correlation between pairs of channels: [54]

$$S^2 = N\sigma^2 + N(N-1)c^2 \tag{4.2}$$

where S^2 is the square of the signal fluctuation, σ^2 is square of the random noise and c^2 reflects the cross-correlation. As N becomes large, the second term, known as the "coherent noise" term, grows faster than the "random noise", and the two terms become equal when $N \approx \sigma^2/c^2$ channels are added together. The RMS noise voltage, σ, measured by the ADC is proportional to the noise density and the bandwidth of the system, and is linear in the total detector cell capacitance [54,56]. The random noise per channel measured with the high voltage across the LAr readout gaps turned off, corresponds to about 150-200μV at the output of the preamps. One ADC count is approximately 100μV, which represents an ionization charge of 3000 electrons at the preamp input. (A 1 μV signal corresponds to 30 electron charges.) With the high voltage turned on, the standard deviation of the random noise per channel increases because of contributions to the noise from channels that have uranium absorber, which produces ionization in the gaps. The coherent noise, c, is kept to the level of 5-7μV per channel, which corresponds to about 150

electrons per channel at the preamp input. Therefore, 600 - 1600 channels can be added together, before the coherent noise starts to dominate. A typical electron shower contains 100 pads with signals above our zero-suppression threshold; a hadron shower contains 400 such pads. Consequently, coherent noise should not limit the response of the system.

4.5 The Data Acquisition System

The D-Zero data acquisition system used during the beam tests and for D-Zero is divided into four main parts: a Level-1 trigger, a Level-2 filter processor system, a data logging system, and front-end systems connected by a communications bridge known as a token-ring. In order for the entire system to function properly, resources within these systems have to be allocated and coordinated instructions have to be downloaded to them. A detached process, running on the data acquisition computer called COOR [57], performs this allocating and coordinating function. The user communicates with COOR via an interface program called TAKER [58], which is the general data taking task. TAKER selects predefined trigger configurations, sets the lengths of runs, and controls whether the data will be recorded. TAKER communicates with the "Data Logger" and the Comm_TKR process via COOR. The Data Logger receives events from the Level-2 system, writes them to disk, and, when the files are of appropriate size or when it is requested, spools those files to tape.

Events are stored using the ZEBRA utility package from CERN [59]. ZEBRA provides dynamic data storage and management in a Fortran environment. The Data Logger also sends some portion of the data to the "global

shared common" area in memory, so that events can be examined online. Comm_TKR conducts token-ring communication on behalf of COOR, doing address translation and formatting the information that needs to be downloaded. TAKER also communicates via COOR with programs running in the trigger control computer and the Level-2 supervisor. Though no Level-2 filter was used during the 1990 test-beam run, nevertheless, several filter prototypes were tested.

Begin and end of run records were appended to every data run as Run Control Parameter banks (RCP), a special type of ZEBRA storage bank. These records included trigger information from TAKER, other information requested by TAKER, beam status information from the EPICURE system, readings of the calorimeter voltage and currents, temperatures of various electronics racks, temperatures of calorimeter modules and other pertinent information. All this information was also written to a database where subsequent searches could be made to select any particular runs for further study.

The standard code for online monitoring and analysis of data is a menu driven program called EXAMINE [60]. This code can read data either from the global shared common area on the data acquisition machine or from a file on disk. Figure 4.7 shows the data flow between EXAMINE and the data acquisition system when studying data online. COOR maintains a list of the triggers selected by TAKER. EXAMINE must stipulate what triggers are to be received. The EXAMINE program is composed of a frame which calls nine "hooks" in a well defined sequence. At each of these hooks is a set of routines called a "package" that performs a certain task. In order to keep

the code as compact as possible, the total number of hooks used depends on the particular analysis performed. The functions of these hooks can be divided into: beginning the program, operations that have to be completed before looping over events, the event loop, operations that are performed after the event loop, and ending the program. The EXAMINE frame also sets up standard common blocks needed to store the data during the analysis process.

In order to assure the quality of the accumulated data, EXAMINE was used online on a DEC Vaxstation during the operation of 1990 test beam. A user could choose to look at histograms of energies deposited in particular layers of the calorimeter, or summed energies, or energies for different pseudo-rapidities or azimuthal angles, or PWC hit profiles or a three-dimensional color display of the calorimeter. In addition, a hard copy of a predetermined set of histograms was printed at the end of each run, and filed for later reference.

An alarm monitoring process was on at all times, and sent messages to a devoted terminal when any parameters read by the Control Data Acquisition system (CDAQ) [61] exceeded certain preset bounds. The high voltages settings on the resistive layers of the calorimeter and their respective currents were monitored by a standalone system consisting of three PCs (Personal Computers), various switch boxes and 18 "Droege" high voltage power supplies.

Runs to determine the background ADC counts in each electronics channel, without beam, but with the high voltage turned on, known as pedestal runs, were taken once every eight-hour shift. A program named CALIB was used to analyze these pedestal runs. CALIB also functioned as the TAKER

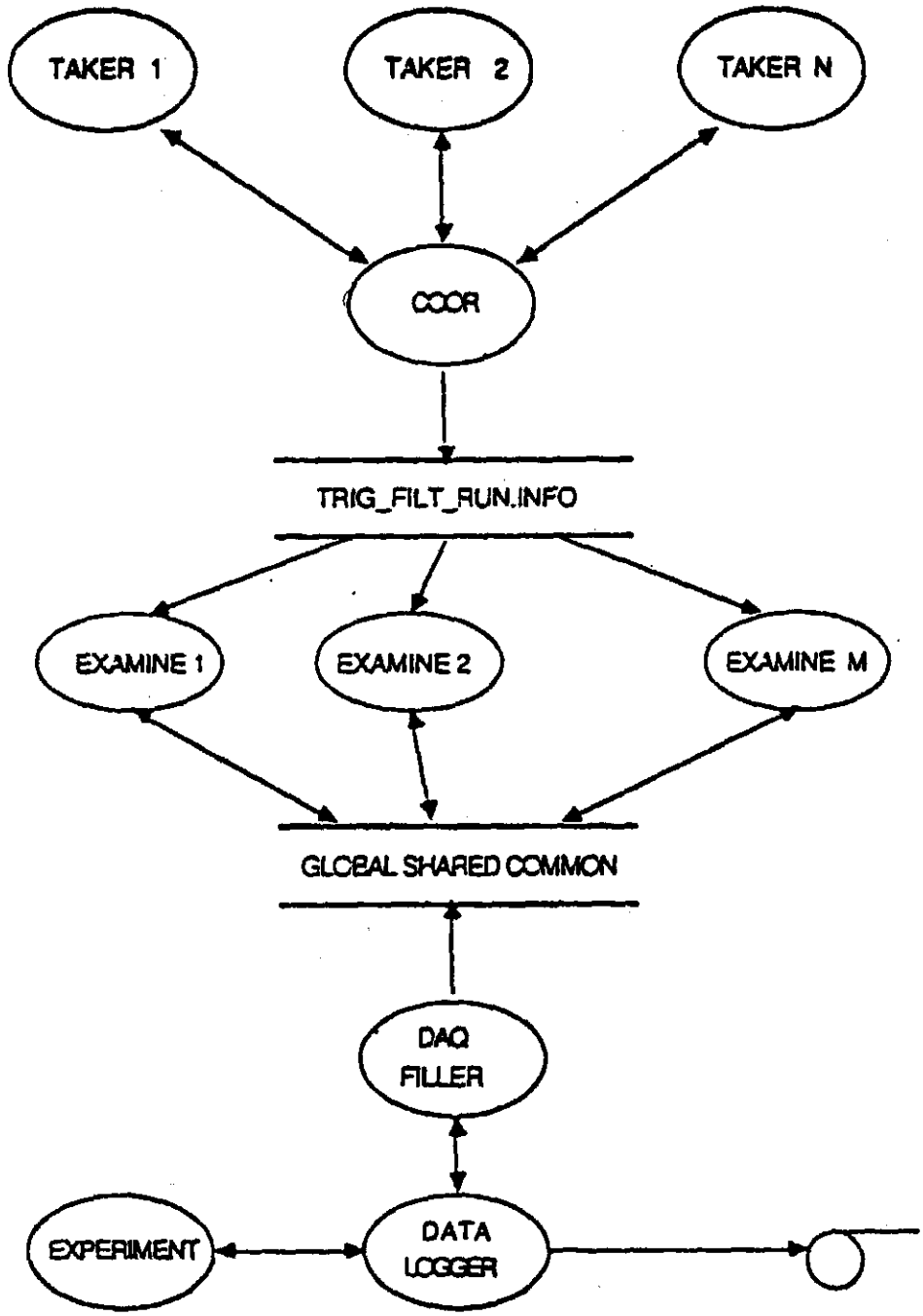

Figure 4.7 A flow diagram of the D-Zero data acquisition system

for pulser runs used to determine the gains of the channels. Pulser runs were taken every 24 hours. The pedestal runs were taken in what is called double-digitized mode, where all the channels were read out both in $\times 1$ and then $\times 8$ mode independent of the magnitude of the pedestal. The observed pedestal levels were stable to within 1 ADC count.

About halfway through the running period it was decided to also take separate pedestal runs for the two modes because a mean drop of the order of 1/2 ADC count was noted in the $\times 8$ pedestal values per channel as a function of readout time. (This effect was caused by a faulty power supply in the ADC crate.) A comparison of these single-mode pedestal runs to the doubly-digitizing runs determined a parametrization that was used to correct the doubly-digitized pedestals [62]. This was necessary since the doubly-digitized pedestals were used most often in the analysis of the data. The so-called in-spill pedestals were also taken for the second half of the run. These were pedestals taken during the data taking in the $\times 8$ mode, and recorded with the data. Wherever possible, in-spill pedestals were used when the data was processed to create data summary tapes (DSTs) for analysis.

4.6 Detector Calibration

One of the primary aims of the 1990 test beam was to calibrate the performance of the three calorimeter modules. The goal was to establish the absolute energy calibration to better than 1% accuracy, and to transfer this calibration to D-Zero. To achieve this, a precision resistor (0.1% tolerance) was connected to the input of each preamp channel to measure of the relative response of all channels to a pulser system [54,63]. This system consisted of a

current source, an attenuator box (to control the amplitude of the deposited charge), and a switch box. During each calibration run, the pulser system was stepped automatically through 32 switch positions corresponding to 144 channels of the calorimeter, all of which were tested at one time.

For an input voltage at the preamp of $V(t)$, the output voltage is given approximately by [54]:

$$V_{out} = \frac{\int V(t)dt}{RC_F} \frac{AC_F}{AC_F + C_D} \tag{4.3}$$

where C_F is the feedback capacitance, C_D is the detector capacitance, R is the feedback resistance, and A is the DC open-loop gain of the preamp (see Fig. 4.8). Values of $R = 499k\Omega$ for the channels with a feedback capacitance of 5 pF, and $R = 249k\Omega$ for the channels with a 10 pF capacitance, were used to ensure a nearly equal response for all the channels. The detector capacitance C_D ranged from 1.5 to 5.0 nF, and the open loop gain A was approximately 5000.

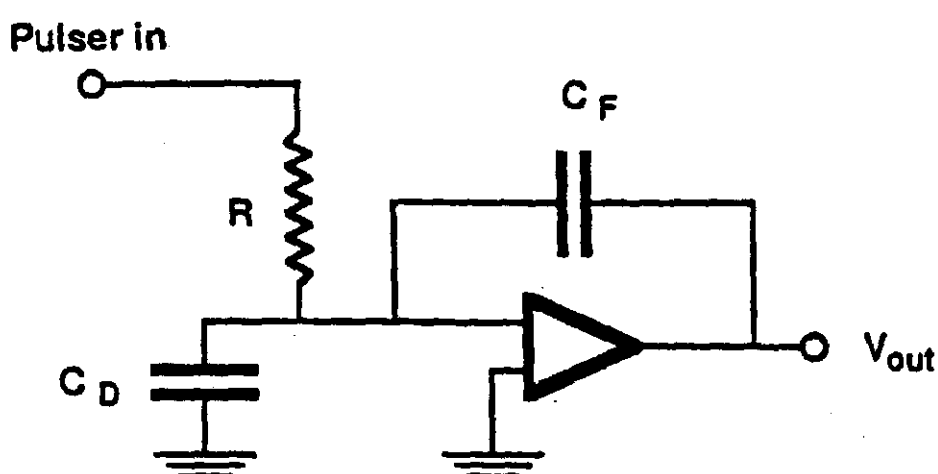

Figure 4.8 A schematic of the pulser input to the calorimeter preamp

The width of the pulser pulses was about 300 ns. The uniformity of the pulser distribution was found to have an rms of about 0.1%. The relative timing accuracy for the full system was ±10ns, which leads to an uncertainty in the measured gain of less than 0.2% per channel. Gains were obtained for each channel in both ×8 and ×1 modes.

The linearity of the gains was studied by taking pulser runs at various attenuator settings. The output ADC values, corrected for the detector and feedback capacitances, were plotted as a function of pulser amplitude, and the results fitted to a straight line. The pulser covered an energy range of 2.5 to 50 GeV. The deviations from a fit to a straight line for all the channels were less than ±0.25%, and the channel-to-channel relative response for a given amplitude had an rms spread of about 2.3%. During the second half of the run, (≈50 days), pulser events of a group of 144 channels were used to study gain stability. The rms gain variation over this time was observed to be about 0.8%. A correction to remove temperature dependences was applied using the BLS and preamp crate temperatures recorded throughout the run [54,64]. With this temperature correction, the gain variation was reduced to 0.2%.

After establishing the absolute energy gain of the calorimeter electronics, the calibration had to be transferred to D-Zero. Because of the differences in the test beam and D-Zero electronics systems, a reliable cross-calibration was needed [65]. A movable test station with its own pulser system was built for this task. The cross-calibration can be obtained by collecting complete sets of pulser data using this test station at both the test beam and at D-Zero. Because the ratio of the response of the calorimeter to a particle at the test

beam, relative to that of the test-beam electronics to a pulse from the pulser, can be determined to an accuracy of better than 0.1%, the response of the calorimeters at D-Zero can therefore be determined accurately from the data collected using the test-station pulser [54].

CHAPTER 5

ANALYSIS OF SHOWER SHAPES AND POSITION RESOLUTION

As stated in the previous chapter, one of the important goals of the D-Zero test beam was to determine the shapes of electromagnetic and hadronic showers in the D-Zero end calorimeter. A complete understanding of the shower profiles is important for several reasons. First, one can use the distinctive shower shapes of electromagnetically and hadronically interacting particles to recognize and distinguish between the two types of particles. Secondly, knowledge of the profiles enables one to understand the energy overlap of showers initiated by particles that are closely spaced apart. Shower profiles can also be used to improve the energy resolution of calorimeters by exploiting the fact that the shapes depend upon the particle energy.

Information about the shower shapes can be used to calculate the impact position of the particle that created the shower. Accurate determination of the impact position of particles in the calorimeter is important for several reasons. Through the matching of tracks in the central tracking system with impact positions in the calorimeter, the detector alignment can be understood. The impact position of neutral particles such as photons or π^0's can only be determined using the calorimeter. Good spatial resolution is important for the determination of the invariant mass of particles such as $J/\psi \rightarrow e^+e^-$.

Proper simulation of calorimeter response is of major importance in high energy physics experiments. It is crucial that a simulation correctly model the shape of particle showers in the calorimeter in order to gauge effects on resolution and signal that depend on the specific calorimeter configuration, on energy leakage out of the detector, or on variations in thickness of absorber or active material. The shower parametrizations used in the simulations of showers to determine such effects must therefore be chosen with care. A detailed description of the Monte Carlo simulations used in this analysis is given in Appendix A.

An analysis of the profiles of electron and pion showers observed in the 1990 D-Zero test beam data will be presented in this chapter. The methods used in the analysis will be discussed in detail. In particular, we will concentrate on the measurement of transverse profiles and on the determination of the positions of impact of particles based on these profiles. Several methods for determining position were investigated for both electrons and pions and the results will be presented below. The dependence of the spatial resolution on a particle's energy and angle of incidence will also be shown. In some cases, the identical analysis was performed, on simulated data samples. Comparisons of the results from simulations and from test-beam data will be presented throughout the chapter.

5.1 Analysis of the Shape of Electromagnetic Showers

The electron data used in our analysis have undergone several processing steps. First the individual ADC output channels are corrected for electronic pedestal fluctuations and amplifier gain variations, which were described in the

previous chapter. Next, channels that contained signals within one standard deviation of their pedestal value were ignored. (This is known as "one-sigma zero-suppression".) Such data, together with information about the reconstructed beam tracks observed in the PWCs for each trigger, were written to files called Modified Data Summary Tapes (MDSTs). The MDST data were then processed further in preparation for the shower-shape analysis.

In the next step of processing, only signals in ECEM layers 1-4 and ECIH layer 1 that were located within a given η and ϕ range were included in the sums of the total electromagnetic energy. The relative weights given to signals in each longitudinal layer were determined from fits to the data [44,52]. The accepted η and ϕ ranges were varied with the η of the incident particle, so as to account for geometrical differences in shower position. Events with more than one track detected in the PWCs, or events with ambiguous information in the tracking data, were removed to ensure that only single particles entered the calorimeter. A cut on beam momentum was also implemented such that only particles with a momentum within 5% of the expected value were passed. The final criterion involved accepting only those events where the energy outside of the shower's η and ϕ range, in a border region of $\Delta\eta = \Delta\phi = 0.1$, was less than 200 ADC cts (260 ADC cts corresponds to 1 GeV). This was to ensure that the particle shower was well contained within the chosen (η,ϕ) range. On the average, 75% of the data passed all these requirements.

5.1.1 Longitudinal Shape of Electromagnetic Showers

The longitudinal shape of the electromagnetic showers was examined by studying the average energy deposited in each of the four longitudinal layers of

the ECEM, $\langle E_{layer} \rangle$. The energy deposited in the ECEM layers 1-4 and ECIH layer 1 and the total energy in the ECEM and ECIH layer 1 combined for 100 GeV electrons at $\eta = 2.3$ and $\phi = 3.0$ rad, namely 8.4° above the -x axis, are shown in Fig. 5.1. The asymmetric energy distributions in each layer introduce errors in determining the mean energy per layer. The average energy was compared to the average total electromagnetic energy of the shower, $\langle E_{total} \rangle$, in terms of the ratios $R_{layer} = \langle E_{layer} \rangle / \langle E_{total} \rangle$. Figure 5.2 shows a plot of this energy ratio for ECEM layers 1-4, for six different beam energies between 10-150 GeV, at $\eta = 2.3$, and $\phi = 3.0$ rad. Typically, the statistical errors are smaller than the data points. Leakage into the first hadronic layer (ECIH layer 1) was less than 2% at all energies. For all energies the shower maximum occurs in ECEM layer 3, and consequently the ratios are nearly energy independent for that layer.

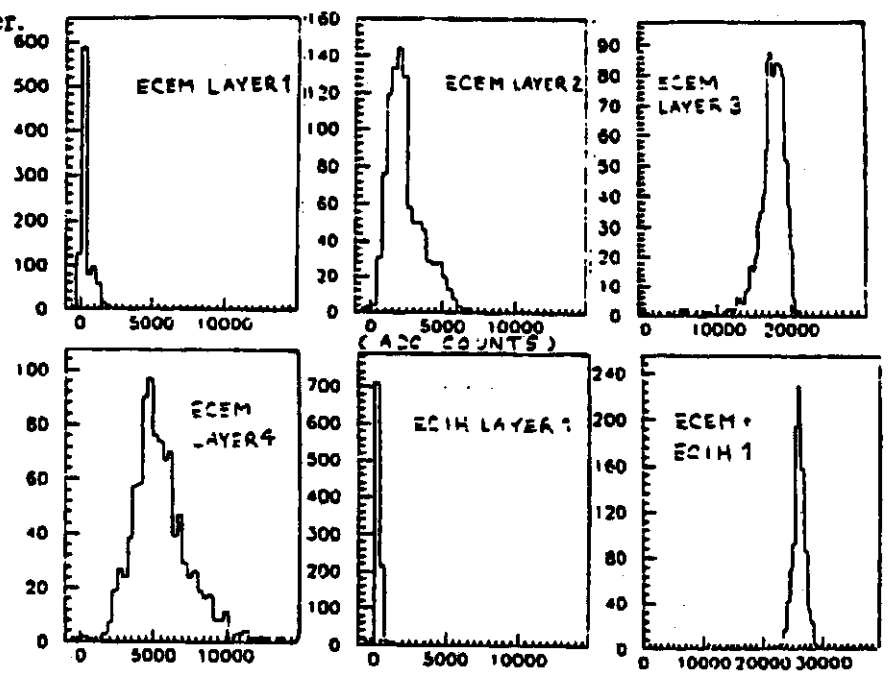

Figure 5.1 Distribution of energy in ECEM layers 1-4 and ECIH layer 1 and the total energy in the ECEM and ECIH layer 1 combined for 100 GeV electrons at $\eta = 2.3$ and $\phi = 3.0$ rad.

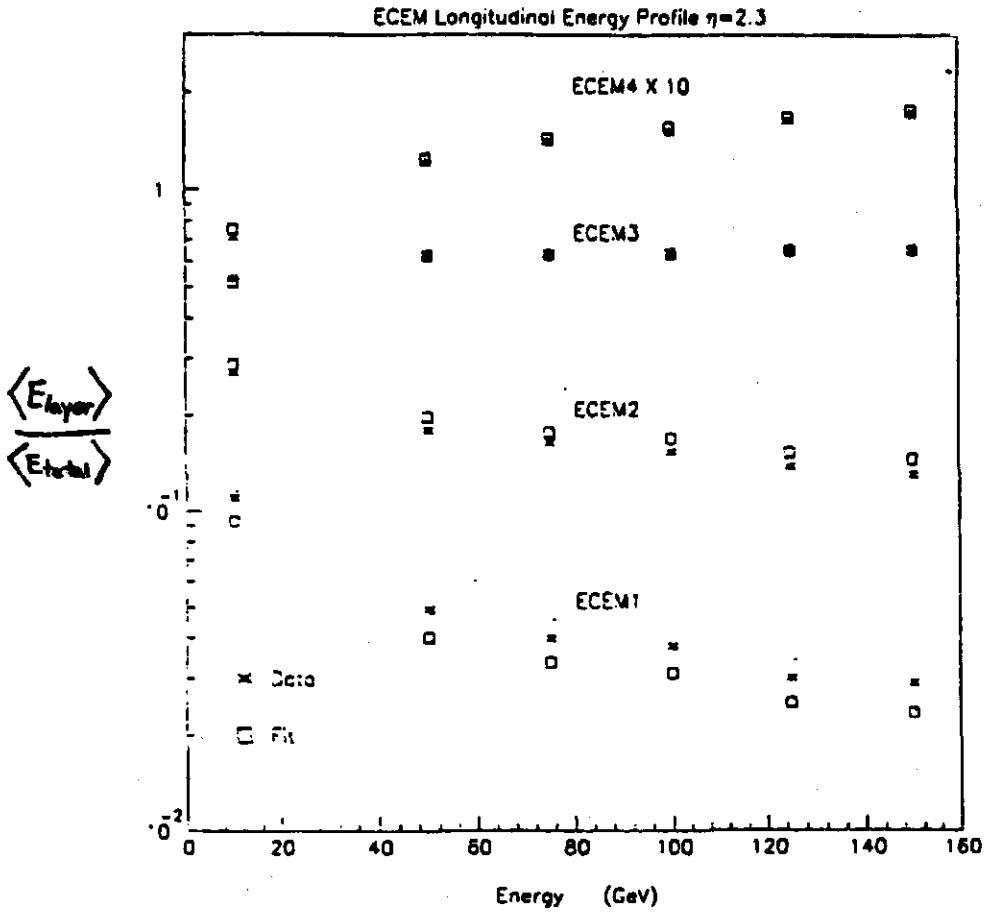

Figure 5.2 $\langle E_{layer}\rangle/\langle E_{total}\rangle$ plotted as a function of energy for ECEM layers 1-4 at $\eta = 2.3$. The asterisks are data and the open squares are from a fit to the data that is described in the text.

For a fixed energy, our data can be described by the electromagnetic longitudinal parametrization given in Eq. (3.2):

$$\frac{dE}{dz} = Az^{\alpha}e^{-bz} \tag{5.1}$$

where A is a normalization constant and α and b are the parameters to be determined in a fit to the data, and z is the longitudinal depth of material

in radiation lengths. The parameters are calculated by integrating Eq. (5.1) over the depths of the four individual calorimetric layers simultaneously. The dependence of the parameters α and b on energy was determined by fits to the values of α and b at each individual energy. These parameters show a logarithmic dependence of the form:

$$\alpha = \alpha_0 + \alpha_1 \ln E \tag{5.2}$$

$$b = b_0 + b_1 \ln E \tag{5.3}$$

The results we found were: $\alpha_0 = 0.91 \pm 1.2, \alpha_1 = 0.449 \pm 0.27, b_0 = -0.382 \pm 0.15 X_0^{-1}$ and $b_1 = -0.0049 \pm .034 X_0^{-1}$. This logarithmic dependence is a consequence of the logarithmic increase of the longitudinal extent of the showers with energy, as discussed in Section 3.2.

The ratios calculated from the fits to Eq. (5.1) are plotted as a function of energy in Fig. 5.2. The results for all the layers are found to be particularly sensitive to the depth t_1, that is taken as the start of the first ECEM layer. There is 2.73 X_0 of material upstream of the first layer (at $\eta = 2.3$), and this layer, designed to be almost "massless", consists of only 0.3 X_0 in depth. A value of $t_1 \approx 1.8 X_0$ provides the best agreement with the data. This suggests that electron showers are initiated, typically, after about 1.8 X_0 of the upstream material (well before the beginning of the first active layer). The agreement is reasonably good except that the fit underestimates the amount of energy deposited in layer 1. This can be understood from the fact that there is very little energy deposited in this layer so it is weighted less in the calculation.

The longitudinal shower shape in the data agrees well with that obtained seen in a Monte Carlo simulation. Figure 5.3 shows the mean energy deposited per radiation length of material, as a function of depth (taking account of the upstream material), for 50 GeV electrons at $\eta = 1.95$ and $\phi = 3.0$ rad. Both experimental data and the Monte Carlo results are shown plotted at the effective mean position of each ECEM layer.

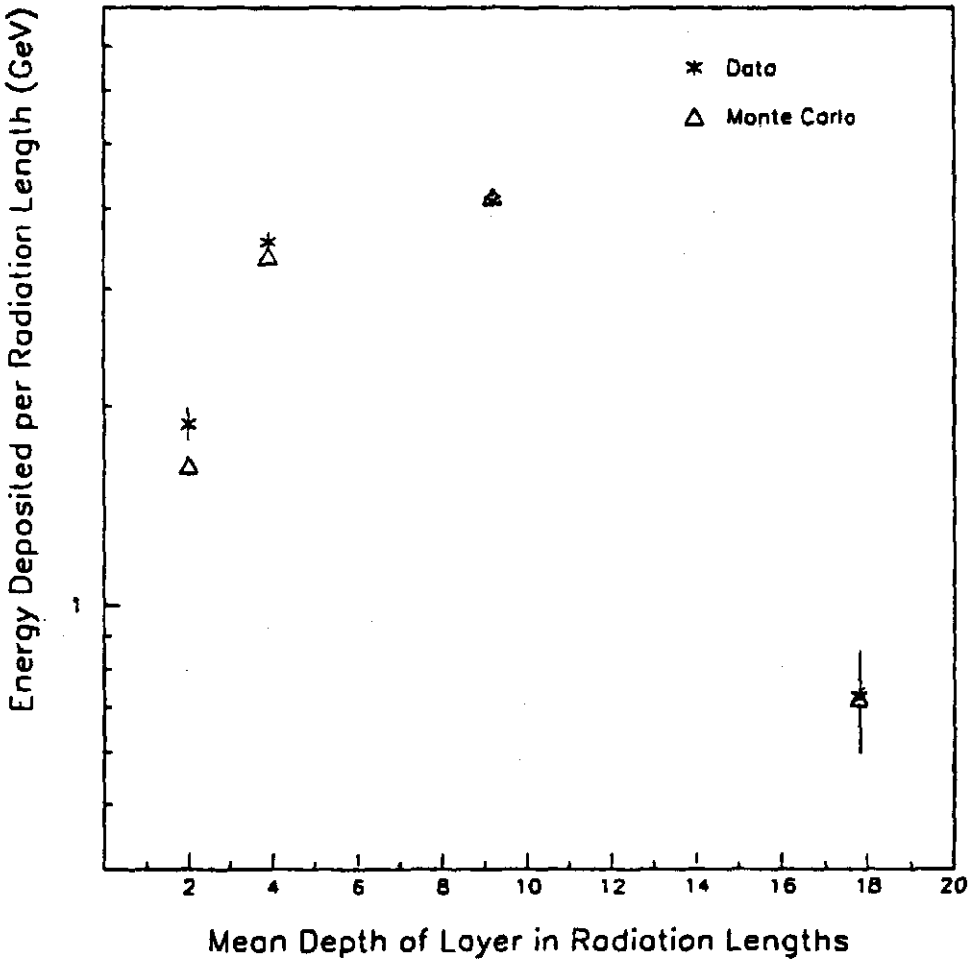

Figure 5.3 The longitudinal shower shape for 50 GeV electrons at $\eta = 1.95$ as a function of depth in the calorimeter. The asterisks are data and the open triangles are the results of a Monte Carlo simulation.

5.1.2 Transverse Shape of Electromagnetic Showers

The transverse shape of electromagnetic showers was determined by examining the fraction of total energy deposited in ECEM layer 3 in all towers a distance $\geq x$ away from the impact position of the shower averaged over a large number of events. The tower structure of the ECEM has been used to integrate over towers at a given ϕ. The distance $x = r \cdot \phi$ where ϕ is the azimuthal coordinate in radians and r is the radial distance from the beam pipe in cm, forming a polar coordinate system. (See Figure 5.4) The experimental data used had a zero-suppression level of ± 3 standard deviations from the pedestal value. This was done so that the data could be compared with a detailed Monte Carlo simulation (See Appendix A) that did not include the effects of electronic noise or uranium radioactivity-induced noise. The resulting transverse profile is shown in Fig 5.5. The data and the Monte Carlo agree quite well, although the transverse shape in the Monte Carlo seems to be somewhat narrower than that of the data.

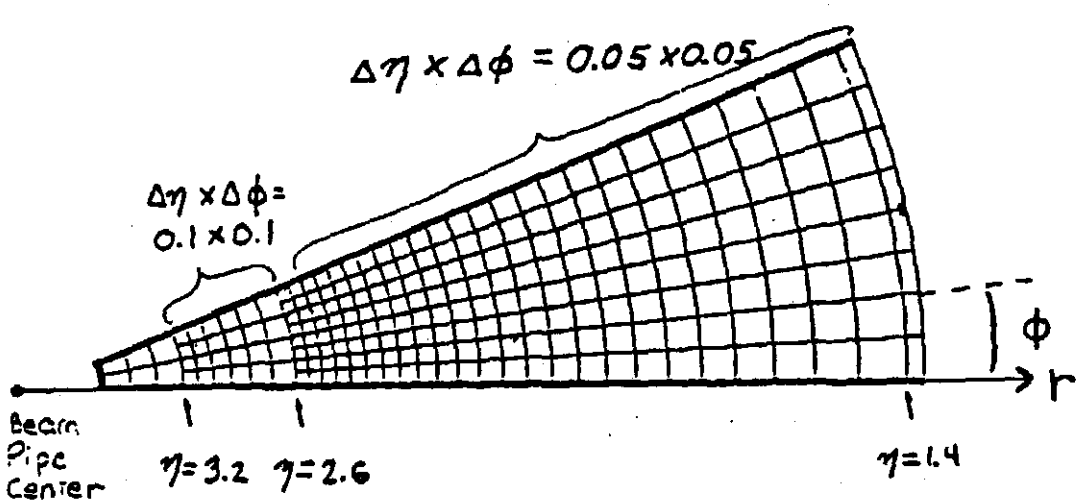

Figure 5.4 The pad layout of a 22.5° multilayer signal board in ECEM layer 3 showing r-ϕ segmentation.

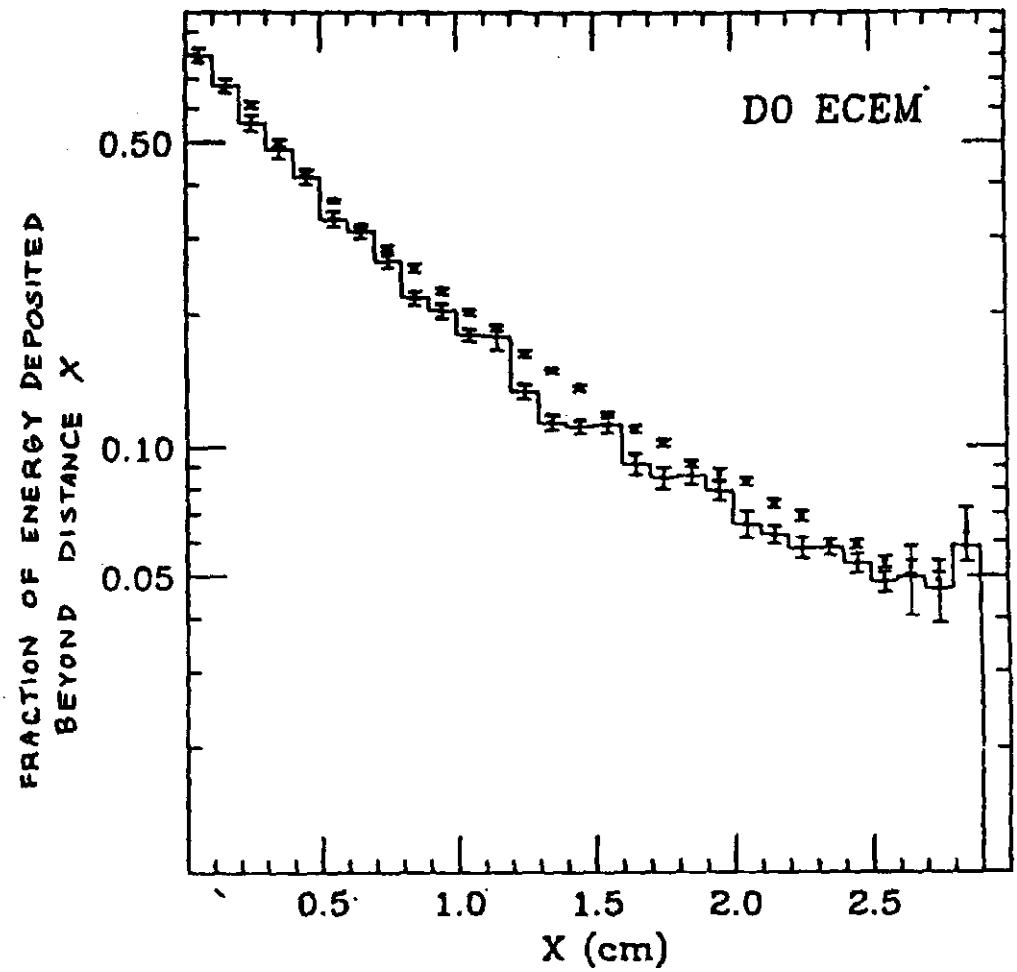

Figure 5.5 Transverse profile for 50 GeV electron showers in ECEM layer 3. The points are data and the histogram represents a Monte Carlo simulation [44].

The transverse projection (i.e. the energy deposited along one direction, x) of an electromagnetic shower in ECEM layer 3 has been characterized by the sum of two exponentials

$$\frac{dE}{dx} = A_1 e^{\frac{-|x-x_0|}{B_1}} + A_2 e^{\frac{-|x-x_0|}{B_2}} \tag{5.4}$$

where x is either the radial (r) or azimuthal ($r \cdot \phi$) coordinate, and x_0 is the

impact position of the shower. Both of these coordinates were evaluated at the longitudinal center of ECEM layer 3. The first exponential term describes the core of the shower, and the second term describes the halo of the shower. A fit of 50 GeV electron showers at $\eta = 1.95$ in ECEM layer 3 to Eq. 5.4 gives $A_1/A_2 = 3.7 \pm 0.1$, $B_1 = 2.9 \pm 0.1$ mm, and $B_2 = 11.1 \pm 0.1$ mm [44]. These parameters vary with the energy and with the angle of incidence of the particle.

5.1.3 Methods for Determining Transverse Electromagnetic Position

As discussed in Chapter 3, the impact position of an electron in a calorimeter can usually be determined to much better accuracy than just the size of the cell used in the segmentation. The most straightforward algorithm for reconstructing the central position of a shower from a set of lateral energy measurements is through the calculation of the energy centroid of the shower (the center-of-gravity method):

$$\bar{x} = \frac{\sum_i E_i x_i}{\sum_i E_i} \tag{5.5}$$

where $\bar{x}$ is a first-order estimate of the coordinate x_0, the center of the shower, E_i is the energy deposited in tower i, and x_i is the central position of the tower.

For a complex transverse shower shape, as we have for electrons, $\bar{x}$ depends on x_0 in a nonlinear way. Figure 5.6 shows $x_0 - \bar{x}$ plotted as a function of x_0, for the $r \cdot \phi$ coordinate, for electron data at 100 GeV, at $\eta = 2.25$ and $\phi = 3.0$ rad. The well known "S-curve" shape of Fig 5.6 is a result of the fact that the linear assumption in Eq. 5.5 leads to too small a weighting of the towers with small energy depositions [66]. That is, the shape of the shower is

not considered in Eq. (5.5). For a shower that can be described approximately by a single exponential with a transverse spread characterized by S:

$$E(x) = E_0 e^{-|x-x_0|/S} \tag{5.6}$$

the relationship between x_0 and $\bar{x}$ can be shown to be [29]:

$$x_0 - x_{max} = S \cdot sinh^{-1}\left(\frac{(\bar{x} - x_{max})}{\Delta} \cdot sinh\frac{\Delta}{S}\right), \quad for \quad -\Delta \leq x_0 - x_{max} \leq \Delta \tag{5.7}$$

where x_{max} is the position of the center of the tower that contains the largest energy signal and Δ is the half-width of a pad. It is clear that $x_0 = \bar{x}$ when $x_0 = 0$ and when $x_0 = \Delta$. This result can be seen in the data of Fig 5.6.

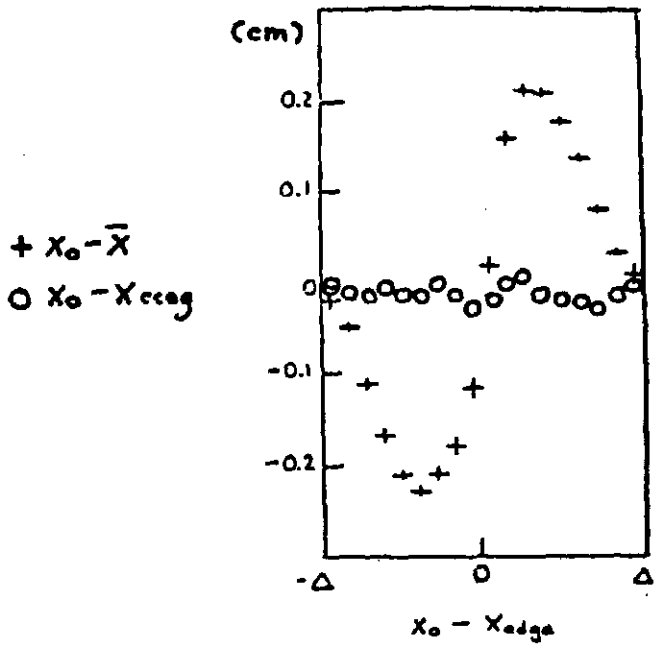

Figure 5.6 The difference between the impact position x_0 and the estimated position $\bar{x}$, $x_0 - \bar{x}$, and the difference between x_0 and the corrected position x_{ccog}, $x_0 - x_{ccog}$, plotted as a function of $x_0 - x_{edge}$, where x_{edge} is the pad edge closest to x_0.

For a shower profile that is described better by a double exponential fall-off, as is case for electron showers, the analysis is more complicated. It is not possible to find a solution in closed form comparable to Eq. (5.7). However, the bias in $\bar{x}$ for a double-exponential shape has been numerically calculated using the shower shape fit parameters given above for data at $\eta = 1.95$ [67]. The difference between the double exponential result and that for a single exponential fit, using $S = 5$mm as an estimate, was less than 0.2 mm for all values of impact point $-\Delta \leq x_0 - x_{max} \leq \Delta$.

Two algorithms were tried for extracting the central position of electromagnetic showers. Only ECEM layer 3, which has the finest segmentation of all the layers, was used in these studies. The first method, known as the corrected-center-of-gravity method, follows from Eq. (5.7). Namely,

$$x_{ccog} = x_{max} + S \cdot sinh^{-1}\{\frac{(\bar{x} - x_{max})}{\Delta} \cdot sinh(\frac{\Delta}{S})\} \tag{5.8}$$

where $\bar{x}$ is the simple result of a center of gravity calculation using Eq. (5.5). As can be seen in Eq. (5.7), the size of the deviation of $\bar{x}$ from x_0 depends on the ratio of the tower size relative to the shower width Δ/S. Using a weighted average of B_1 and B_2 (weighted by A_1 and A_2) from the fit in Eq. (5.4) given above, at $\eta = 1.95$, this ratio for ECEM layer 3 is $\Delta/S \approx 2.8$. This value of the ratio is within the range where the corrected-center-of-gravity method has been found to give good results [29]. The difference between the impact position x_0 and the corrected-center-of-gravity position x_{ccog} is plotted for 100 GeV electrons in Fig. 5.6. The "S-Curve" shape has been almost entirely eliminated. The value of S used in the correction is 4.1 mm.

The second algorithm, called the double-exponential method, is based on

the observed transverse shower profile [68]. In this technique, all the energy to the "right" of the tower containing the maximum energy (in either η or ϕ) is summed, and denoted as E_R. The ratio of E_R to the total energy deposited in layer 3, E_T, is then given by:

$$\frac{E_R}{E_T} = \frac{\int_0^\infty (dE/dx)dx}{\int_{-\infty}^\infty (dE/dx)dx} = \frac{A_1 B_2 e^{\frac{-|x_0|}{B_1}} + A_2 B_1 e^{\frac{-|x_0|}{B_2}}}{2(A_1 B_2 + A_2 B_1)} \quad where \quad x_0 < 0 \quad (5.9)$$

where $x = 0$ is defined to be the right edge of the tower with the highest energy and x_0 is to the "left" of x=0. With parameters A_1,B_1,A_2,B_2 determined from fits to the transverse shape, one can extract $|x_0|$ from the ratio of E_R/E_T through an iterative procedure.

5.1.4 Results for Electromagnetic Position Resolution

Trajectories of electrons were determined using the PWCs located upstream in the beamline. These trajectories were then extrapolated to the middle of ECEM layer 3. This extrapolated position was known to a precision of $\approx$ 400 μm, which is significantly better than the position resolution of the ECEM. The overall offset between the PWCs and the ECEM had an uncertainty of several mm, and consequently the absolute position was referenced to the ECEM coordinates by the addition of an offset to the PWC values. This offset was determined from a fit to the data. A Gaussian fit to the difference between the measured impact positions in ECEM layer 3 and the values extrapolated from the trajectories was used to determine the position resolution of the calorimeter, as shown in Fig. 5.7. The standard deviation of this Gaussian fit measures both the resolution at each point across a tower and the magnitude of the systematic deviation (S-curve shape) of the

reconstructed positions, and therefore provides a good estimate of the overall position resolution.

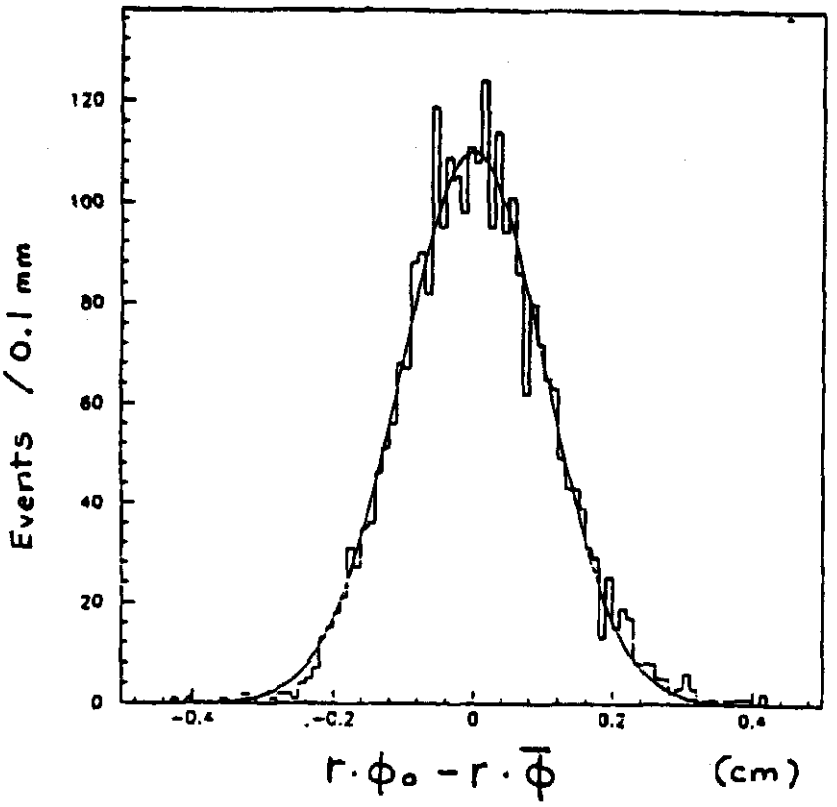

Figure 5.7 The corrected position resolution for 75 GeV electrons entering the ECEM at a pseudorapidity of $\eta = 1.95$. The Gaussian fit has a mean of $\mu = -.009 \pm 0.014$ mm and a standard deviation 1.03 ± 0.01 mm.

Both of the methods investigated for determining shower centers, give very similar results for 50 GeV electrons at $\eta = 1.95$ [44]. In the following analyses, the data are for $\phi = 3.0$ rad namely 8.4° above the -x axis, unless stated to the contrary.) Because the corrected-center-of-gravity method does not require extensive fitting to shower shapes at different energies and angles, and is not as sensitive to fluctuations in the shower, this was the method that was investigated further. Only the resolution in the azimuthal direction,

namely $x = r \cdot \phi$ is examined in what follows. The resolution for the radial direction $x = r$ is similar [44].

These further investigations involve finding parameters that optimize the calculation of the impact position. The optimum parameters at each energy and angle of incidence can then be used in the collider experiment to determine the positions of incident electrons. There are two parameters that can be varied to optimize the position resolution in the corrected-center-of-gravity method. These are the width of the shower in ECEM layer 3 (the parameter S) and a threshold cut (a parameter τ) that determines which towers are to be included in the center-of-gravity sum. Only towers with energy greater than this cut are included in the sums. The initial values chosen for these parameters, $S = 5.0$mm and $\tau = 15$ ADC cnts (1 GeV $\approx$ 260 ADC cnts), give good results for energies ranging from 10 to 150 GeV, as can be seen in Fig 5.8. The statistical errors are typically smaller than the data points.

The first optimization involved finding parameters that gave the best resolution at 75 GeV and applying these to the other energies. The resolution was minimized with respect to S at $\tau = 15$ cnts, and then with respect to τ. These minimizations were done by fitting curves of resolution versus S or τ to polynomials using the MINUIT fitting package and then finding the minimums of these curves [69]. The optimized parameters were found to be $S = 5.2$mm and $\tau = 94$ ADC cnts. The large value of τ indicates that the tails of the electromagnetic shower are not important in the position calculation. The position resolution varied from 0.953-0.980 mm with S values in the range 4.7-6.0 mm and from 0.942-1.006 mm for τ values in the range 0-190 ADC

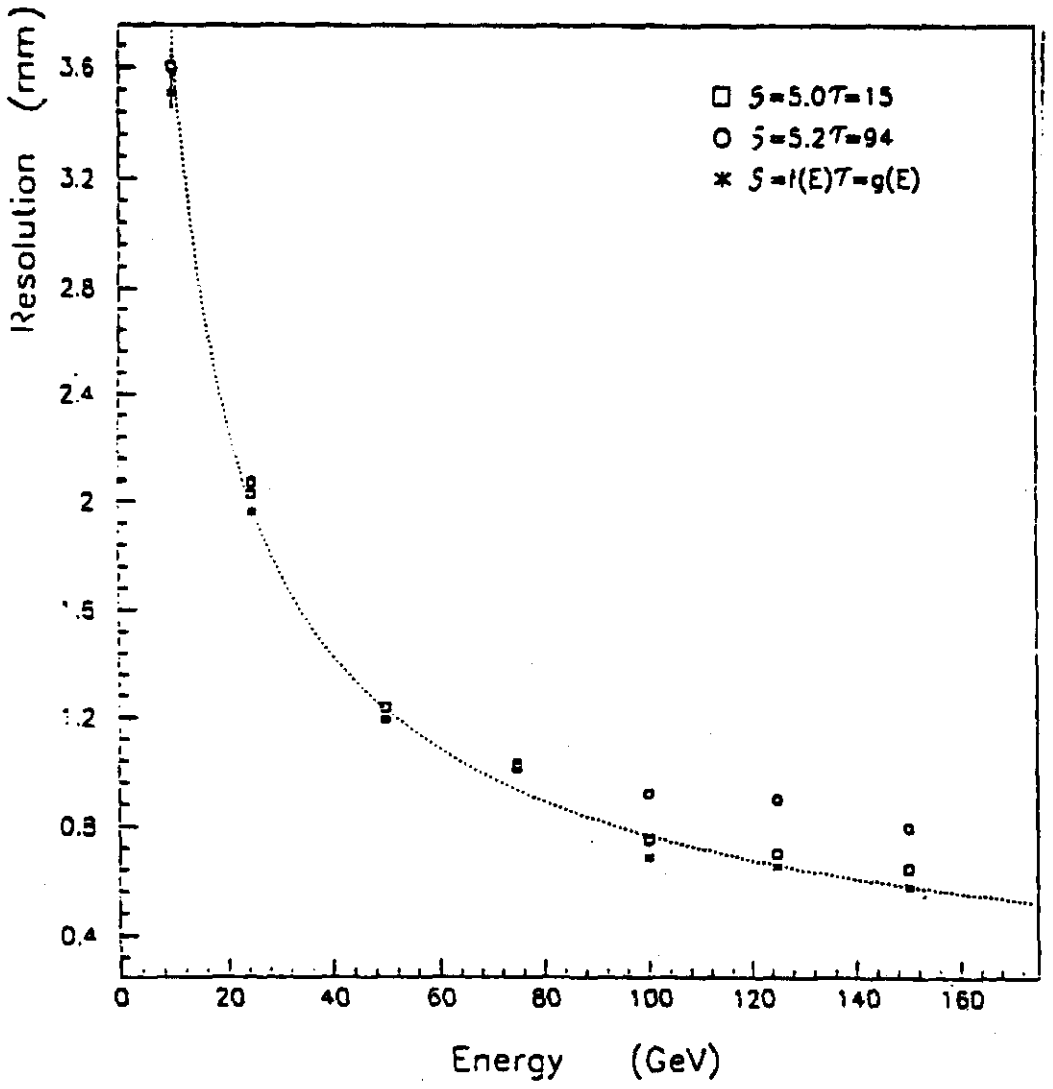

Figure 5.8 The electromagnetic position resolution plotted as a function of energy for the corrected-center-of gravity method with the three sets of parameters given in the legend. The dotted line is a fit to the resolution obtained using the optimized parameter set (asterisks) for the phenomenological form $\sigma(r \cdot \phi) = (17.9 \pm 0.4)E^{-0.685 \pm 0.005}$ mm.

cnts. The optimized parameters were found to give resolutions comparable to or better (by .01-.06 mm) than those found using the starting parameters for energies $\leq$ 75 GeV (except at 10 GeV where the threshold cut sometimes left towers with only one ϕ value in the sum) but worse resolutions for energies > 75 GeV (See Fig 5.8).

In the second optimization scheme, τ and S were determined as functions of energy. An initial try of $\tau = 1.25 \times E$ cts was used for the threshold, where E is the electron energy in GeV, and the value of S was optimized at each energy. Then the best value of τ at each energy was determined using the optimized values of S. The functions, plotted in Fig. 5.9, are:

$$\tau = g(E) = -6 \pm 18. + (1.66 \pm 0.20) \cdot E \text{ cnts}, \quad E \geq 10 \text{ GeV} \qquad (5.10)$$

$$S = f(E) = 6.83 \pm 0.08 - (0.494 \pm .017) \cdot \log(E) \text{ mm} \quad E \geq 10 \text{ GeV} \quad (5.11).$$

The threshold cut depends linearly on energy, indicating that the cut yields a constant fraction of the energy of the total shower. The shower width parameter S decreases logarithmically with energy. This may be explained by the logarithmic increase in depth of the shower maximum with energy such that ECEM layer 3 measures the narrower, early portion of a shower at higher energies. The position resolution using such fits is at least as good as that found using the two simpler parametrizations of Fig. 5.8. The ability to determine precise positions using the thresholds given by Eq. (5.10), which corresponds roughly to summing $\approx 10 - 12$ towers at all energies, indicates that the energy deposition much beyond the center of a shower can be ignored. Namely, it is not necessary to include the entire extent of the shower in the calculation of position. This is useful in a collider environment where it is

likely for particle showers to overlap in high multiplicity events. Due to the statistical nature of shower development, we expect the resolution to vary as $1/\sqrt{E}$. A fit to the energy dependence of the data is given in the caption below Fig. 5.8.

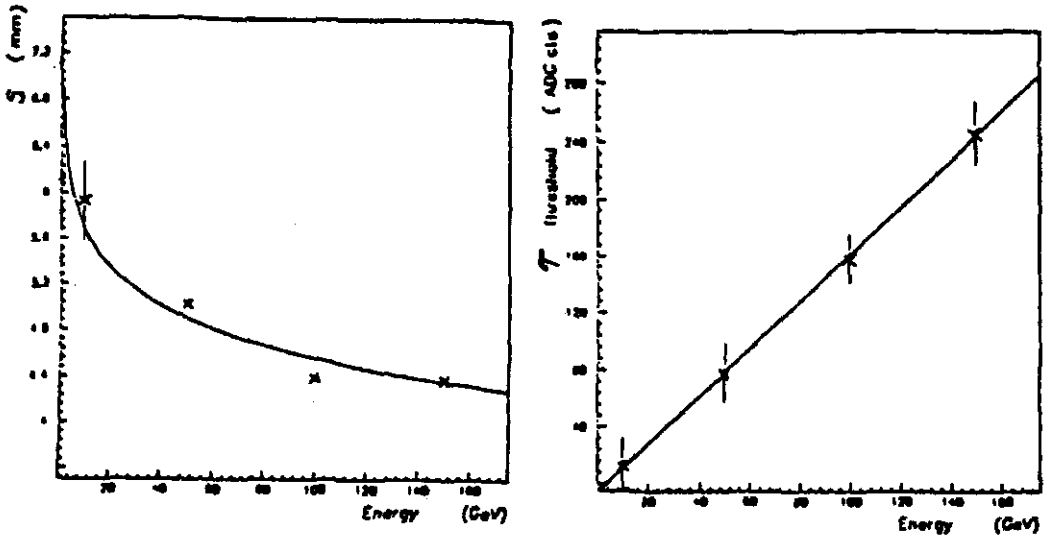

Figure 5.9 Optimized values of corrected-center-of-gravity parameters S and threshold cut, τ, plotted as functions of energy. The fits are those given in Eqs. (5.10) and (5.11).

An identical analysis was performed to optimize the position resolution for 100 GeV electrons at different pseudorapidities. Optimized threshold cut parameter and S values were determined for five pseudorapidities in the range η= 1.65 - 2.85. These parameters are plotted as a function of pseudorapidity in Fig. 5.10. The threshold cut generally decreases with increasing η, which

is to be expected because the pad size changes as $\Delta r = r\Delta\eta/\cos\theta$. (The value of the threshold cut at $\eta = 2.85$ has been divided by four to take into account the increase in pad size seen in Fig. 5.4 and described below.) The slight decrease in r at $\eta = 1.65$ may be due to edge effects. In a Monte Carlo study, it was found that at $\eta = 1.65$, 99.5% energy containment is achieved by summing an array of 4×4, 0.1×0.1 size, towers, consequently there is some energy deposition in the edge towers at $\eta = 1.45$ for this pseudorapidity [44]. The effect of these threshold cuts was to include only 10-15 towers at all η's in the energy sums used to calculate position.

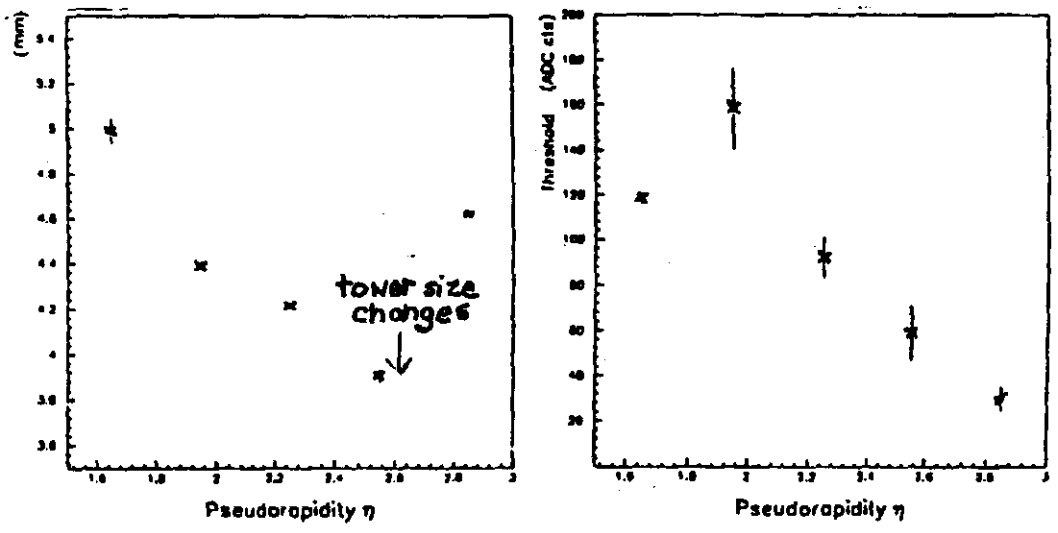

Figure 5.10 Optimized values of corrected-center-of-gravity parameters plotted as a function of pseudorapidity η. The arrow indicates where the calorimeter tower size changes from $\Delta\eta \times \Delta\phi = 0.05 \times 0.05$ to 0.1×0.1.

The S parameter also decreases with increasing η except for $\eta > 2.6$, where the readout pad size increases to $\Delta R \times \Delta\phi = 0.1 \times 0.1$. The pad structure of ECEM layer 3 is shown in Fig. 5.4. Pad sizes are expected to

affect the η dependence of S. At a larger angle of incidence (smaller η), the particle traverses a greater number of X_0 before entering ECEM layer 3 and therefore the shower is also wider for smaller η.

The improvement of the spatial resolution with these optimized parameters can be seen in Fig 5.11 where the position resolution is plotted as a function of pseudorapidity. The statistical errors are the size of the data points.

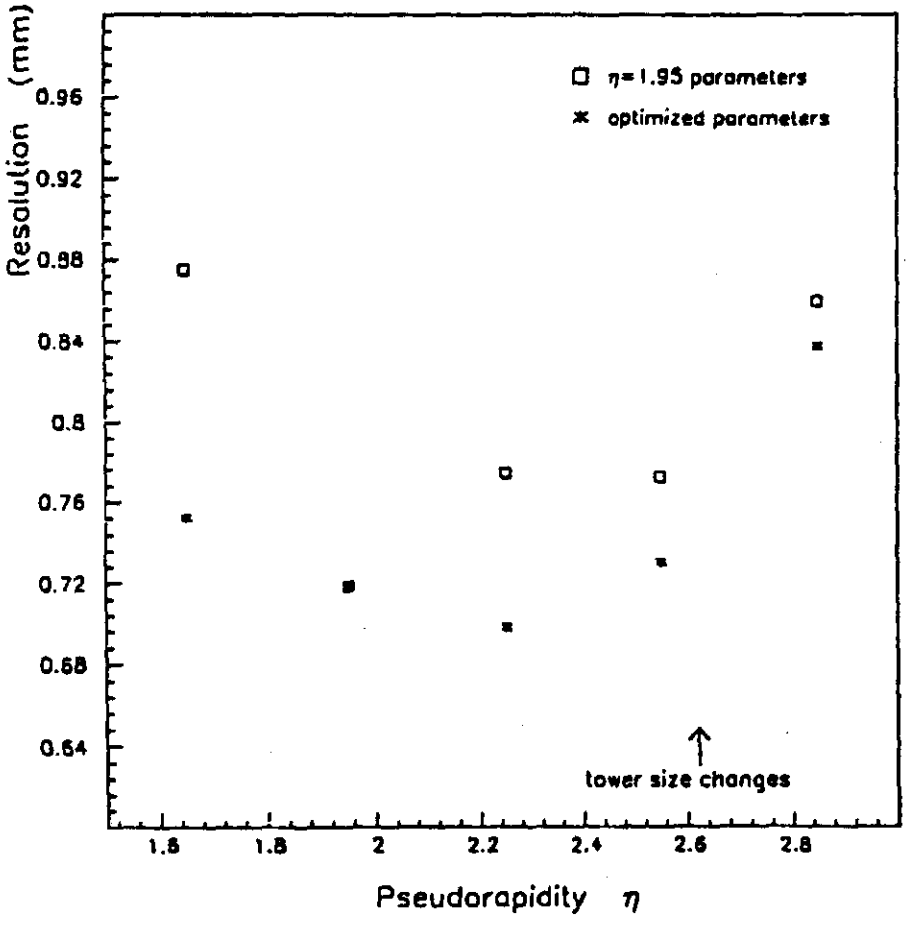

Figure 5.11 The position resolution for electromagnetic showers is plotted as a function of pseudorapidity for the corrected-center-of-gravity method using two sets of parameters. One from the values obtained at $\eta = 1.95$ and the other optimized at each energy.

The position resolution using only ECEM layers 2 and 4 individually was also examined at $\eta = 1.95$ for 100 GeV electrons. The results and the values of the optimized parameters are listed in Table 5.1. The resolution is about 4-5 times worse in these layers, which is due primarily to the larger pad sizes and smaller energy deposited. In the collider setting, the transverse position found in each of these layers could conceivably be used to determine the z position of the origin of an electron track. The uncertainty in this measurement would be about 12 cm which is not very precise so this method will not be used.

Table 5.1

Electromagnetic Position Resolution at $\eta = 1.95$

Layer	Threshold Cut (ADC cts)	S (mm)	Resolution (mm)
ECEM 2	80	7.0	3.376 ± 0.012
ECEM 3	158	4.4	0.718 ± 0.002
ECEM 4	160	15.5	2.321 ± 0.007

5.1.5 Conclusions

In conclusion, the longitudinal electromagnetic shower shape is well fit by Eq. (3.2) and agrees with that seen in the Monte Carlo. The transverse electromagnetic profile is well fit by the sum of two decaying exponentials. Both of the methods investigated for reconstructing the position of the shower centroid gave good results for 50 GeV electrons. The corrected-center-of-gravity method for position determination (Eq. (5.8)) was found to give good

results for electrons at various energies and angles of incidence. Optimized values of shower width and threshold cut parameters were found to improve the spatial resolution. Relatively large optimized threshold cuts τ indicate that the tails of transverse shower distributions can be ignored in calculating the shower centroid. The expected energy and pseudorapidity dependence of the position resolution was observed.

5.2 Analysis of the Shape of Hadronic Showers

The pion data sample underwent several processing steps similar to those used for electrons. The data were corrected for gain variations and for pedestal fluctuations in the same manner as the electron data. Because hadronic showers extend over larger areas of the calorimeters and are therefore more sensitive to noise, channels that had signals within two standard deviations of their pedestal values ("two-sigma zero suppression") were dropped. This reduced the number of channels that had to be read out. Subsequently, these data and the PWC information for beam tracks were written to standard test-beam Data Summary Tapes (DSTs).

All the layers in the ECEM and ECIH were summed to determine the total energy of a hadronic shower. In the following analysis of the shower shape, all 0.1×0.1 towers in a 10×10 array centered about the beam position were included in the energy sums. To account for the spread in the beam momentum from event to event, the momentum measured by the PWCs was used to correct the deposited energy. Any events with more than one track in the PWCs or with a track that did not point to the instrumented region of the calorimeter were cut out. Events where the halo or muon counters registered

a hit were also removed. Another restriction eliminated those events where the base-peak timing difference in the BLSs was outside of preset bounds. To select pions that started showers after entering the calorimeter modules, only events with less than 100 ADC cnts in ECEM layer 1 were retained for further study. Typically, 80% of all triggers in a run passed all these criteria.

5.2.1 Longitudinal Shape of Hadronic Showers

The energy deposited in five longitudinal layers of the calorimeter and the total energy deposited in the ECEM and ECIH combined for a 150 GeV pion run at $\eta = 2.55$ and $\phi = 3.0$ rad is shown in Fig. 5.12. The longitudinal shapes of hadronic showers, characterized by the mean energy deposited in each layer of the calorimeter divided by the number of absorption lengths (dE/dz_a), are shown in Fig. 5.13 for four pion energies. As can be seen from the figure, these profiles are well reproduced by a "plate-level" Monte Carlo simulation (See Appendix A). The longitudinal development for pion data at 50, 75, 100 and 150 GeV/c was fitted to the parametrization of Bock et al. given in Eq (3.6) [70,71]:

$$\delta E = \frac{E_0}{\Gamma(a)} w (bz_r)^{a-1} e^{-bz_r} b\delta z_r + \frac{E_0}{\Gamma(c)}(1-w)(dz_a)^{c-1} e^{-dz_a} d\delta z_a \qquad (3.6)$$

The fit parameters were: $a = c = 0.32 \pm 0.02 + (0.36 \pm 0.02) \cdot \ln(E)$ (fixed to be the same), $b = 0.20 \pm 0.02\ X_0^{-1}$, $d = 1.03 \pm 0.02\ \lambda_{abs}^{-1}$, and $w = 0.43 \pm 0.01$. This parametrization gives a good fit to the longitudinal distributions as can be seen in Fig 5.13.

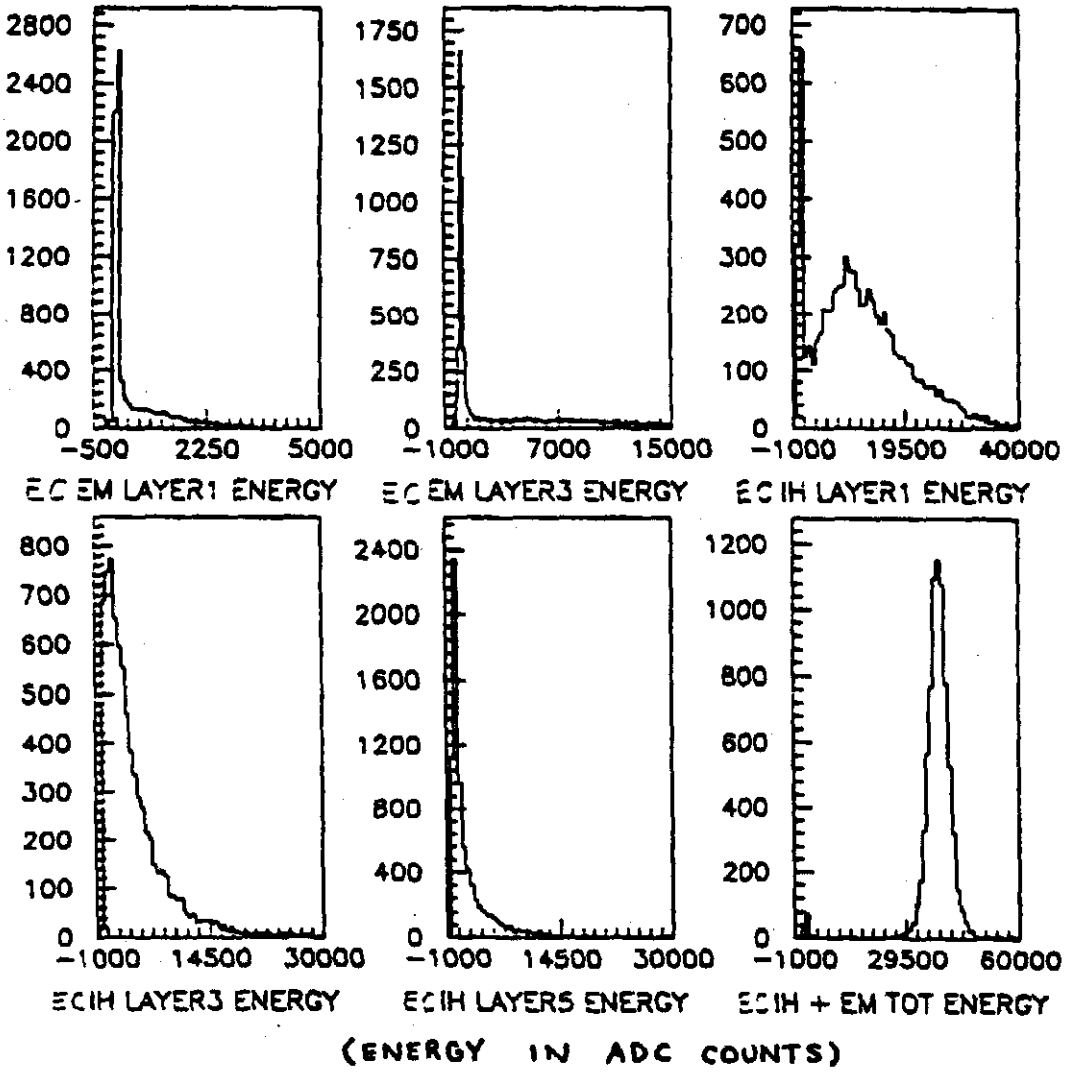

Figure 5.12 The energy distributions in five longitudinal layers of the calorimeter and the total energy deposited in the ECEM and ECIH combined for a 150 GeV pion run at $\eta = 2.55$ and $\phi = 3.0$ rad.

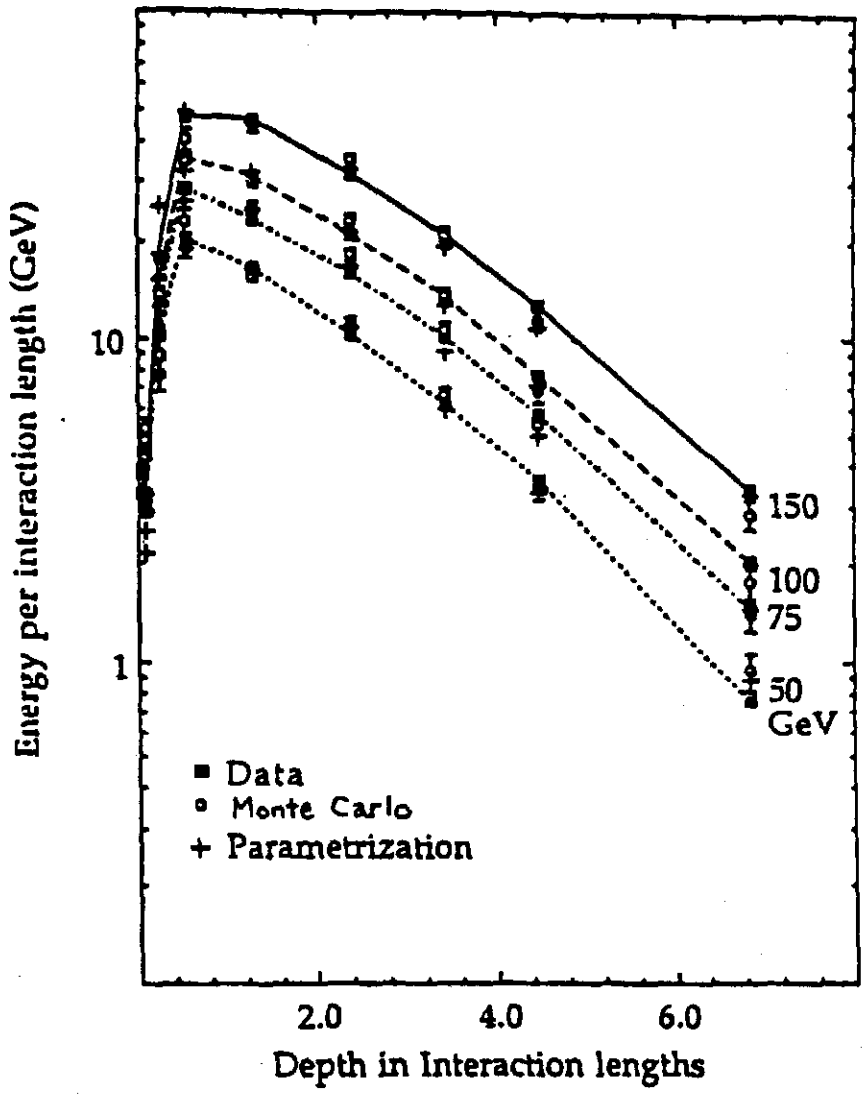

Figure 5.13 Longitudinal development of pion showers at four energies. The results from the data and Monte Carlo simulation are compared with the parametrization of Eq. (3.6) [52].

5.2.2 *Transverse Shape of Hadronic Showers*

Figures 5.14 and 5.15 display the transverse shower profiles for 150 GeV pions in ECEM layers 1-4 and ECIH layers 1-5 at $\eta = 2.55$. The profile, defined as an average over many events of the total energy deposited in a layer at a given $r \cdot \phi_i$ value divided by the total energy deposited in that layer,

is plotted as a function of the absolute value of the distance between the impact position $r \cdot \phi_0$ of the beam track, in the PWCs, and the location of the energy deposition: $x = |x_i - x_0| = |r \cdot (\phi_i - \phi_0)|$. The profiles were determined from a run of 10,000 events. This figure clearly illustrates the widening of the shower with depth into the calorimeter. The profiles in r were found to be like the profiles in $r \cdot \phi$ except that they were asymmetric about the impact position r_0 due to the asymmetric pad structure along r that results from the cylindrical geometry.

Finding a parametrization that provides a good description of the transverse hadronic shower profile is important for several reasons. This parametrization can be used to characterize the shower shape and compare it with the transverse shape of electromagnetic showers. A fit to the transverse shape can also be used to determine the impact position of a shower. Several different parametrizations were investigated for fitting the shapes in Figs. 5.14 and 5.15. There were two parametrizations that gave comparable results for the $r \cdot \phi$ shapes. The first form involved a double exponential dependence on distance, similar to Eq. (5.4), convoluted with a step function of length C :

$$\begin{aligned}
\frac{1}{E}\frac{dE}{dx} &= 2(A_1B_1 + A_2B_2) - A_1B_1(e^{-\frac{|x-x_0|}{B_1}} + e^{-\frac{C-|x-x_0|}{B_1}}) \\
&\quad - A_2B_2(e^{-\frac{|x-x_0|}{B_2}} + e^{-\frac{C-|x-x_0|}{B_2}}) + D \qquad |x - x_0| < C \\
\frac{1}{E}\frac{dE}{dx} &= A_1B_1(e^{-\frac{|x-x_0|-C}{B_1}} - e^{-\frac{|x-x_0|}{B_1}}) \\
&\quad + A_2B_2(e^{-\frac{|x-x_0|-C}{B_2}} - e^{-\frac{|x-x_0|}{B_2}}) + D \qquad |x - x_0| \geq C \qquad (5.12)
\end{aligned}$$

where x is the azimuthal $(r \cdot \phi)$ coordinate, and x_0 is the impact position of the shower and D is an overall offset that accounts for the noise level in the calorimeter. (When The step function is used to take into account the finite

tower size that tends to broaden the distribution at the peak near $x=x_0$. This smearing occurs because the energy in a tower is assigned to a position at the center of that tower. This is equivalent to assuming a uniform energy distribution within the tower. As in the electromagnetic case, the first term models the core of the shower and the second term the halo. The fit parameters and χ^2s obtained are listed in Table 5.2. The broadening of the shower with depth is reflected in the increase of B_1 and B_2 with layer number. The increasing pad size with depth is taken into account in the increasing values of C. (In ECEM layer 3, four 0.05×0.05 towers were summed to create one 0.10×0.10 tower so that the data could be compared with those of the other layers.) The values of B_1 (6 - 24 mm) and B_2 (30-120 mm) are significantly larger than those found for the electromagnetic shower profile in ECEM layer 3 ($B_1 = 2.9$ mm, $B_2 = 11$ mm).

The second parametrization that was found to give a good fit to the shower shape was a sum of two modified Lorentzians and a constant term:

$$\frac{1}{E}\frac{dE}{dx} = \frac{A_1}{(|x - x_0| - B_1)^2 + C_1} + \frac{A_2}{(|x - x_0| - B_2)^2 \pm C_2} + D \qquad (5.13)$$

where the first term describes the core of the shower and the second term describes the tails. (Only one term was used for ECIH layer 5.) The results of the fit can be seen in Fig 5.16 where each term is plotted separately for several layers. The core term decreases in height and the tail term widens gradually with increasing depth. Table 5.3 lists the fit parameters and χ^2s obtained using this method. As can be seen from the χ^2s in Table 5.3, this fit models the transverse shape better than the previous parametrization.

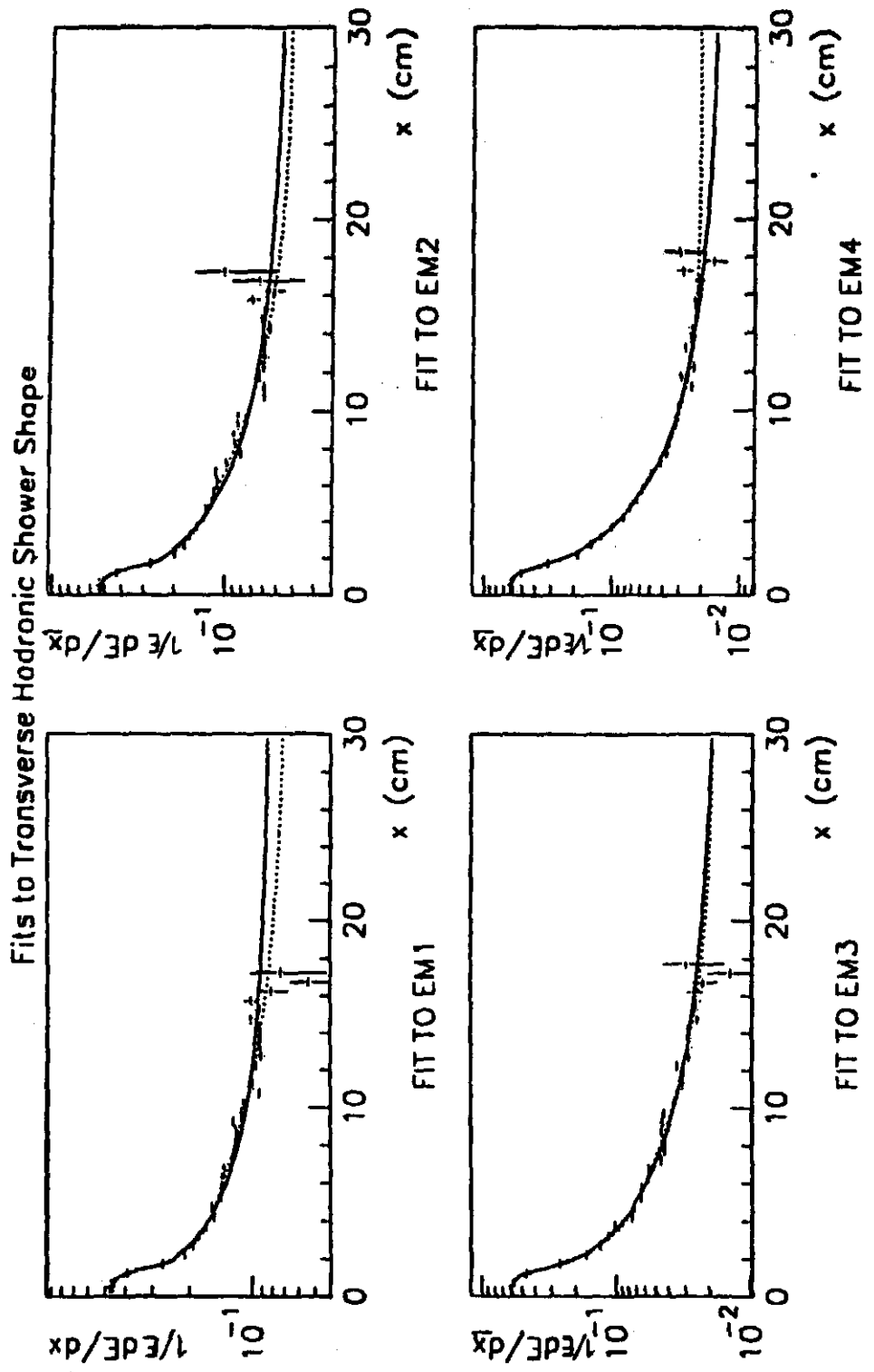

Figure 5.14 The transverse hadronic shower shape in ECEM layers 1-4, $x = |x_i - x_0|$. The dotted line is the convoluted double exponential fit and the solid line is the modified Lorentzian fit, both described in the text.

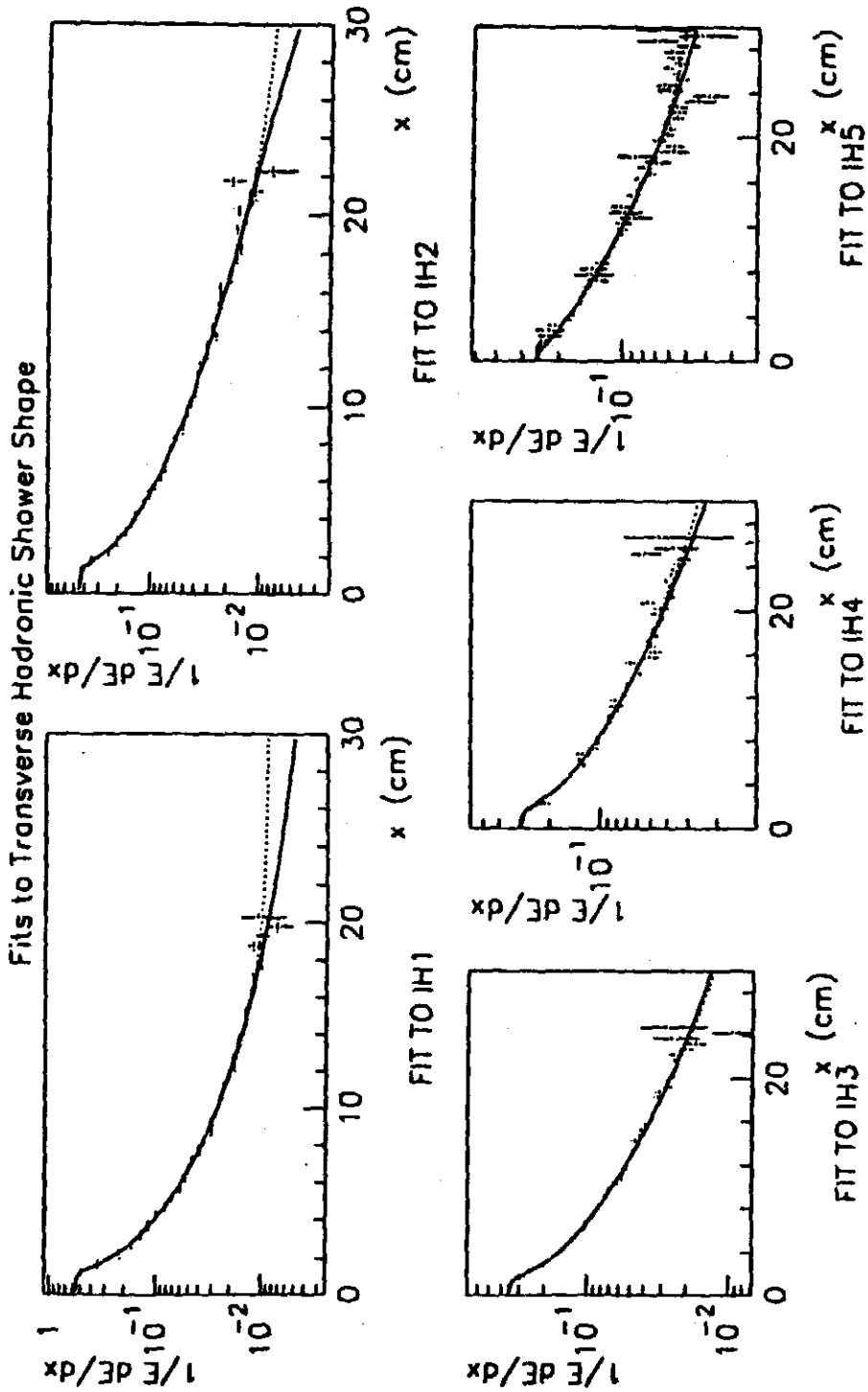

Figure 5.15 The transverse hadronic shower shape in ECIH layers 1-5, $x = |x_i - x_0|$. The dotted line is the convoluted double exponential fit and the solid line is the modified Lorentzian fit, both described in the text.

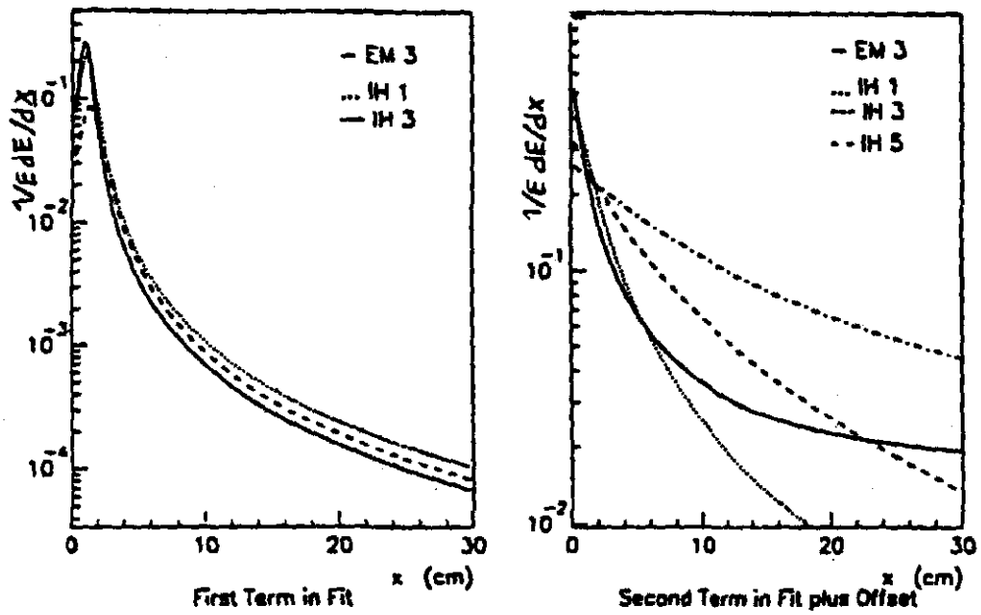

Figure 5.16 The first and second terms in the modified Lorentzian fit to the transverse shower shape plotted separately.

Profiles obtained from a plate-level Monte Carlo simulation were also fitted to the parametrization of Eq. (5.13). A comparison of fits to the Monte Carlo events and to data for four of the layers is shown in Fig. 5.17. In comparing the half-widths at half-maximum (HWHM's) from the figure, one sees that the Monte Carlo showers are narrower than the data in the early part of the shower, as seen in the electromagnetic case, but wider in the later part of the shower. This may indicate that the Monte Carlo showers have narrower electromagnetic cores and wider hadronic tails than those seen in the data.

Table 5.2

Parameters for Convoluted Double Exponential

Fit to Transverse Hadronic Shower Shape

EC Layer	A_1 (cm^{-2})	B_1 (cm)	A_2 (cm^{-2})	B_2 (cm)	C (cm)	D (cm^{-1})	χ^2
EM 1	0.354 ± 0.009	0.65 ± 0.07	0.121 ± 0.006	7.3 ± 1.4	1.183 ± 0.045	0.069 ± 0.008	3.82
EM 2	0.456 ± 0.009	0.564 ± 0.046	0.150 ± 0.006	5.6 ± 0.5	1.200 ± 0.031	0.0407 ± 0.0037	6.07
EM 3	0.630 ± 0.010	0.725 ± 0.037	0.102 ± 0.007	5.2 ± 0.6	1.130 ± 0.026	0.0189 ± 0.0023	6.69
EM 4	0.552 ± 0.008	0.627 ± 0.031	0.161 ± 0.009	2.97 ± 0.13	1.249 ± 0.017	0.0204 ± 0.0006	8.08
IH 1	0.433 ± 0.007	0.855 ± 0.037	0.148 ± 0.007	3.88 ± 0.14	1.293 ± 0.021	0.0089 ± 0.0004	6.69
IH 2	0.274 ± 0.009	1.25 ± 0.06	0.134 ± 0.006	6.17 ± 0.31	1.320 ± 0.038	0.0055 ± 0.0011	4.05
IH 3	0.188 ± 0.023	1.97 ± 0.23	0.123 ± 0.015	9.4 ± 1.9	1.27 ± 0.07	0.006 ± 0.006	1.51
IH 4	0.110 ± 0.022	2.36 ± 0.44	0.108 ± 0.014	11.8 ± 2.9	1.43 ± 0.16	0.013 ± 0.009	2.05
IH 5	0.022 ± 0.007	1.28 ± 0.89	0.133 ± 0.033	9.2 ± 0.7	1.46 ± 0.33	0.0422 ± 0.0031	1.22

Table 5.3

Parameters for Modified Lorentzian Fit to Transverse Hadronic Shower Shape

EC Layer	A_1 (cm)	B_1 (cm)	C_1 (cm^2)	A_2 (cm)	B_2 (cm)	C_2 ($\pm cm^2$)	D (cm^{-1})	χ^2
EM 1	0.0076 ± 0.0045	1.0042 ± 0.0058	0.012 ± 0.041	6.23 ± 0.30	-5.79 ± 0.06	-20.0 ± 3.3	0.0794 ± 0.0016	3.17
EM 2	0.0090 ± 0.0041	1.0003 ± 0.0043	0.008 ± 0.030	7.21 ± 0.24	-5.680 ± 0.040	-20.0 ± 1.8	0.0409 ± 0.0013	5.41
EM 3	0.0565 ± 0.0012	0.984 ± 0.007	0.1642 ± 0.0003	4.14 ± 0.10	-5.050 ± 0.009	-19.90 ± 0.11	0.0159 ± 0.0006	2.52
EM 4	0.087 ± 0.013	1.015 ± 0.010	0.280 ± 0.035	2.19 ± 0.24	-1.72 ± 0.43	0.5 ± 1.1	0.0130 ± 0.0008	3.05
IH 1	0.086 ± 0.012	1.100 ± 0.015	0.358 ± 0.042	3.43 ± 0.21	-1.90 ± 0.29	2.6 ± 0.7	0.0015 ± 0.0005	2.21
IH 2	0.082 ± 0.015	1.203 ± 0.033	0.52 ± 0.08	11.9 ± 1.5	-5.9 ± 1.0	-7. ± 9.	-0.0051 ± 0.0013	2.17
IH 3	0.067 ± 0.030	1.33 ± 0.09	0.78 ± 0.30	22. ± 6.	-8.2 ± 2.6	-3. ± 26.	-0.0017 ± 0.0035	0.94
IH 4	0.094 ± 0.040	1.54 ± 0.12	1.5 ± 0.6	123. ± 5.	-36.6 ± 0.5	-918. ± 36.	-0.0120 ± 0.0022	0.75
IH 5	-	-	-	73. ± 6.	-16.0 ± 1.0	30. ± 24.	0.0108 ± 0.0038	0.63

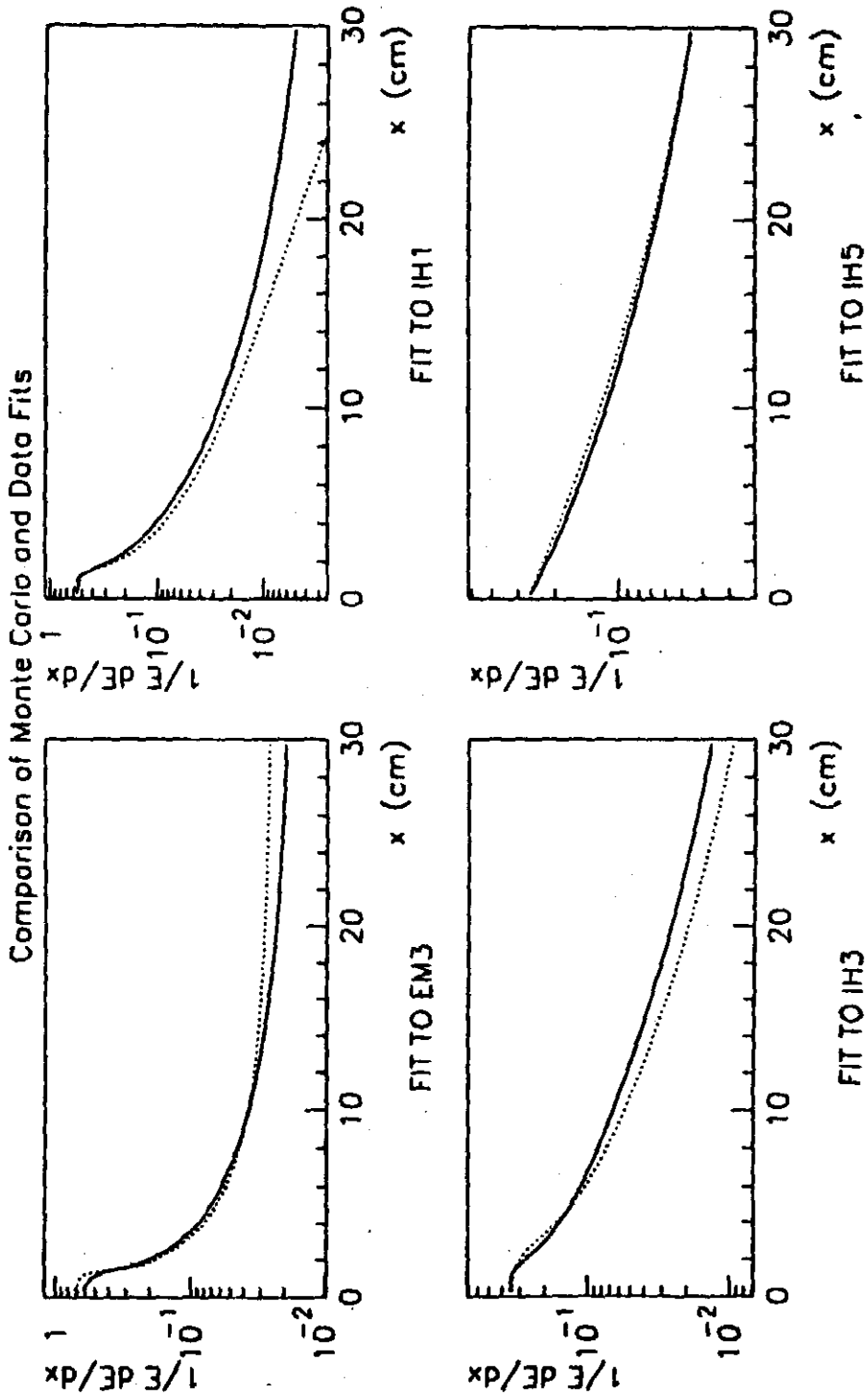

Figure 5.17 Modified Lorentzian fits to the transverse shower shape seen in the data (solid line) and the Monte Carlo (dotted line).

To examine the unsmeared transverse shower profile, the ratio E_R/E_T (the energy in a layer to the right of the edge of the tower with the most energy, divided by the total energy in the layer) was plotted as a function of impact position relative to the edge of a tower. This quantity is not sensitive to the energy distribution within a tower. The data and the corresponding fits are shown in Fig. 5.18 for several layers. The fits are of the same form as used for electromagnetic showers in Eq. (5.9). In Fig. 5.18, these results are compared with those obtained using the parameters from fits to Eq. (5.12) in the unconvoluted double exponential of Eq. (5.9). The good agreement of the fits for each layer implies that convolution with a step function is a good way to model the effect of the finite pad size.

5.2.3 Methods for Determining Transverse Hadronic Position

Several kinds of methods were examined for determining impact positions of hadronic showers. One set of methods involved a center-of-gravity type of calculation. The position along one dimension ($\bar{x}$) was defined using all the layers of the ECEM and ECIH modules, with each tower (i) in each layer (j) in the sum over channels given a particular weight w_{ij}, and each layer weighted by the total energy in that layer E_j:

$$\bar{x} = \frac{\sum_j E_j \sum_i w_{ij} x_{ij}}{\sum_j E_j \sum_i w_{ij}} \tag{5.14}$$

where x_{ij} is the central position of tower i in layer j.

Three kinds of weights were tried in Eq. (5.14). The first was just a simple weighting with energy, namely $w_{ij} = E_{ij}$, where E_{ij} is the energy deposited in layer j of tower i. In the second method, we set $w_{ij} = \sqrt{E_{ij}}$,

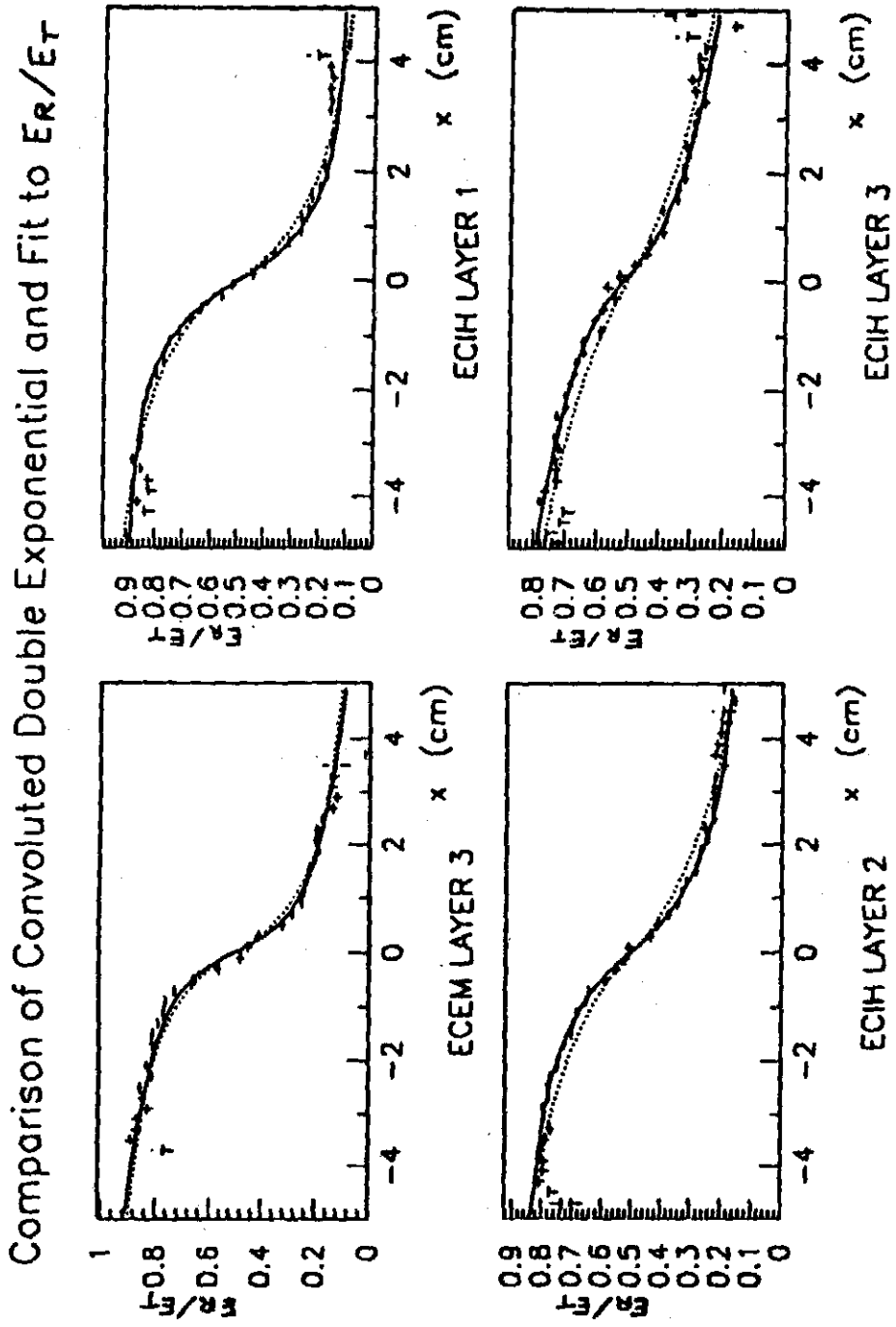

Figure 5.18 E_R/E_T plotted as a function of impact position $x = x_0 - x_{edge}$ for four calorimeter layers. The solid line is a double exponential fit and the dotted line is the curve from the convoluted double exponential parameters.

in order to give greater weight to the outer towers that have lower energy. This weighting is known to reduce the dependence of the extracted position on the distance of the impact point x^0 from a pad edge relative to that of the linear center of gravity calculation [72]. The third method employed weights that took into account the exponential fall-off in energy of particle showers with transverse direction; here the w_{ij} were set to zero or to the value of $[W_0 + \ln(E_{ij}/E_{Tj})]$, whichever was larger, where $E_{Tj} = \sum_i E_{ij}$ is the total energy in layer j and W_0 is a free parameter obtained from a fit to data [73]. Weighting according to logarithm of the energy produces weights that tend to change linearly with transverse distance of the tower i from the the point of incidence, thereby improving the accuracy of the simple center-of-gravity formula. The parameter W_0 acts both as a threshold cut on the energy needed to include a tower in the calculation of the position, and to set the relative importance of the tails of the shower in the weighting process.

A second set of methods for determination of positions of showers uses a center-of-gravity technique, but only the single layer that has the greatest amount of energy deposited in it. Here the sum of Eq. (5.14) extends only over this layer labeled as j_{max}:

$$\bar{x} = \frac{\sum_i w_{ij_{max}} x_{ij_{max}}}{\sum_i w_{ij_{max}}} \tag{5.15}$$

Again, the three weights described above were used for the sum over towers within the maximum layer, namely 1) $w_{ij_{max}} = E_{ij_{max}}$, 2) $w_{ij_{max}} = \sqrt{E_{ij_{max}}}$, and 3) $w_{ij_{max}}$ = either zero or $[W_0 + \ln(E_{ij_{max}}/E_{Tj_{max}})]$, whichever was greater. This procedure is similar to what tried in the case of electromagnetic showers and may prove useful in cases when a shower is not fully contained

in the transverse direction in all the layers of the calorimeter.

The corrected-center-of-gravity method was also investigated for hadronic showers. However, because of variation in tower size 2Δ from layer to layer, this method was used only on the layer that contained the largest energy in an event. The value of $\bar{x}$ obtained using the the energy-weighted center-of-gravity calculation was corrected to obtain x_{ccog} as was done in Eq. (5.8). The value of the ratio Δ/S for 150 GeV hadronic showers at $\eta = 2.55$, calculated using the fits to Eq (5.9) decreased from 1.1 to 0.3 with the depth of the longitudinal layer. These ratios are substantially smaller than for electromagnetic showers in ECEM layer 3 because hadronic showers are significantly wider. The relative corrections to the center-of-gravity calculation were consequently much smaller for hadronic showers. An attempt was also made to correct the center-of-gravity position using third order polynomial fits to the "S-curve" observed in the data.

The final method used to reconstruct central positions of hadronic showers was the iterative double-exponential technique using Eq. (5.9), that gave good results for electromagnetic showers. Positions were calculated using both the parameters from the convoluted double exponential fits to the transverse shape Eq. (5.12) with D=0, and those from the fits to the observed E_R/E_T ratio. For the case of the E_R/E_T ratio, fits were made to obtain the average shower shape for single layers when they had the maximum energy deposition, as well as to the separate layers, independent of the location of the layer with largest energy. The shape parameters from the fits to the layers with maximum energy were used only for calculating positions in such layers, while

the parameters from the fit to the mean shape for each layer were used when all layers were included in the calculation of positions.

5.2.4 Results for Hadronic Position Resolution

As in the case of electrons, the trajectories of beam pions were determined using the PWCs, and then extrapolated to various depths within the calorimeter. The overall offset between the PWCs and the calorimeter was determined experimentally in the following way. As can be deduced from Eq. (5.7), for showers at the edge of a pad where there is equal sharing of energy on either side of the edge, we obtain $\bar{x} = x_0$. Therefore, the overall offsets, $\bar{\phi} - \phi_{PWC}$ and $\bar{r} - r_{PWC}$ were determined from events with positions at the edge of a tower. In particular, the events had to have an energy difference between the left and the right of an edge of the tower with the largest energy that was less than 5% of the total energy of the shower. The offsets observed at $\eta = 2.55$ were $\bar{\phi} - \phi_{PWC} = 0.008 \pm 0.003$ rad, and $\bar{r} - r_{PWC} = -7.5 \pm 0.4$ mm. The position resolution was subsequently determined using Gaussian fits to the difference between the measured and extrapolated impact positions, correcting for these offsets, as was done for electromagnetic showers. An example of one of these Gaussian fits is given in Fig. 5.19.

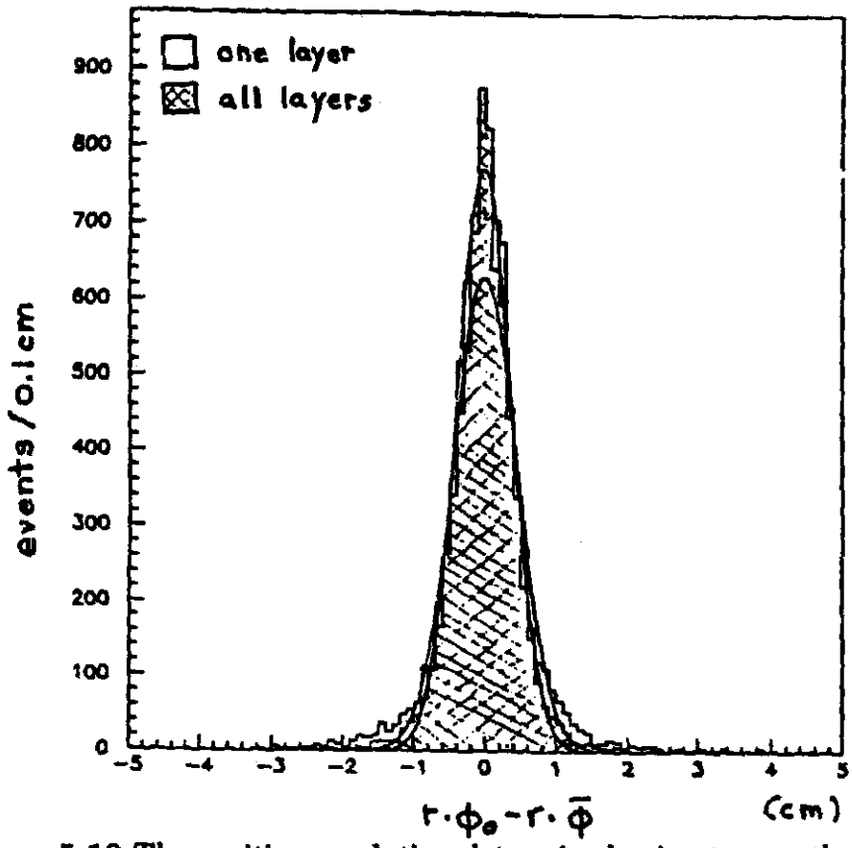

Figure 5.19 The position resolution determined using two methods for 150 GeV pions entering at a pseudorapidity of $\eta = 2.55$. For the method using only one longitudinal layer, the Gaussian fit has a mean of $\mu = .01 \pm 0.05$ mm and a standard deviation 4.49 ± 0.06 mm; using all the layers the Gaussian fit has a mean of $\mu = -.13 \pm 0.04$ mm and a standard deviation 3.80 ± 0.04 *mm*.

Position reconstruction based on the center-of-gravity algorithms described in the previous section were applied to 150 GeV pions at $\eta = 2.55$. Without applying any energy thresholds, the results obtained for azimuthal and radial coordinates, with their statistical errors, are listed respectively in the first column in Tables 5.4 and 5.5. Radial resolutions are typically 0.2

- 1.2 mm worse than azimuthal resolutions. This is likely due to the non-rectangular nature of the pad geometry, namely curved pad edges of constant ϕ dividing the radial sections. When all layers were included in the calculation of position, the best resolutions were typically found using the weighting $w_{ij} = E_{ij}$. In the case where only the layers with maximum energy were used, the logarithmic energy weighting scheme appeared to yield best results. The parameters W_0 for the logarithmic weights were determined by minimizing the resolution. The values of W_0 varied from 3.0 to 3.8 (corresponding to effective energy threshold cuts of 5.0% to 2.2% of the total energy in the layer, E_T) with the larger values required for the azimuthal coordinate. This implies that the towers near the centers of showers must be given greater weight for the radial than for the azimuthal coordinate in order to achieve better precision in the calculation of shower centers. This effect is probably due to the asymmetric nature of the shower profile in the radial dimension, which is caused by the cylindrical geometry of the end calorimeter.

Two kinds of energy thresholds can be used to optimize the calculated position resolutions: a requirement can be imposed on the minimum energy (T) for a tower to be included in the total sum, and a requirement on the energy T_L for a layer to be included in the sum. Initial values chosen for these thresholds that provided good results for the energy-weighted center-of-gravity calculations at 150 GeV were: $T = 150$ ADC cnts and $T_L = 4000$ ADC cnts. (These cuts correspond to using on the average, four layers and eight towers per layer for calculating position.) The results of using these threshold values for all the calculational methods appear in the second columns of Tables 5.4 and 5.5. The position resolution improves by as much as 2.4 mm

Table 5.4

Hadronic Azimuthal Position Resolution at $\eta = 2.55$

Weighting (w_{ij})	Resolution (mm) No Energy Threshold	Constant Energy Threshold	Optimized Energy Threshold
Center-of-Gravity: All layers included in calculation			
E_{ij}	3.786 ± 0.041	3.747 ± 0.042	3.512 ± 0.040
$\sqrt{E_{ij}}$	5.51 ± 0.05	4.89 ± 0.06	3.87 ± 0.05
Logarithmic $W_0 = 3.3$	4.42 ± 0.05	3.85 ± 0.05	3.68 ± 0.05
Center-of-Gravity: Only maximum layer included in calculation			
$E_{ij_{max}}$	4.51 ± 0.06	4.39 ± 0.05	4.08 ± 0.05
$\sqrt{E_{ij_{max}}}$	7.74 ± 0.08	5.79 ± 0.08	4.58 ± 0.07
Logarithmic $W_0 = 3.8$	3.76 ± 0.07	3.79 ± 0.07	3.75 ± 0.07
Method	**Corrected-Center-of-Gravity: Only maximum layer**		
Eq. 5.8	4.75 ± 0.07	4.46 ± 0.07	4.00 ± 0.07
Polynomial	4.52 ± 0.06	4.35 ± 0.05	4.05 ± 0.05

Table 5.5

Hadronic Radial Position Resolution at $\eta = 2.55$

Weighting (w_{ij})	Resolution (mm) No Energy Threshold	Constant Energy Threshold	Optimized Energy Threshold
Center-of-Gravity: All layers included in calculation			
E_{ij}	4.62 ± 0.06	4.22 ± 0.05	4.035 ± 0.049
$\sqrt{E}_{ij}$	6.58 ± 0.06	5.39 ± 0.07	4.07 ± 0.05
Logarithmic $W_0 = 3.0$	4.59 ± 0.06	3.91 ± 0.05	3.67 ± 0.05
Center-of-Gravity: Only maximum layer included in calculation			
$E_{ij_{max}}$	5.33 ± 0.08	4.97 ± 0.08	4.81 ± 0.07
$\sqrt{E}_{ij_{max}}$	8.94 ± 0.10	6.49 ± 0.11	4.99 ± 0.07
Logarithmic $W_0 = 3.5$	4.10 ± 0.07	4.09 ± 0.07	4.09 ± 0.07
Method	Corrected-Center-of-Gravity: Only maximum layer		
Eq. 5.8	5.16 ± 0.08	4.48 ± 0.08	4.28 ± 0.07
Polynomial	5.13 ± 0.08	4.49 ± 0.08	4.34 ± 0.07

in one case, with the greatest improvements occuring when the weighting was $w_{ij} = \sqrt{E_{ij}}$. This is understandable because weighting by $\sqrt{E_{ij}}$ gives greater weight to towers away from the center of the showers, where a threshold requirement has a greater effect.

Optimized values of T and T_L were sought by roughly minimizing the position resolution for each of the methods used for determining position. It was found that varying T_L over the range 0-4000 ADC cnts did not materially improve the resolution, and the resolution degraded for values of T_L above this range. In the following analysis, we have therefore set $T_L = 0$. The optimum values for T are given in Table 5.6. These values were obtained from the observed dependence of the spatial resolution on T; several such selected plots are shown in Fig. 5.20. For the method where the tails of showers are more heavily weighted, namely for $w_{ij} = \sqrt{E_{ij}}$, a higher threshold usually produces better resolution. In general, there was little difference found for thresholds required to optimize the radial and azimuthal resolution. The best overall resolutions were obtained when all the longitudinal layers were included in the calculation of positions. Logarithmic weighting showed the least improvement when all the layers are included in the sums, as opposed to just the layer with maximum energy. Also, logarithmic weighting yielded the best results, when only the maximum layer was used in the calculation of position.

Table 5.6

Estimated Optimum Tower-Energy Threshold Values

Center-of-Gravity Methods

Weight	Azimuthal T (ADC cnts)	Radial T (ADC cnts)
All layers included in calculation		
E_{ij}	500	500
$\sqrt{E}_{ij}$	600	600
Logarithmic	600	750
Only maximum layer included in calculation		
$E_{ij_{max}}$	450	450
$\sqrt{E}_{ij_{max}}$	450	750
Logarithmic	400	450
Method	Corrected: Only maximum layer	
Eq. 5.8	400	450
Polynomial	500	450

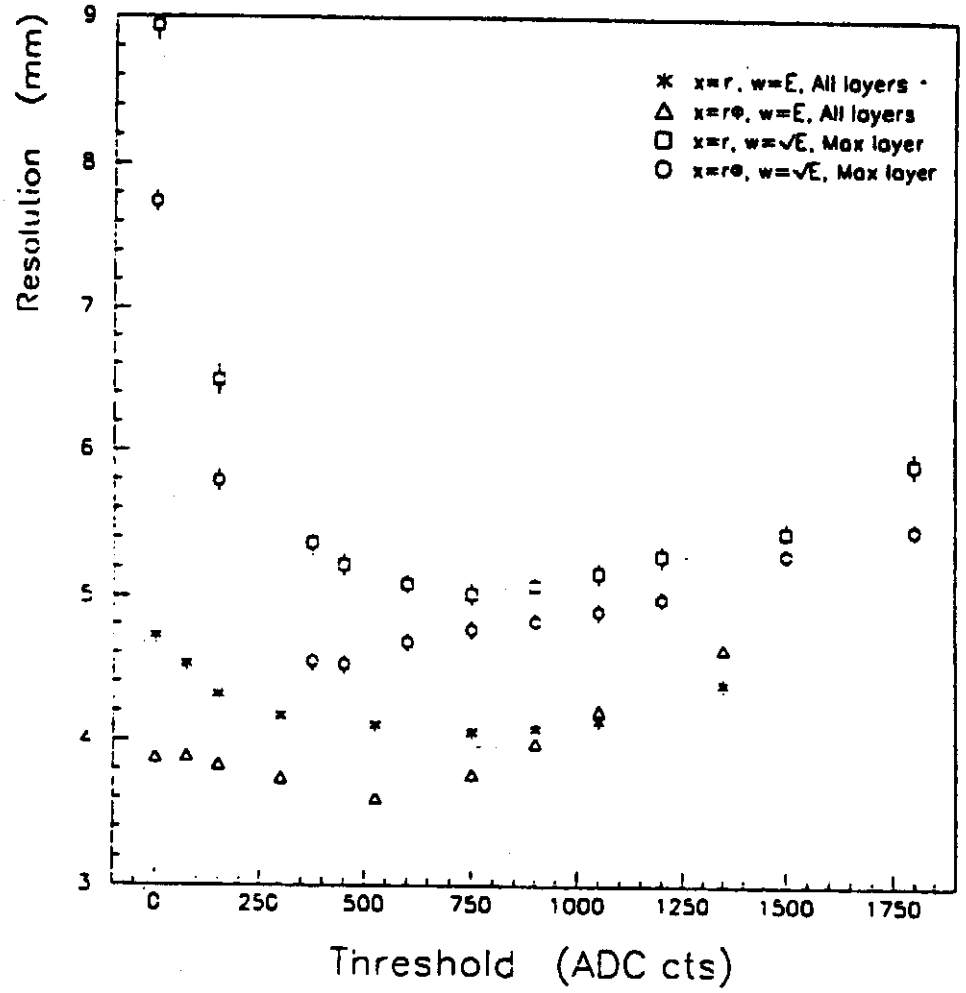

Figure 5.20 Hadronic position resolution as a function of threshold cut T. Typical results are plotted for both the radial and azimuthal coordinate.

The two methods chosen to correct the calculated position based on the center-of-gravity yielded very similar results. The results are given in Tables 5.4 and 5.5. Optimum values for T found for these two methods are given in Table 5.6. For the method using Eq. (5.8), the value of the effective shower width S that gives the best results for the radial coordinate is $S = 8.0$ mm and for the azimuthal coordinate $S = 10.4$ mm. (For ECEM layer 3, these

values were reduced by a factor of two because of the dependence of S on pad size seen in the electromagnetic analysis.) It was found that using optimized values of S that were made proportional to the width of the shower in each layer of the calorimeter did not improve the resolution. Correcting the center-of-gravity calculation improves the radial position resolution when a single maximum layer is used, by about 0.5 mm, but does not significantly affect the azimuthal resolution. Although, these methods provide some correction for the asymmetry in the radial shower shape, they do not provide any improvement to the center-of-gravity calculation because of the small value of Δ/S.

Although the measured shower profiles were used, the iterative double-exponential technique, using Eq. (5.9), gave the worst results for position resolution of all the methods studied. When all layers were used to reconstruct position, we obtained $\sigma(r\phi) = 9.48 \pm 0.09$ mm for the convoluted double-exponential fit, Eq (5.12) and $\sigma(r\phi) = 8.18 \pm 0.09$ mm from the direct fit to E_R/E_T. For the case where only the maximum layer was used, we found $\sigma(r\phi) = 8.08 \pm 0.07$ mm using the fits to E_R/E_T. The reason this method does so poorly is because of the large fluctuations that occur in hadronic showers. The average shower shape over a large number of events does not correctly describe each individual shower. Consequently, the methods that take greater cognizance of the structure of each event are more reliable. This is also born out in the Monte Carlo analysis. The Monte Carlo results yield $\sigma(r\phi) = 11.3 \pm 0.7$ mm for the convoluted double exponential, and $\sigma(r\phi) = 9.1 \pm 0.8$ mm for the fits to E_R/E_T when all layers are used, and $\sigma(r\phi) = 9.9 \pm 0.7$ mm when only the maximum layer is used. These resolutions are considerably

larger than those found using the other analysis methods on Monte Carlo events, as is discussed below.

The position resolution was examined as a function of energy using all the above calculations, except the iterative double-exponential method. Scaled values of thresholds $T = T(150) \cdot E/150$ were used for each calculation, where $T(150)$ are the optimum thresholds at 150 GeV, and E is the total shower energy in GeV. Although lower energy showers tend not to extend deeply into the calorimeter, best resolutions even for low energies were obtained, nevertheless, when the information from all the layers was used. Figure 5.21 shows the azimuthal and radial position resolution as a function of energy for the weights $w_{ij} = E_{ij}$ when using the single maximum layer and all the layers (the latter yielded the best results). As can be seen from a fit to data in Fig 5.21, using all layers, the optimized resolution scales essentially as $E^{-1/2}$, with $\sigma(r\phi) = (54.9 \pm 1.3)E^{-0.551\pm0.005}$ mm and $\sigma(r) = (49.4 \pm 1.9)E^{-0.502\pm0.008}$ mm. These results are only slightly worse than the prediction of Eq. 3.9: $38.8/\sqrt{E}$ mm.

To compare with data, the position resolution was also studied for the plate-level Monte Carlo simulation. Results for the center-of-gravity and corrected-center-of-gravity for 150 GeV pions are given in Tables 5.7 and 5.8. The optimized values for W_0, S and T found for the data were used in the Monte Carlo analysis. In general, the Monte Carlo resolutions are only somewhat worse than those in the data. The logarithmic weighting scheme using the optimized parameters, however, yields resolutions 1.5 - 2 mm worse than data. This seems to indicate that the values of W_0 that minimize the

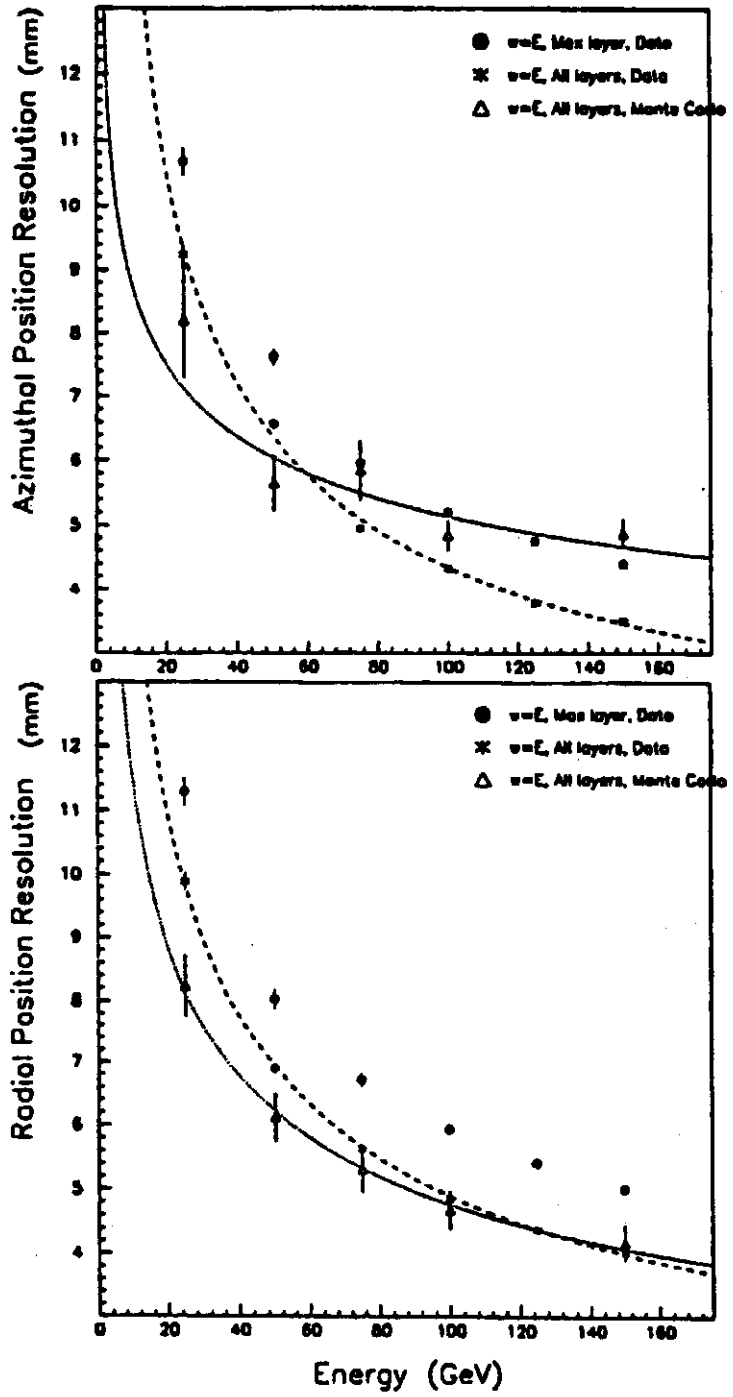

Figure 5.21 The azimuthal and radial hadronic position resolution plotted as a function of energy for data and for Monte Carlo. The dashed lines are best fits to the data, and the dotted lines are best fits to the Monte Carlo for the case when all layers are used in the calculation of position.

resolution for the data, do not do as well for the Monte Carlo. We conclude that the shower shapes and fluctuations in the data may not be modeled accurately enough in the current D-Zero Monte Carlo. The dependence of the Monte Carlo resolution on energy is also given in Fig. 5.21. There is better agreement between the data and Monte Carlo for the radial resolution than for the azimuthal resolution. The fit to the energy dependence of the optimized Monte Carlo results are not very good for the azimuthal direction, and yield $\sigma(r\phi) = (15.1 \pm 6.9)E^{-0.24\pm1.0}$mm. The fit for the radial dimension

Table 5.7

Hadronic Azimuthal Position Resolution

at $\eta = 2.55$ in the Monte Carlo

Weighting (w_{ij})	Resolution (mm) No Energy Threshold	Resolution (mm) Optimized Energy Threshold
Center-of-Gravity: All layers included in calculation		
E_{ij}	4.62 ± 0.25	4.86 ± 0.23
$\sqrt{E}_{ij}$	5.93 ± 0.29	5.03 ± 0.39
Logarithmic $W_0 = 3.3$	7.11 ± 0.40	5.61 ± 0.36
Center-of-Gravity: Only maximum layer included in calculation		
$E_{ij_{max}}$	5.57 ± 0.30	5.03 ± 0.27
$\sqrt{E}_{ij_{max}}$	8.24 ± 0.46	5.01 ± 0.36
Logarithmic $W_0 = 3.8$	8.04 ± 0.43	6.23 ± 0.57
Method Corrected-Center-of-Gravity: Only maximum layer		
Eq. 5.8	5.19 ± 0.30	4.37 ± 0.44

is quite good, and yields $\sigma(r) = (28 \pm 13)E^{-0.38 \pm 0.11}$mm. The idealized $E^{-1/2}$ behavior is not as evident for the Monte Carlo resolutions as for the data. This is most likely due to the fact that the approximations to fluctuations in the Monte Carlo are not handled properly.

Table 5.8

Hadronic Radial Position Resolution

at $\eta = 2.55$ in the Monte Carlo

Weighting (w_{ij})	Resolution (mm) No Energy Threshold	Resolution (mm) Optimized Energy Threshold
Center-of-Gravity: All layers included in calculation		
E_{ij}	4.37 ± 0.24	4.18 ± 0.28
$\sqrt{E}_{ij}$	7.37 ± 0.36	4.79 ± 0.31
Logarithmic $W_0 = 3.0$	7.60 ± 0.38	5.66 ± 0.32
Center-of-Gravity: Only maximum layer included in calculation		
$E_{ij_{max}}$	5.77 ± 0.35	4.99 ± 0.32
$\sqrt{E}_{ij_{max}}$	8.87 ± 0.50	5.11 ± 0.34
Logarithmic $W_0 = 3.5$	9.65 ± 0.72	6.04 ± 0.44
Method Corrected-Center-of-Gravity: Only maximum layer		
Eq. 5.8	5.96 ± 0.35	4.92 ± 0.31

The impact of the angle of incidence into the calorimeter and of the tower size, on the hadronic position resolution was examined by studying the response to pions at $\eta = 2.3$. At $\eta = 2.3$ the pads are about 1.7 times larger in

area, than the pads at $\eta = 2.55$. Only three methods for calculating position were studied at $\eta = 2.3$; these corresponded to weighting with $w_{ij} = E_{ij}$ for the maximum layer as well as for all layers, and logarithmic weighting for all layers. Each of these calculations was performed using $T = 150$ ADC cnts, the optimized threshold at $\eta = 2.55$, $T(\eta = 2.55) = T(150) \cdot E/150$, and $T = 1.7 \cdot T(\eta = 2.55)$. In general, the best results were obtained for the radial coordinate using logarithmic weighting and the highest threshold. The azimuthal resolution is usually best for the $w_{ij} = E_{ij}$ weighting, all layers included with the $T(\eta = 2.55)$ threshold. This implies that pad dimensions are not the only factor that can govern the choice of threshold for hadronic showers. (In the case of electrons, it was found that the optimum threshold at $\eta = 2.25$ was about 1.6 times the optimum threshold at $\eta = 2.55$.) In Fig. 5.22, the hadronic resolutions are plotted as a function of energy and compared to the results obtained at $\eta = 2.55$, for the $w_{ij} = E_{ij}$ weighting, using all layers, and thresholds set to $T = 1.7 \cdot T(\eta = 2.55)$. The results at $\eta = 2.55$ show consistently better resolution than at $\eta = 2.3$ (by ≈ 0.5 mm). This is what would be expected from the difference in pad sizes.

5.2.5 Conclusions

The observed longitudinal development of hadronic showers can be modeled with the usual parametrization of Bock et. al. The best fit to the transverse hadronic shower profile observed was obtained using the sum of two modified Lorentzians. The best overall position resolution results for pions at $\eta = 2.55$ were found by including all the longitudinal layers in the calculation, using optimized energy thresholds, and using weights of $w_{ij} = E_{ij}$ for

the ϕ coordinate and logarithmic weights for the r coordinate. When only the single layer with the largest energy signal was used, the best weights for both coordinates were the logarithmic ones. Applying corrections to the simple center-of-gravity calculations for a single layer, improved the radial spatial resolution by 0.5 mm but did not alter the azimuthal resolution. Methods that involved fits to the average shower shape observed in each layer gave resolutions 4.5 - 5.5 mm larger than those obtained using the weighting techniques on each individual event. The energy and angular dependence of the hadronic position resolution were as expected.

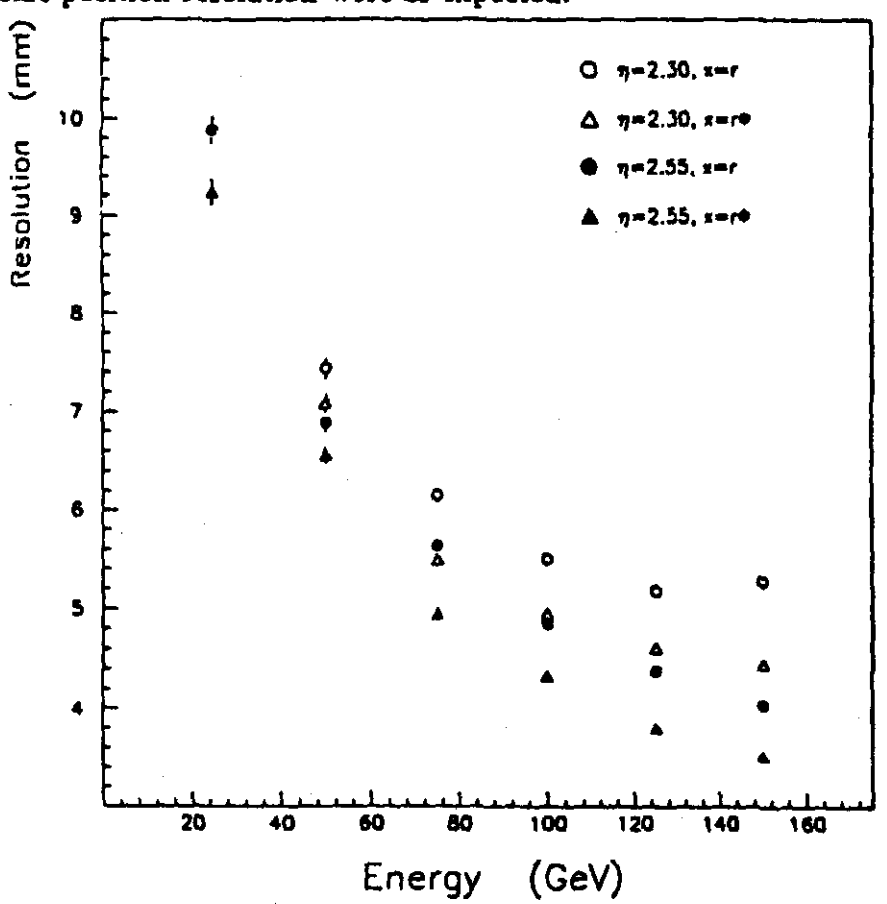

Figure 5.22 The radial and azimuthal hadronic position resolution plotted as a function of energy, with $T = T(\eta = 2.55)$ at $\eta = 2.55$ and $T = 1.7 \cdot T(\eta = 2.55)$ at $\eta = 2.30$.

The results from Monte Carlo simulations generally agree with the shower shapes and position resolution behavior observed in the data. One difference seen between the data and Monte Carlo was that the parameters W_0 that optimized the resolutions measured in the data did not optimize the Monte Carlo spatial resolutions. The other major difference was that the energy dependence of the position resolution in the Monte Carlo did not follow the idealized $E^{-1/2}$ behavior. These two differences point to the fact that the fluctuations seen in hadronic showers are not properly handled in the D-Zero Monte Carlo.

CHAPTER 6

ANALYSIS OF JET ENERGY RESPONSE

An analysis of the energy response of the calorimeter to single particles is important for determining the energy response to hadronic jets. This is because hadronic jets are merely collimated sprays of single particles. As stated in Chapter 2, because jet production properties depend on the characteristics of the energy and momentum transfers, the precise measurement of jet energies is crucial for establishing the nature of the dynamics. Measurements of production properties, such as the single-jet cross section or jet-jet correlations, provide checks of the theory of quantum chromodynamics (QCD). The single jet differential cross section $d\hat{\sigma}/d\hat{t}$ has an E_T^{-4} energy dependence, and consequently an uncertainty in the measurement of jet energy of 10% leads to an uncertainty in the cross section of 40% [74]. (That is, $\Delta\hat{\sigma}/\hat{\sigma} \approx 4\Delta E_T/E_T$.)

There are several factors that contribute to systematic uncertainties in the measurement of jet energy. Properties of the calorimeter, such as non-uniform energy response due to spaces between modules, or the presence of uninstrumented or "dead" material (e.g. walls of cryostats), can cause mismeasurement of energy. Any non-linear response at low energy contributes greatly to the overall uncertainty because jets are typically made up of many low energy (< 5 GeV) particles. To determine the effect of non-linearities

on calorimeter response to jets, the specific particle contents of jets must be known. For example, the fraction of electromagnetic particles and their energies and the fraction of hadronic particles and their energies must be measured. An uncertainty arises from the inability to measure the exact particle content (known as the "fragmentation" uncertainty). Uncertainties in the calibration of the calorimeter also affect jet-energy measurement.

Another major factor, that arises from the physics of jets not from the design of the detector, is the algorithm chosen to define a jet. In D-Zero, we define a jet by the energy in a cone of radius $R = \sqrt{\Delta\phi^2 + \Delta\eta^2} = 0.7$ about the axis of the jet. Energy mismeasurement arises because some of the energy of the jet may leak outside of this cone, and energy from another jet can leak into the cone. A problem also arises when the algorithm merges two closely spaced apart jets into one. The algorithm dependent effects just listed are refered to collectively as "clustering effects".

Figure 6.1 shows a breakdown of the systematic uncertainty in jet energy for the CDF experiment from the sources described above [75]. Any non-linear response to low-energy particles and the simulation of cracks and dead material in the calorimeter generate large uncertainties in the measurement of the cross section for low-energy jets. Consequently, as we have emphasized, an understanding of the calorimeter's response to low energy particles and the effects of non-unformities are therefore crucial for determining the response to jet energy.

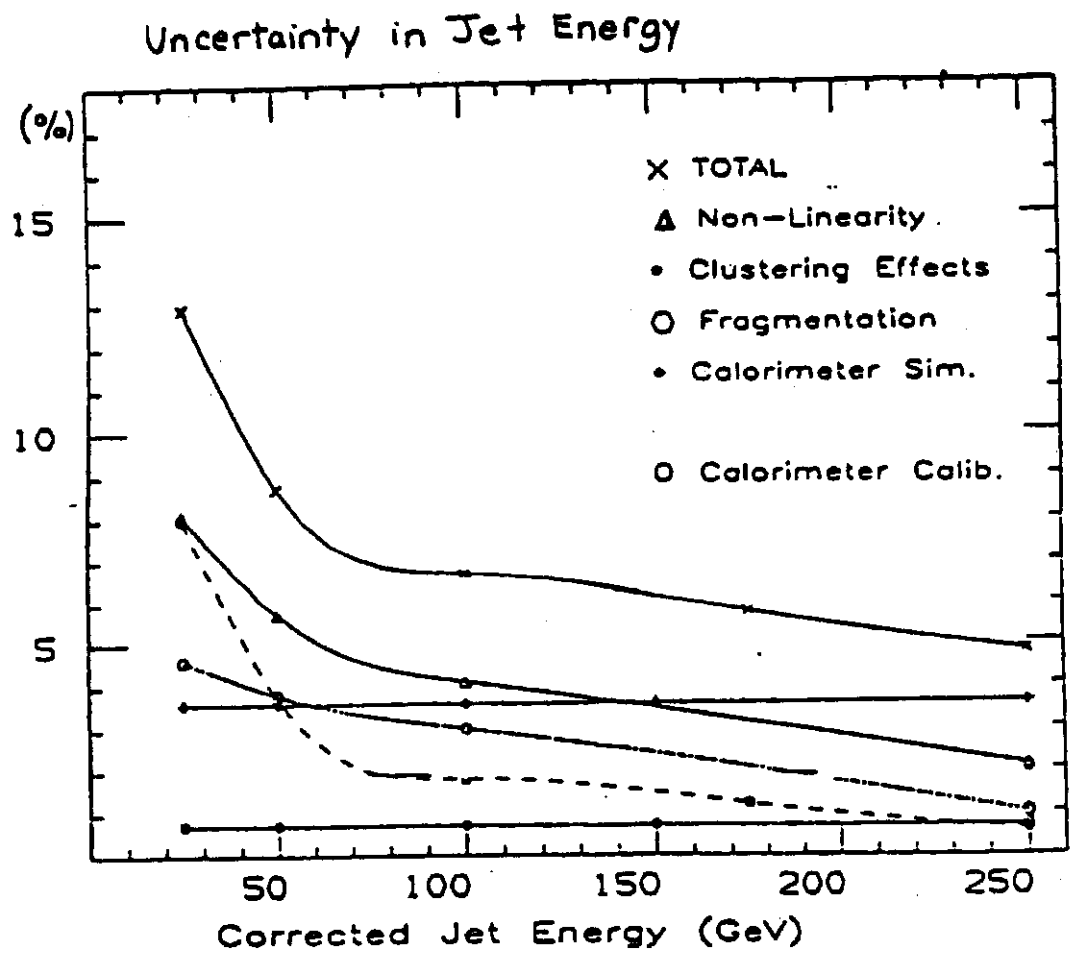

Figure 6.1 The systematic uncertainty in jet energy for the CDF experiment. The total and the contributions from different sources are shown separately.

An analysis of the jet-energy response inferred from the single-particle response of the D-Zero calorimeter will be presented in this chapter. The analysis will involve three main steps. First, the response of the calorimeter modules to single particles in the test beam and in a Monte Carlo simulation will be found. Next, the single-particle content of jets will be determined from jets generated using the ISAJET program [76]. Finally, the single-particle en-

ergy response of the calorimeter and the particle content of jets will be combined to determine the response to jet energy, R_J. This will be done using the single particle response observed both in the test beam R_{JTB} and in the Monte Carlo R_{JMC}. Clearly, the derived response will be very sensitive to uncertainties in the fragmentation of jets and to the response of the calorimeter at low energies. To establish which aspects of the calorimeter's response to jet energy can be determined from the response to single particles, our derived energy response to jets R_{JMC} will be compared to that from a detailed Monte Carlo simulation for jets interacting directly in the calorimeter R_{JD}. A comparison of the jet energy response from the Monte Carlo R_{JMC} and the response from the test beam R_{JTB} will provide information about how differences in single particle response affect the jet energy response.

6.1 Energy Response to Single Particles

The energy response to single particles was obtained by studying the ratio of the energy reconstructed in the calorimeter (E_R) to the incident energy of the particle (E). This was examined on an event-by-event basis for both the total energy $R_E = E_R/E$ and the total transverse energy, $R_{E_T} = E_{TR}/E_T$, where $E_T = E \sin\theta_0$, with θ_0 being the angle of incidence into the calorimeter. The reconstructed total energy was determined from a sum of the energies in the calorimeter towers with energy above a given threshold: $E_R = \sum_i E_i$. The reconstructed transverse energy was defined in an analogous manner: $E_{TR} = \sum_i E_i \sin\theta_i = E_R \sin\theta_R$, where θ_i corresponds to the position of each tower in the polar angle θ and θ_R is the reconstructed central value of the angle of the shower.

6.1.1 Response of the Monte Carlo

The generated events used to obtain the Monte Carlo response of the calorimeter consisted of seven electron and seven pion runs at energies ranging from 1 to 50 GeV. Each run contained 2400 events that were evenly distributed in η and ϕ over all angles in ϕ and $-3.0 \geq \eta \geq 3.0$. The detector response was simulated using a "mixture" Monte Carlo, without noise, of the kind described in Appendix A.

Figures 6.2 and 6.3 display the R_E and R_{E_T} values as a function of incident particle energy for five regions of pseudorapidity, $|\eta|$. The energy sums were taken over all the towers in the calorimeter with greater than 1 MeV of energy. The response appears to level off at higher energies. In general, the reconstructed energy for electrons is higher than that for pions of the same energy. (This is what one might expect from a slightly non-compensating calorimeter with a measured e/π ratio of 1.09 at 10 GeV.) The one exception is in the transverse energy response for pions in the η range centered at about $|\eta| = 2.7$. At all energies, the response to pions in this region of η exceeds that to electrons. This effect can be traced down to the nature of the algorithm commonly used to calculate transverse energy, as will be discussed below.

6.1.2 Transverse Energy Bias

Because the transverse energy of showers and jets is usually calculated in the manner described above [77], it is important to understand how this bias in the highest $|\eta|$ region arises. The bias observed in the reconstructed

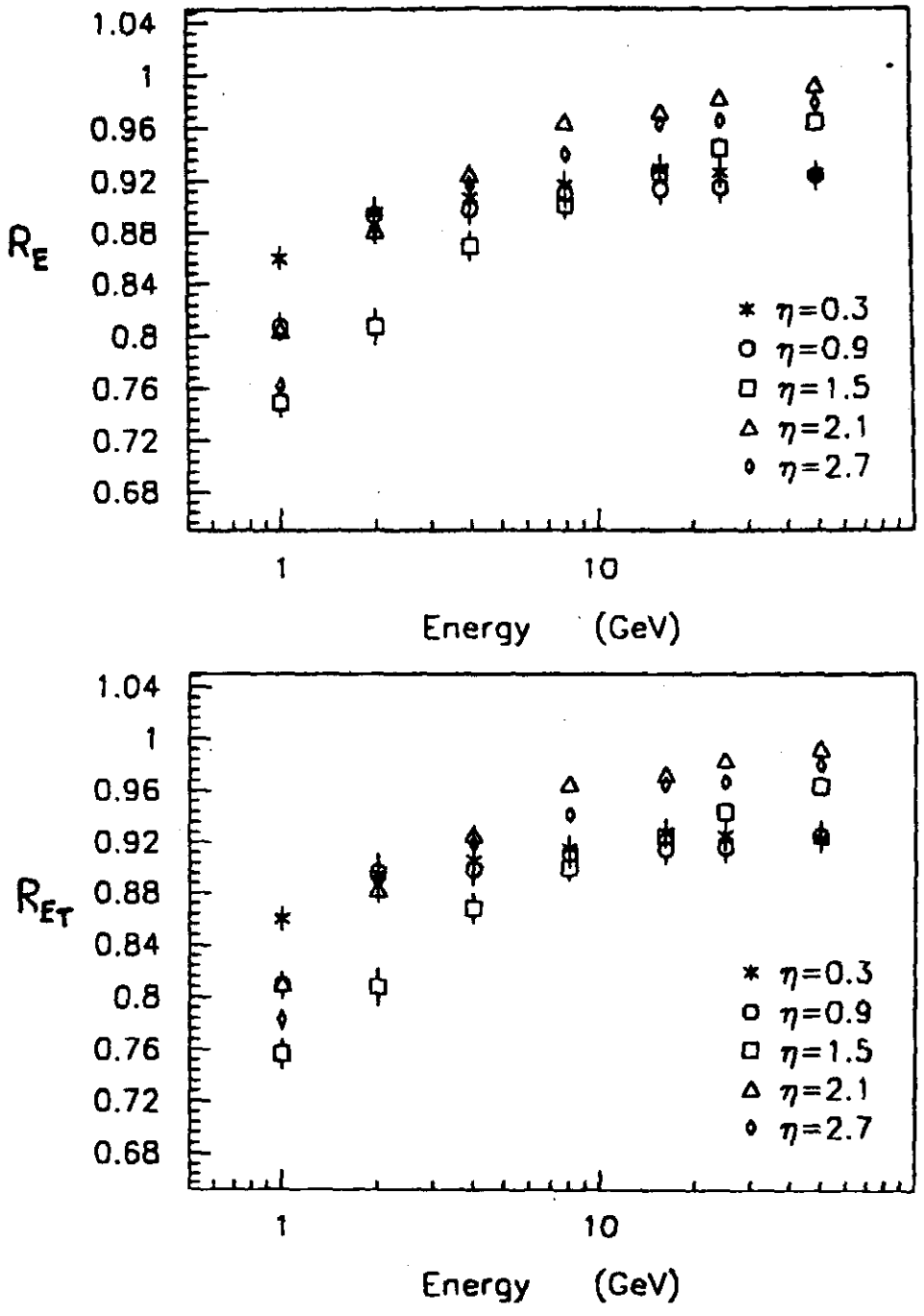

Figure 6.2 The ratios of reconstructed to incident single-particle total energies and transverse energies for electrons obtained in the Monte Carlo.

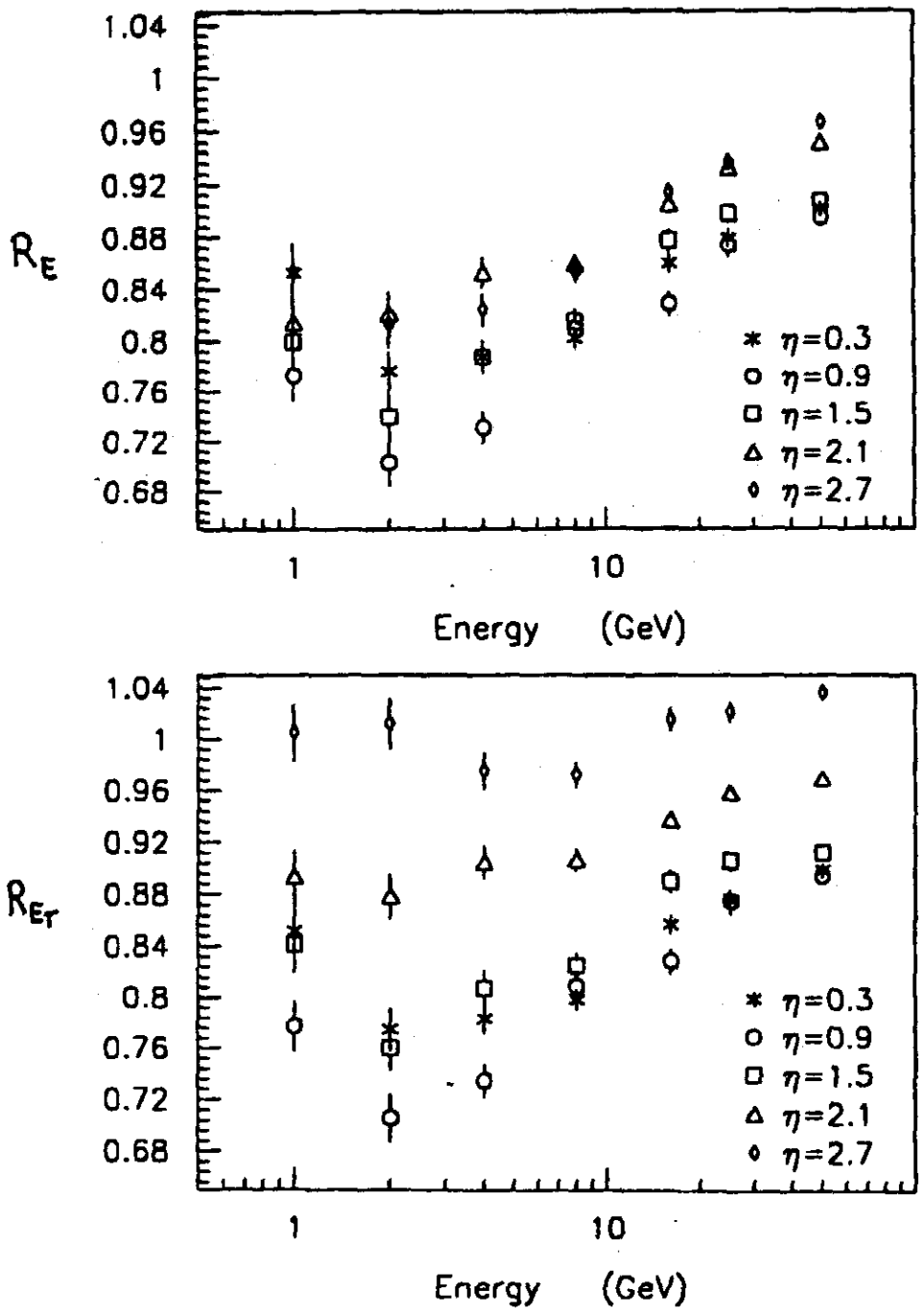

Figure 6.3 The ratios of reconstructed to incident single-particle total energies and transverse energies for pions obtained in the Monte Carlo.

transverse energy for single pions, shown in Fig 6.3, is a result of the large transverse size of pion showers. For example, when a particle enters the end calorimeter at some angle θ_0, it deposits energy in a transverse pattern that is essentially circular. More of the energy of the developing shower is therefore deposited outside of an arc of constant θ than inside that arc (toward the beam axis). This is illustrated in Fig 6.4. At high pseudorapidity, where the radius of curvature of an arc of constant θ is comparable to the transverse radius of the shower, the effect on the calculation of E_{TR} can produce a substantial bias. This bias produces a shift of E_{TR} towards higher values because more energy is deposited in towers located at larger θ. This is what causes the effect observed for pions in the region of $|\eta| = 2.7$.

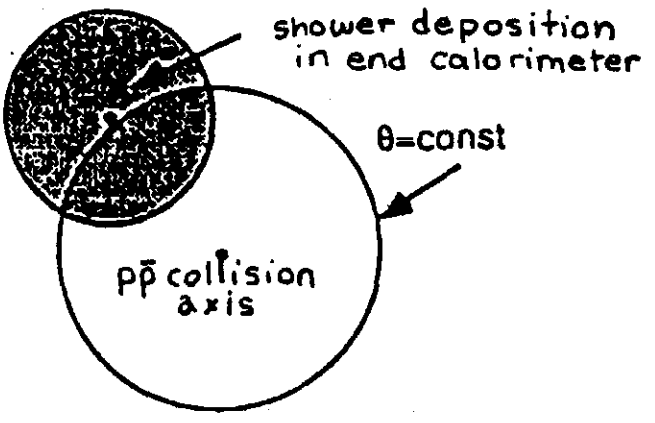

Figure 6.4 If a hadron shower is circularly symmetric, a particle entering the end calorimeter at an angle θ deposits more energy outside the arc of constant θ than inside it.

The magnitude of this effect can be estimated as follows [78]. First, we assume that we have a very fine-grained calorimeter a distance R_o from the particle's origin. The shower is assumed to be symmetric around the axis of the shower at θ_0, with a radial energy deposition characterized by the density, $\rho(r)$. One can then define the following quantities:

$$E_R = \int\int \rho(r) r dr d\phi \tag{6.1}$$

$$E_R \sigma^2 = \int\int \rho(r) r^2 r dr d\phi \tag{6.2}$$

$$E_{TR} = \int\int \rho(r) \sin\theta r dr d\phi \tag{6.3}$$

where σ is the r.m.s. (root-mean-squared) radial width of the shower, θ is the angular position of energy deposition in the shower, and r and ϕ are the coordinates transverse to the axis of the shower shown in Fig. 6.5.

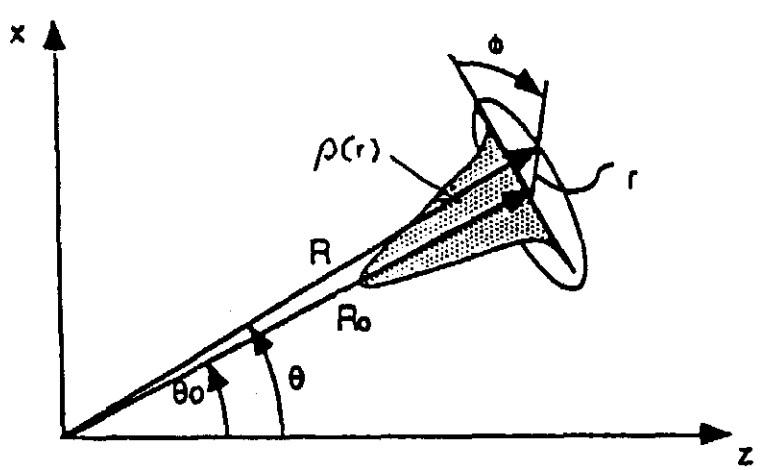

Figure 6.5 The integration of the deposited energy over the extent of a particle shower.

Evaluating the integrals in Eqs. 6.1-6.3, we find that:

$$\frac{E_{TR}}{E_R \sin\theta_0} \approx 1 + \frac{1}{2}\left(\frac{1}{2\sin^2\theta_0} - 1\right)\left(\frac{\sigma}{R}\right)^2 \qquad (6.4).$$

Consequently, the bias towards higher E_{TR} occurs for $\theta_0 > 45°$. Because there is no bias in the total reconstructed energy E_R, this is equivalent to having a bias in the reconstructed angle θ_R. The extent of the bias is a function both of the angle of incidence and of the size of the shower σ/R.

From our studies of the transverse and longitudinal shapes of test beam showers presented in Chapter 5, we can estimate the value of σ/R for 150 GeV pions. If we assume an effective R to be about 1 absorption length into the calorimeter, then we get that $R \approx 200$ cm at $\eta = 2.55$; this distance corresponds to the typical position of the maximum in energy deposition of 150 GeV pion showers (See Figure 5.13). We can also estimate σ (≈ 8 cm) from the width of 150 GeV pion showers (e.g. from just the half-width observed in ECIH layer 5), and get that $\sigma/R \approx 0.04$. Because low energy showers tend to be broader than high energy ones, and do not extend as deeply into the calorimeter, one would expect σ/R to be somewhat larger for lower energy pions. The bias would therefore be expected to increase as energy decreases.

Figure 6.6 shows the size of the bias in the reconstructed transverse energy in D-Zero, for pions plotted as a function of $|\eta|$. The values of R have been estimated from the configuration of the calorimeter and from the longitudinal position of the shower maximum. The value of the shower width, $\sigma = 9$ cm, was determined from a fit to the shower profile for 50 GeV pions. The resulting σ/R values range from 0.05 to 0.09, for $|\eta|$ between 0 and 3.

The bias observed for simulated 50 GeV pions is also plotted in Fig. 6.6 in terms of the ratio of Eq. (6.4). Our simple calculation predicts the observed shift, but underestimates its magnitude at the highest values of $|\eta|$. This may be partially due to the fact that the half-width is smaller than σ for a distribution that has significant tails in energy. For electrons or photons, this effect is negligible because such showers are quite narrow. Also, pion showers can have large fluctuations in the radial direction which are not represented well enough by just considering the effects on the second moment in r.

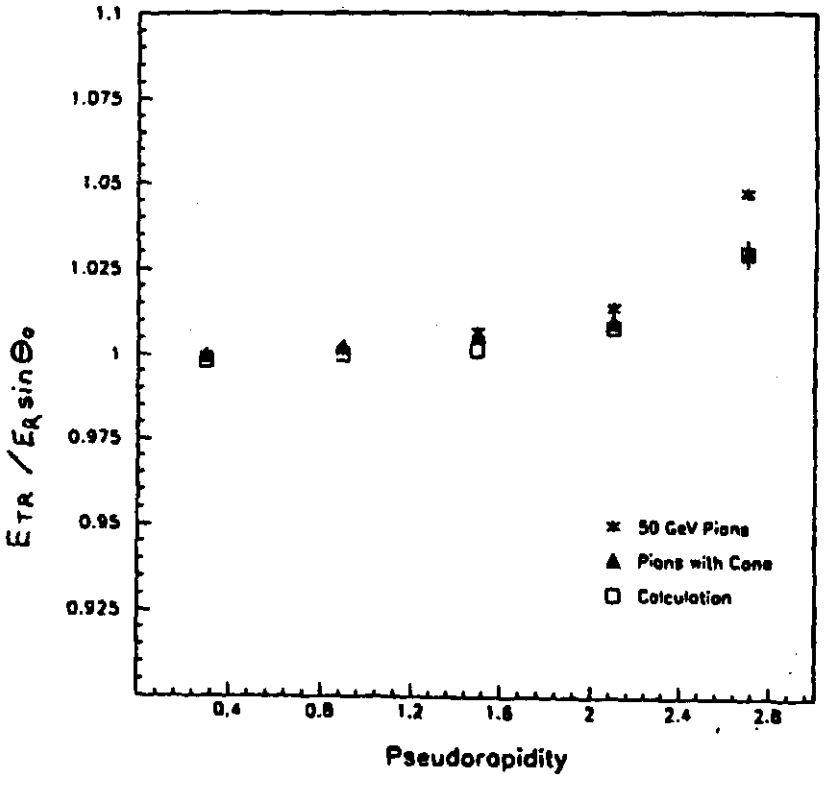

Figure 6.6 The bias in transverse energy due to shower size, shown as a function of $|\eta|$, for simulated 50 GeV pions without a cone restriction, with a cone of R=0.7 and calculated using Eq. 6.4.

The transverse energy bias due to the finite size of showers should be

observed both for hadrons and for jets, both of which have similar transverse dimensions at large $|\eta|$ [79]. One major difference between jets and single-hadronic showers, however, is that the energy of a jet is usually defined within a predetermined cone in η and ϕ. The transverse energy bias obtained for 50 GeV simulated pion showers, where only the energy within a cone of R=0.7 is summed, is plotted in Fig. 6.6. As expected, the imposition of a cone restriction decreases the bias because the outlying calorimeter cells are not included in the energy sums.

To determine the amount of energy that gets deposited outside the R=0.7 cone for single pion showers, Fig 6.7 shows the fractional difference in the reconstructed energy E_R (calculated by adding all the calorimeter towers) and the energy calculated by adding only the towers within a cone of radius R=0.7 about the incident direction of the particle. We will refer to the latter as E_J. The results for 4 GeV and 50 GeV pions are plotted as a function of pseudorapidity. The fraction of energy that escapes increases with $|\eta|$, and is somewhat greater for 4 GeV pions than for 50 GeV pions. Because the transverse energy of jets is currently calculated in D-Zero as $E_{J_T} = \sum_i E_i \sin\theta_i$ for a cone size of R=0.7, the magnitude of this effect must be incorporated into a correction to the transverse energy response for jets.

The single-particle energy response and the transverse-energy response as a function of energy for simulated electrons and pions, with and without an imposed cone of R=0.7, for five regions of pseudorapidity, was fitted to the simple form $R_E(E) = A + B\log_{10}(E)$. The fit parameters, their statistical errors and the χ^2s per degree of freedom of the fits, are given in Tables 6.1-

6.4. In the case of electrons, the fits to $R_E(E)$ and $R_{E_T}(E)$ with an imposed cone differed significantly from the fits without a cone only for $|\eta| = 2.7$, and consequently only the $|\eta| = 2.7$ results are given for the R=0.7 cone size. The fits are, in general, poor but especially for the electron simulations in the two highest $|\eta|$ regions. This is caused by a large drop in electron response at 1 GeV, which is probably due to energy losses in the central tracking chambers and in the gap between the central and end calorimeters, which become exceedingly important at low energies. Because these losses would occur for low energy electrons or photons within jets, we can not discard these points. The fits to $R_{E_T}(E)$ for pions are shown in Fig. 6.8. The fits again are poor, and the rise in the pion response at 1 GeV is not completely understood, but may be due to fact that pions lose their kinetic energy mostly by ionization below 2 GeV, as discussed in Chapter 3.

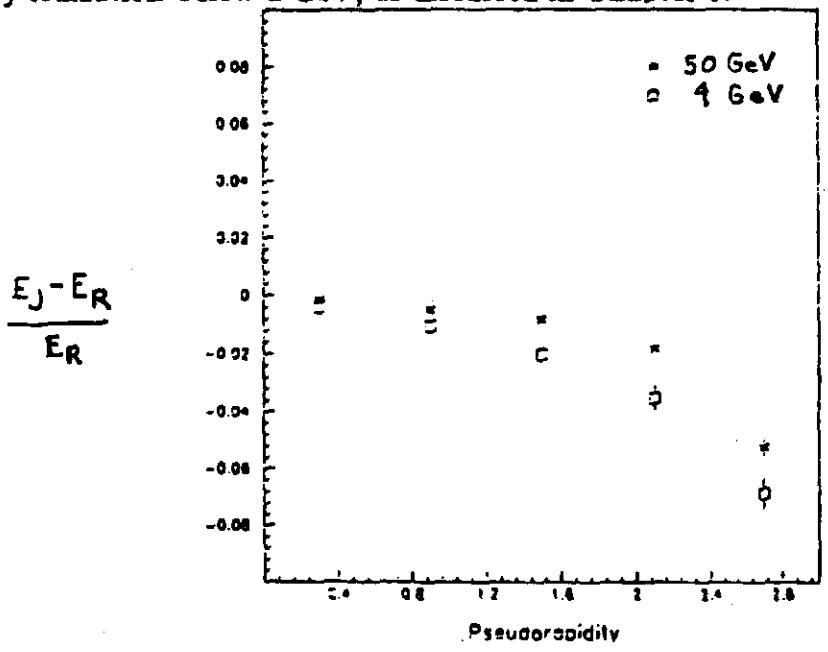

Figure 6.7 The fractional difference between the reconstructed energy in D-Zero obtained with (E_J) and without (E_R) a cone of R=0.7 imposed for simulated 4 GeV and 50 GeV pion showers, shown as a function of $|\eta|$.

These initial simulations of the D-Zero detector are continuing to be developed and as more sophisticated calculations become available, better approximations and fits to the simulations will be required to estimate corrections to the data. At this juncture, the kind of fits we have presented to $R_E(E)$ do not present a limitation to the analysis of the experimental results.

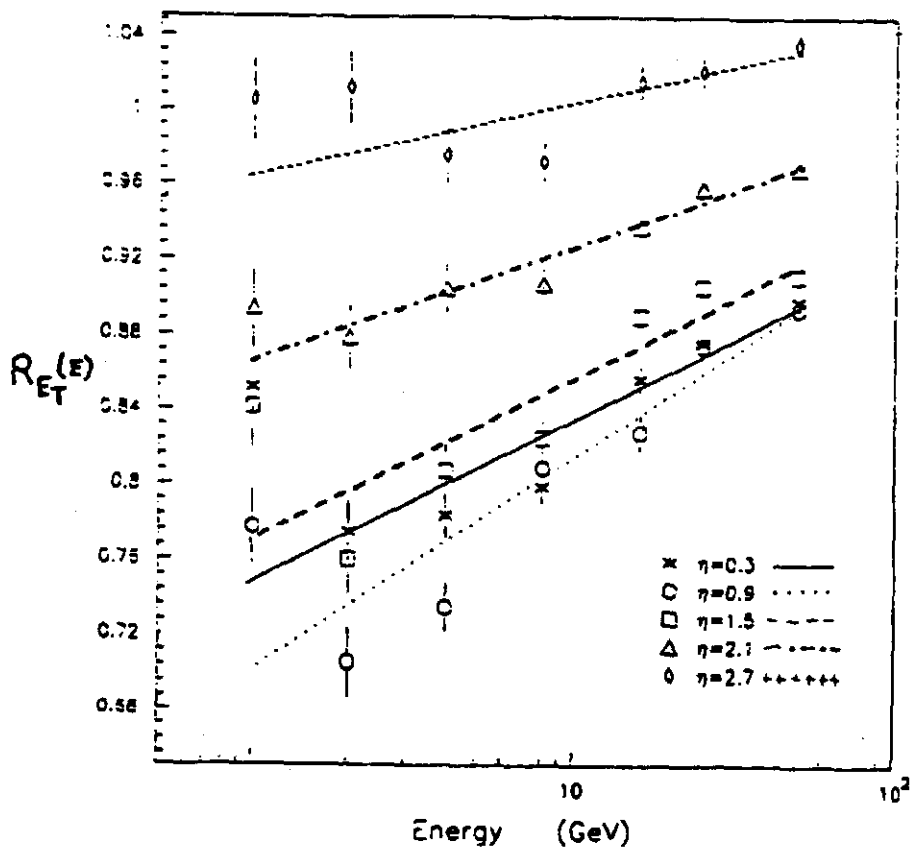

Figure 6.8 The results for and fits to, $R_{E_T}(E)$ for pions generated in the Monte Carlo.

Table 6.1

Parameters for Fits to Single-Particle Energy Response in the Monte Carlo

$$R_E(E) = A + B\log_{10}(E)$$

η	A	B	χ^2
	Electrons		
0.3	0.873 ± 0.007	0.039 ± 0.007	1.24
0.9	0.841 ± 0.008	0.058 ± 0.008	4.73
1.5	0.776 ± 0.008	0.118 ± 0.007	3.21
2.1	0.857 ± 0.005	0.0844 ± 0.0034	22.8
2.7	0.828 ± 0.005	0.0939 ± 0.0035	33.8
	Pions		
0.3	0.750 ± 0.010	0.087 ± 0.008	7.27
0.9	0.697 ± 0.011	0.116 ± 0.008	5.47
1.5	0.742 ± 0.011	0.100 ± 0.008	4.75
2.1	0.789 ± 0.009	0.097 ± 0.007	2.14
2.7	0.771 ± 0.010	0.115 ± 0.007	5.11

Table 6.2

Parameters for Fits to Single-Particle Transverse Energy Response in the Monte Carlo

$$R_{E_T}(E) = A + B\log_{10}(E)$$

η	A	B	χ^2
		Electrons	
0.3	0.873 ± 0.007	0.038 ± 0.007	1.23
0.9	0.843 ± 0.008	0.058 ± 0.008	4.68
1.5	0.780 ± 0.008	0.115 ± 0.007	2.60
2.1	0.863 ± 0.005	0.0816 ± 0.0035	21.2
2.7	0.845 ± 0.005	0.0843 ± 0.0037	23.4
		Pions	
0.3	0.748 ± 0.010	0.087 ± 0.008	7.48
0.9	0.702 ± 0.011	0.114 ± 0.008	5.53
1.5	0.771 ± 0.011	0.087 ± 0.008	5.85
2.1	0.867 ± 0.010	0.061 ± 0.007	1.27
2.7	0.965 ± 0.011	0.040 ± 0.008	3.13

Table 6.3

Parameters for Fits to Single-Particle Energy Response in the Monte Carlo R=0.7 Cone Imposed

η	A	B	χ^2
		Electrons	
2.7	0.821 ± 0.007	0.0988 ± 0.0035	40.2
		Pions	
0.3	0.730 ± 0.012	0.101 ± 0.009	2.35
0.9	0.664 ± 0.014	0.135 ± 0.010	1.29
1.5	0.733 ± 0.013	0.104 ± 0.009	3.58
2.1	0.792 ± 0.011	0.087 ± 0.008	3.42
2.7	0.768 ± 0.012	0.088 ± 0.009	5.69

Table 6.4

Parameters for Fits to Single-Particle Transverse Energy Response in the Monte Carlo R=0.7 Cone Imposed

η	A	B	χ^2
		Electrons	
2.7	0.834 ± 0.005	0.0912 ± 0.0037	30.4
		Pions	
0.3	0.730 ± 0.012	0.101 ± 0.009	2.48
0.9	0.668 ± 0.014	0.134 ± 0.010	1.28
1.5	0.741 ± 0.013	0.102 ± 0.010	3.69
2.1	0.817 ± 0.011	0.077 ± 0.008	2.47
2.7	0.819 ± 0.012	0.072 ± 0.009	8.99

6.1.3 Response of the Test Beam Data

The test beam data used in this jet analysis were from D-Zero's 1991 single particle beam tests [80]. This run was similar to that of 1990, as described in Chapter 4, except that these studies involved tests of the transition region between the central calorimeter and end calorimeter, including the inter-cryostat detector (ICD), as shown in Fig 6.9. (The inter-cryostat detector is an array of scintillating tiles that is used to measure energy deposition between the cryostats of the central and end calorimeter.) In the 1991 test beam, a fraction of time was devoted to studying the response of the calorimeter to low energy ($< 10GeV$) particles [80]. We used preliminary data from these low energy runs to determine the single-particle response of the calorimeter. These data sets consist of $\approx$ 10,000 electron and 1000-5000 pion events at each of three values of η= 0.05, 0.45 and 1.05, and several energy settings between 1 and 10 GeV. The data were corrected for pedestal fluctuations and gain variations, as was done for the data from the 1990 run of the test beam. For electrons, all the energy in the CCEM and CCFH layer 1, contained in a 5 $\times$ 5 array of towers of 0.1 $\times$ 0.1 in $\eta \times \phi$, centered at the the impact position of the particle, was summed to calculate the reconstructed energy. For pions, a 10 $\times$ 10 array of towers in CCEM, CCFH, and CCCH (as well as ECMH, ECOH, ICD and "massless" gaps (CCMG and ECMG) for $\eta = 1.05$) was summed. (Massless gaps are calorimeter readout gaps without absorber material that are mounted on the end plates of the CCFH and ECMH modules, and are used to measure energy flow in the region between the central and end cryostats.) A 10 $\times$ 10 array of towers is equivalent to a typical cone of radius R=0.7.

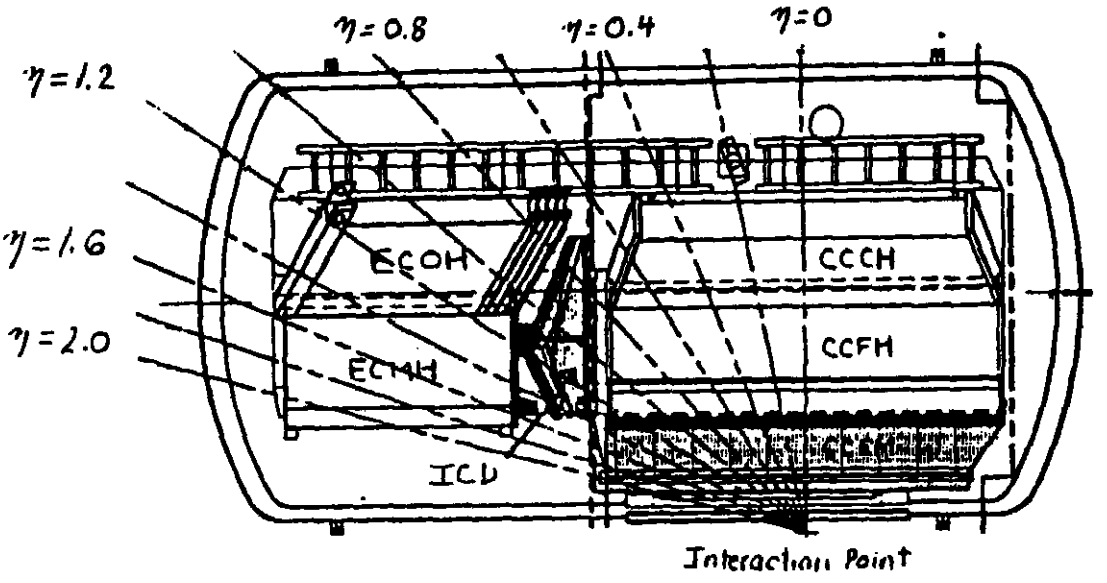

Figure 6.9 The arrangement of calorimeter modules in the 1991 test beam.

The response of the preliminary data was also fitted to the form $R_E(E) = A + B\log_{10}(E)$, at three values of η. The parameters from these fits and the χ^2s per degree of freedom are listed in Table 6.5. The fits to the single-particle response for the Monte Carlo results at $|\eta| = 0.3$, using a cone of R=0.7, and for the test-beam data at $\eta = .45$, for both pions and electrons, are shown in Fig. 6.10. The fits to the Monte Carlo and to the data differ for several reasons. First, because the calibration of the calorimeter is still not fully established, the response for the test beam data has been normalized assuming that the ratio $R_E = 1$ for 50 GeV electrons at $\eta = 0.05$. In the Monte Carlo simulation, $R_E = 0.92$ for 50 GeV electrons in the region centered at $|\eta| = 0.3$, and so the data response should be reduced by $\approx 8\%$ to compare it with the Monte Carlo. Another important difference, is that the test-beam

data were not averaged over all values of ϕ. The results, therefore, do not take into account energy lost in the ϕ cracks between the modules of the central calorimeter. It was observed in the Monte Carlo that, independent of energy, a small fraction of the electrons, lose a large percentage of their energy in cracks between CCEM modules, this percentage being larger for high energy electrons. This would contribute to the response in the Monte Carlo not being as steep as that seen in the data.

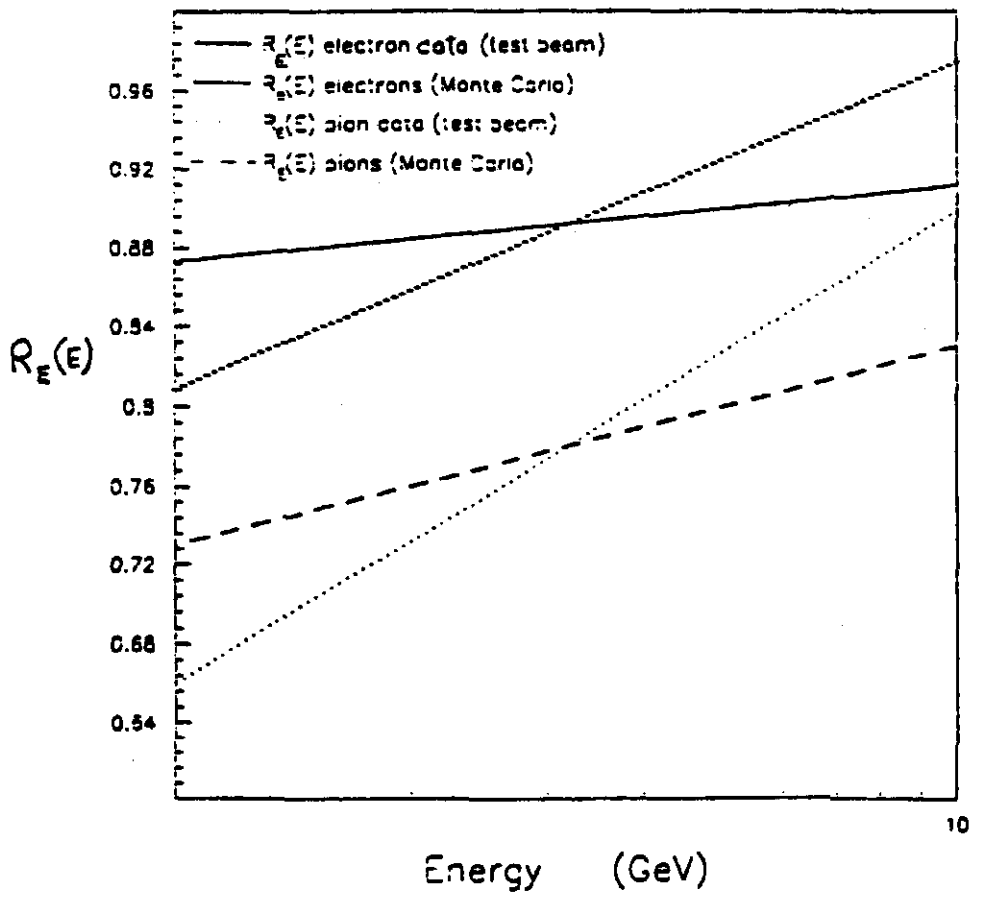

Figure 6.10 Fits to the ratios $R_E(E)$ for the Monte Carlo events at $|\eta| = 0.3$, and for test-beam data at $\eta = .45$, for both pions and electrons.

Table 6.5

Parameters for Fits to Single-Particle Energy Response in the Test Beam

η	A	B	χ^2
		Electrons	
0.05	0.8206 ± 0.0024	0.16634 ± 0.00002	9.9
0.45	0.8089 ± 0.0021	0.18000 ± 0.00016	20.7
1.05	0.6783 ± 0.0026	0.25603 ± 0.00001	18.8
		Pions	
0.05	0.561 ± 0.010	0.3735 ± 0.0002	0.84
0.45	0.660 ± 0.007	0.23952 ± 0.00001	4.8
1.05	0.11 ± 0.10	0.73 ± 0.09	.02

6.2 Single Particle Content of Jets

The single-particle content of simulated jets, reflecting the jet fragmentation function, was determined by analyzing jets generated using the ISAJET event generator. The simulation consisted of a 5000-event run, with jets evenly distributed over all angles in ϕ and η. For each run, the jet of highest transverse energy (E_T) in each event had a E_T between 45 and 55 GeV. The invariant single-particle content, E dN/dE, where N is the number of fragment particles in the jet and E is the particle energy, for each of the five chosen $|\eta|$ ranges ($|\eta|$= 0.0-0.6, 0.6-1.2, 1.2-1.8, 1.8-2.4, 2.4-3.0) is plotted as a function of particle energy in Figs. 6.11 and 6.12, respectively for electromagnetically

and hadronically interacting fragment particles. The electromagnetically interacting particles consisted of photons, electrons, π^0's and η's. All other fragment particles were labeled hadronic. These fragment distributions were fitted to the form $EdN/dE = \exp(C + DE)$. The fits are also shown in Figs. 6.11 and 6.12. The resultant fit parameters are listed in Table 6.6. The fits are quite good with χ^2's per degree of freedom of 1 ± 0.2. The fraction of the jet energy that is carried by particles that interact electromagnetically and the fraction that is carried by those that interact hadronically is listed in the second column of Table 6.6 for each η region.

6.3 Jet Energy Response

The calorimeter response to jets of 50 GeV in E_T, $R_J(\eta)$, was estimated as a function of η, by combining the single-particle responses $R_E(E,\eta)$, required in the jet fragmentation at any value of η. This combination of the separate responses corresponds to just a sum of convolutions of the two functions:

$$R_J(\eta) = F_{EM} \int R_E(E,\eta)_{EM}(EdN/dE)_{EM}\ dE \Big/ \int (EdN/dE)_{EM}\ dE$$

$$+F_{HAD} \int R_E(E,\eta)_{HAD}(EdN/dE)_{HAD}\ dE \Big/ \int (EdN/dE)_{HAD}\ dE \quad (6.5)$$

where $R_E(E,\eta)_{EM}$ is the electron energy response in the given η region, $R_E(E,\eta)_{HAD}$ is the pion energy response, E dN/dE is the corresponding jet particle content for that particle type, and $F_{EM/HAD}$ is the fraction of the jet's energy carried by that type particle. $R_{J_T}(\eta)$ is of the same form with $R_{E_T}(E,\eta)$ substituted for $R_E(E,\eta)$. The values of $R_E(E,\eta)$ and $R_{E_T}(E,\eta)$ below 1 GeV were assumed to remain constant equaling the value of the

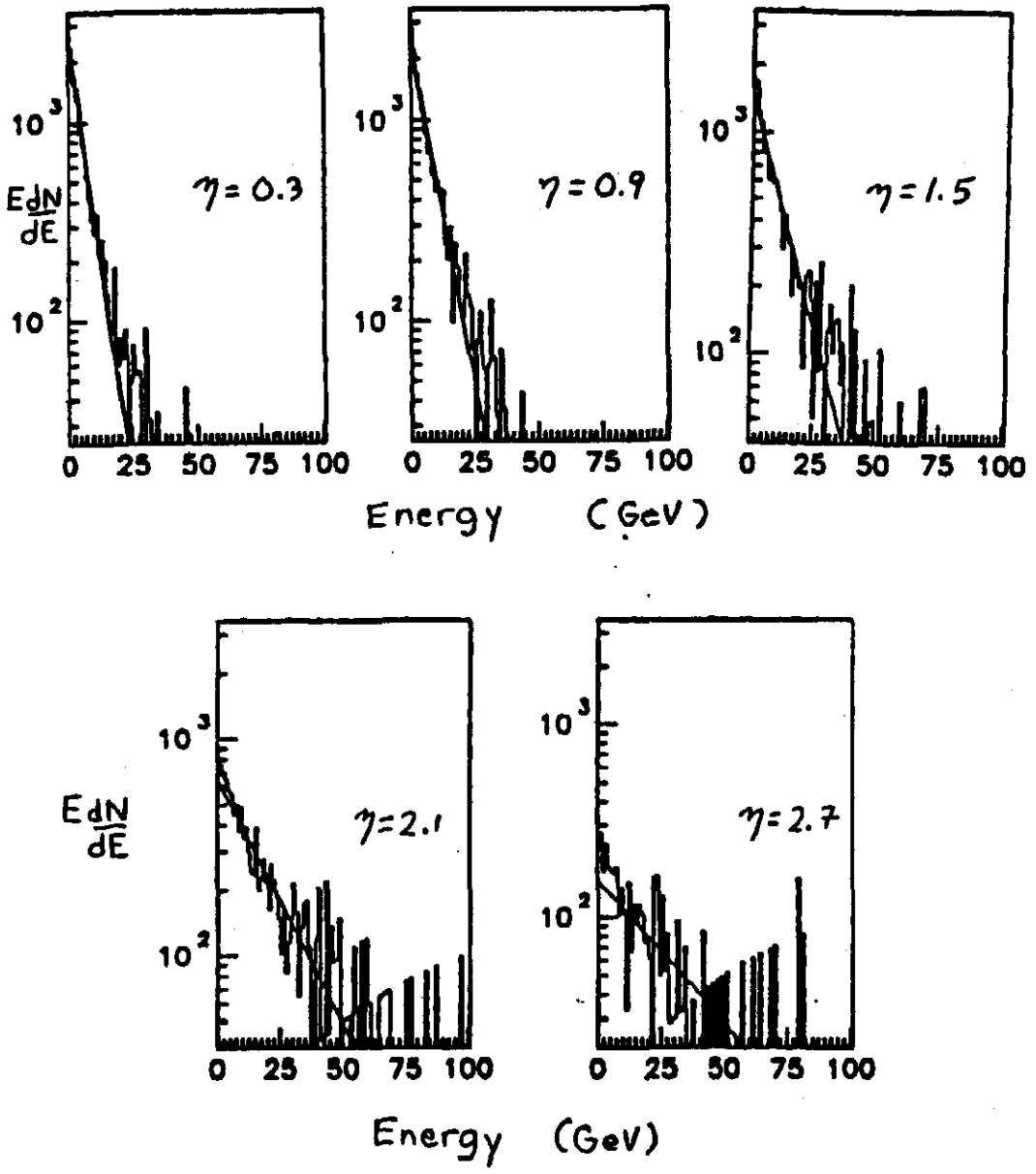

Figure 6.11 Fragments of jets and fits to the inclusive single-particle content (E dN/dE) for electromagnetic particles fragmenting from 50 GeV E_T jets in five pseudorapidity regions.

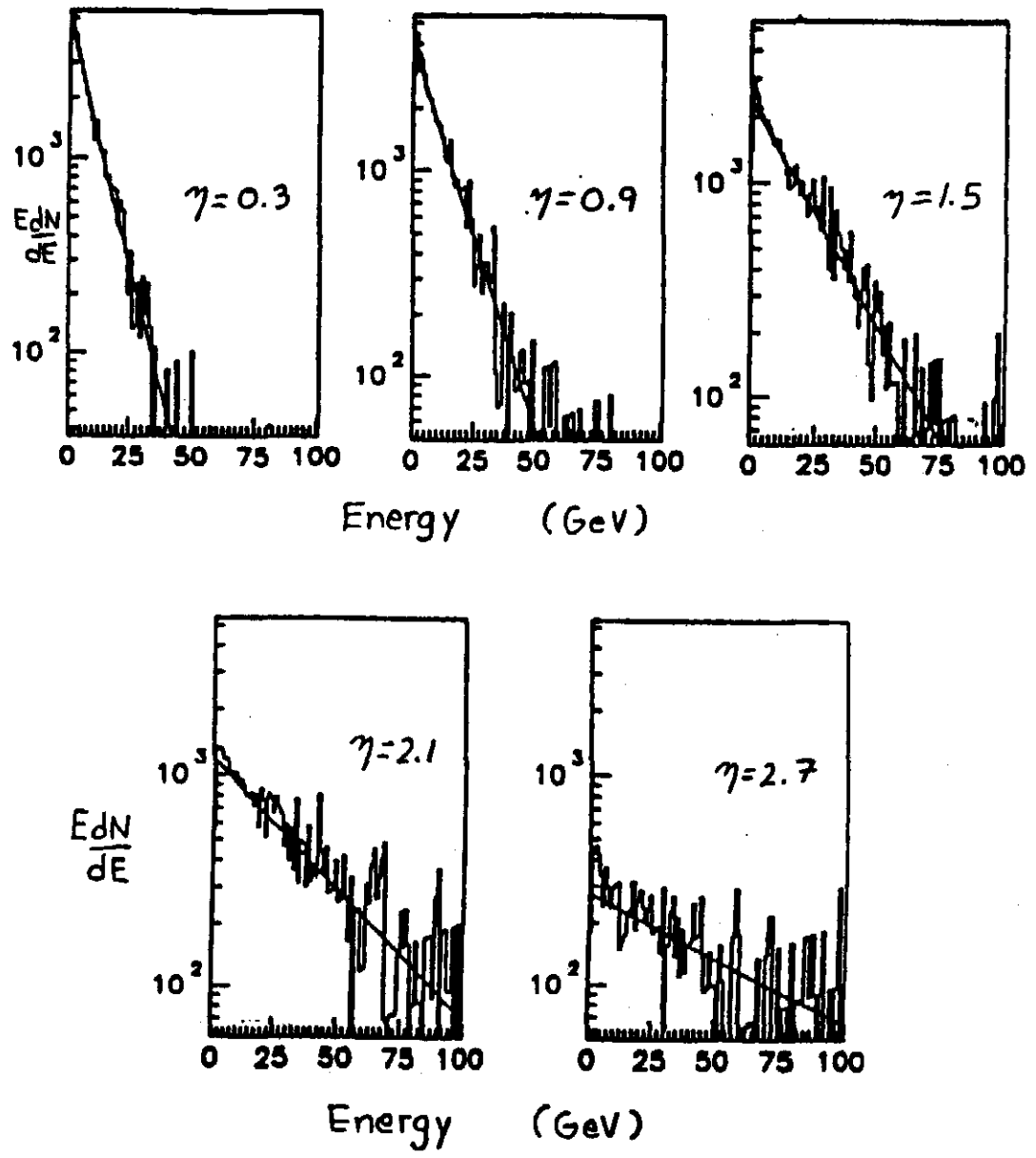

Figure 6.12 Fragments of jets and fits to the inclusive single-particle content (E dN/dE) for hadronic particles fragmenting from 50 GeV E_T jets in five pseudorapidity regions.

Table 6.6

Parameters for Fits to Single-Particle Content of Jets (E dN/dE) from ISAJET

$$EdN/dE = \exp(C + D(E))$$

η	Energy Fraction	C	D
		Electromagnetic	
0.3	0.249	7.97 ± 0.01	-0.209 ± 0.002
0.9	0.250	7.78 ± 0.01	-0.156 ± 0.002
1.5	0.238	7.25 ± 0.01	-0.095 ± 0.001
2.1	0.239	6.47 ± 0.01	-0.052 ± 0.001
2.7	0.235	5.04 ± 0.03	-0.034 ± 0.001
		Hadronic	
0.3	0.751	8.54 ± 0.01	-0.116 ± 0.006
0.9	0.750	8.30 ± 0.01	-0.085 ± 0.004
1.5	0.762	7.80 ± 0.01	-0.049 ± 0.002
2.1	0.761	7.08 ± 0.01	-0.028 ± 0.002
2.7	0.765	5.62 ± 0.02	-0.014 ± 0.004

ratio at 1 GeV. We assumed that all electromagnetically interacting particles behave like electrons and all hadronically interacting particles behave like pions.

The results using the single-particle responses from the Monte Carlo simulation are shown in Fig. 6.13. $R_{JMC}(\eta)$ and $R_{JMC_T}(\eta)$ calculated from single-particle response functions, with and without an imposed cone requirement, are plotted as a function of $|\eta|$. As expected, there is less energy reconstructed when the cone requirement is imposed, and the effect is largest for $R_{JMC_T}(\eta)$ in the $|\eta| = 2.7$ region.

A comparison of the jet energy response derived from the Monte Carlo single particle response and the response for simulated jets interacting directly in the calorimeter will provide information about which aspects of the response can be determined from the single particle response. The result for $R_{JMC_T}(\eta)$ is compared in Fig 6.14 with the transverse energy response found for 50 GeV E_T jets created using ISAJET, and run through the same Monte Carlo simulation $R_{JD_T}(\eta)$. R_{JMC_T}, with a cone imposed, accurately models the eta dependence of R_{JD_T}, but its overall value is about 7% larger. This implies that the calculated response does not take into account all the factors that affect the jet energy response. One factor not taken into account is the fact that the single particles we used were centered within the imposed cone, while in a jet they would not be centered, and therefore more energy would be deposited outside of the cone. In our simulation, there were no nearby jets created by ISAJET and therefore no energy from them was deposited in the measured jet's cone, and there was no merging of closely spaced jets.

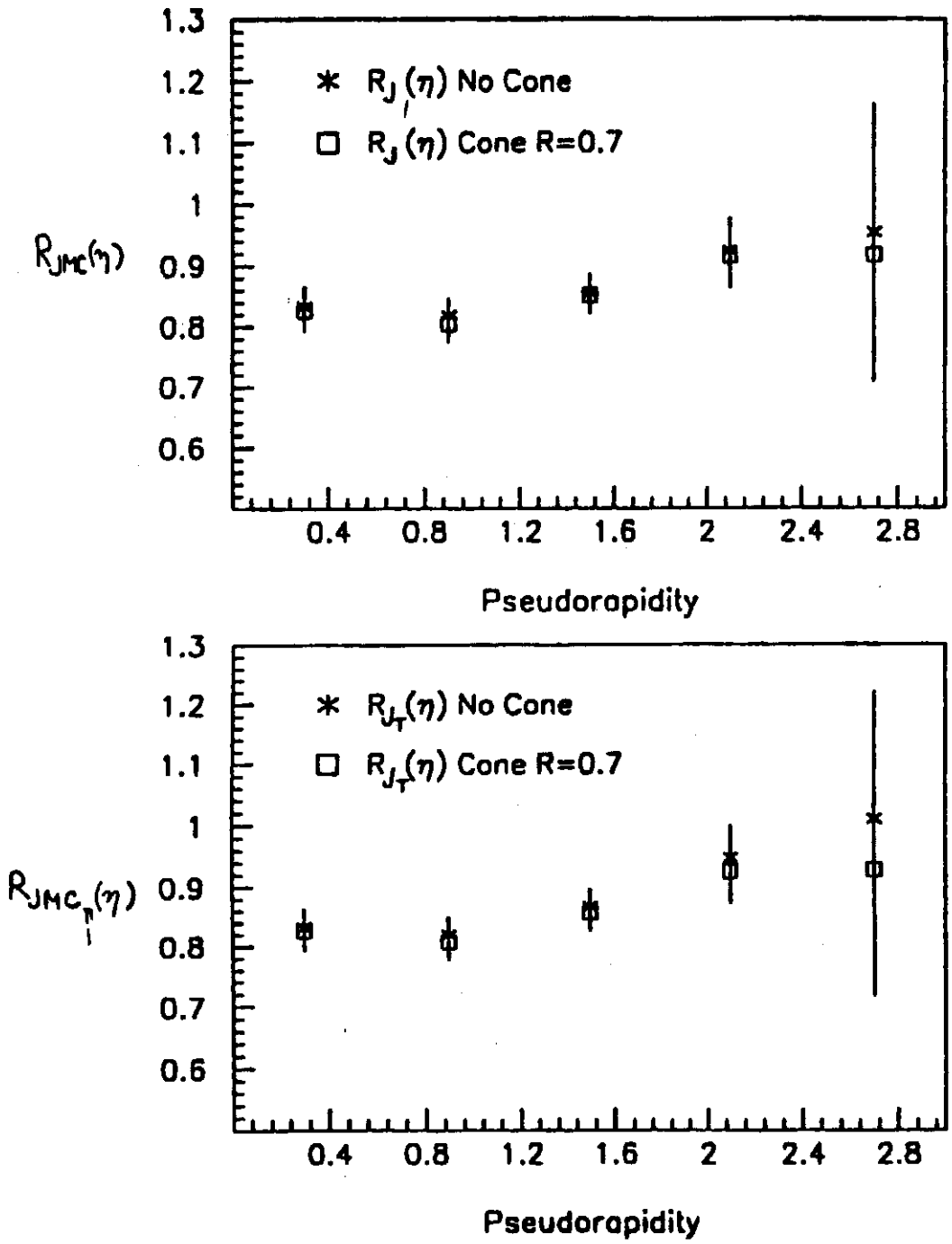

Figure 6.13 R_{JMC} and R_{JMC_T} as a function of $|\eta|$, with and without an imposed cone requirement.

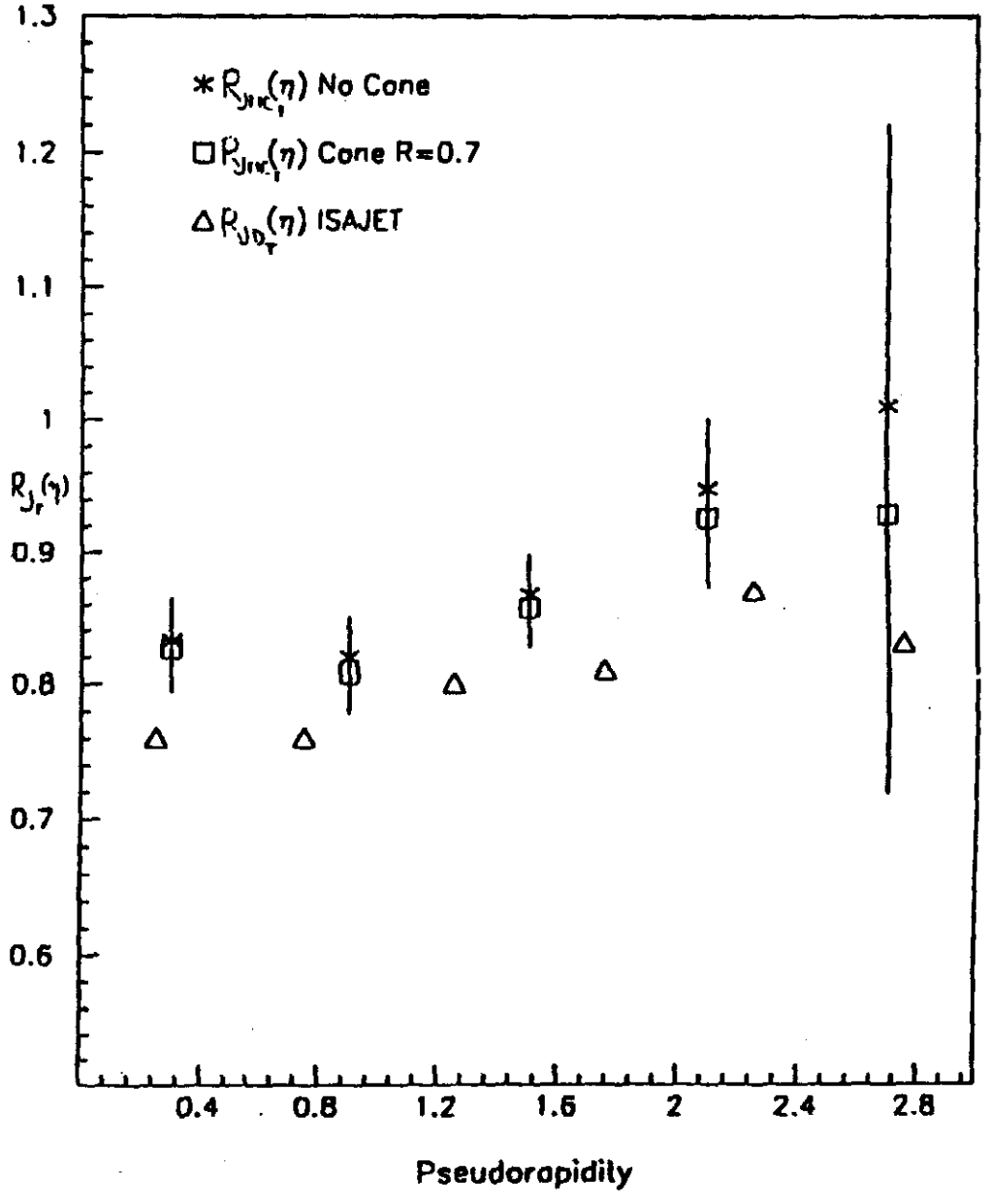

Figure 6.14 A comparison of the calculated jet transverse energy response in the Monte Carlo with that measured for jets created by ISAJET.

There should be little effect due to uncertainty in the fragmentation since the same version of ISAJET was used to determine E dN/dE for the calculation of R_{JMC_T} and to determine R_{JD_T}.

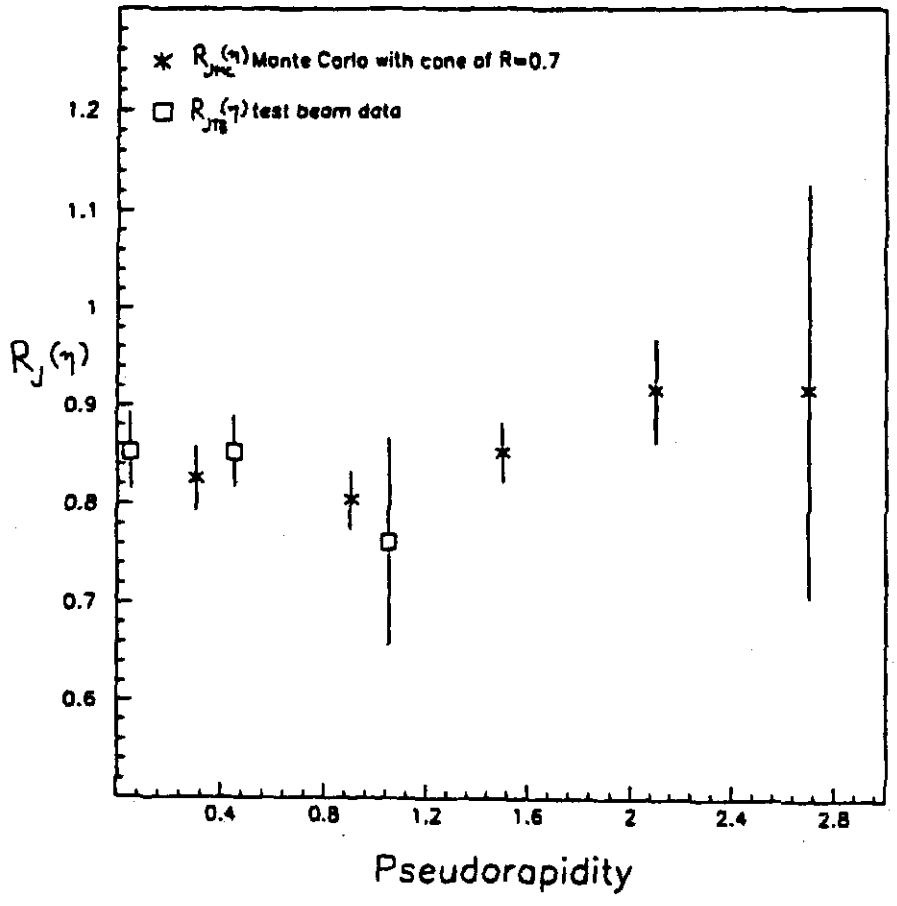

Figure 6.15 A comparison of the jet energy response calculated from the test-beam single particle response with the response calculated from the Monte Carlo.

The energy response of jets calculated using the results from the test beam, R_{JTB}, is plotted in Fig. 6.15. Also shown is R_{JMC} with a cone R=0.7 imposed. A comparison of the two shows the effects the underlying single

particle response has on the jet energy response. R_{JTB} exceeds R_{JMC} by a few percent, as might have been expected from the single particle response observed in Fig 6.10. The drop in response at $\eta = 1.05$ can be attributed to energy losses in the region between the central and end cryostats which are not corrected properly by the ICD and massless gaps. The ICD and massless gaps response in the Monte Carlo simulation has not yet been tuned to the response seen in the test beam.

This type of study provides information on how to improve the jet energy response in D-Zero. Because ECEM and ECIH modules were not exposed to the low-energy test beam, the Monte Carlo simulation, with noise added from the electronics, will have to be tuned to match the test beam studies at high energy and the results at low energy for the central calorimeter. The low energy response of the end calorimeter will then have to be extracted from this tuned simulation. The array of towers summed to calculate the reconstructed energy should be equivalent to a cone size of R=0.7 to correctly model the transverse energy bias at large values of $|\eta|$.

It has been noted that different fragmentation models, used in different event generators, provide jet energy responses that vary by as much as 5% for a cone size of R=0.7 [81]. Therefore, in comparing data to models, the choice of the jet fragmentation scheme used is also important. In D-Zero, the details of jet fragmentation cannot be measured because there is no central magnetic field to determine the charge and momentum of individual charged particles. General properties of jets that are related to the fragmentation can however be measured by the calorimeter. The jet fragmentation measured by CDF at

the appropriate value of q^2 should also be a useful guide. A convolution of the chosen jet particle content and the single-particle response from the test beam should then provide a good prediction of the collider energy response for an isolated jet.

Effects due to energy spill-over from nearby jets, energy from partons that did not participate in the hard scattering process (beam and target jets), and energy deposited outside the jet cone can be estimated using collider data [75]. Such effects can be used to correct the isolated jet energy response, and thereby extract the jet energy response seen in the D-Zero detector. This response can then be used to correct the observed jet energies so that the energy dependence of the jet cross sections can be accurately determined and compared to predictions of QCD.

CHAPTER 7

CONCLUSIONS

7.1 Shower Shapes and Position Resolution

This dissertation contains a thorough analysis of the shapes of particle showers and the position resolution obtained in the D-Zero end calorimeter. The longitudinal and transverse shapes of the electromagnetic showers agree with expectations and with Monte Carlo simulations. Two methods provide comparable accuracy for determining positions of the energy centroids of electromagnetic showers. These are the corrected-center-of-gravity method (Eq. (5.8)) and a method employing the measured transverse shower profile (Eq. (5.9)). For the first method, optimizing the readout thresholds and the width parameters of showers improved the spatial resolution. The relative insensitivity to the values of the optimum thresholds indicates that the tails of the transverse shower distributions can be ignored in calculating the shower centroids. The energy dependence of the position resolution was of the form $\sigma(r \cdot \phi) = (17.9 \pm 0.4)E^{-0.685 \pm 0.005}$ mm, which is not far from the expected $E^{-1/2}$ dependence. The dependence of the position resolution on the angle of incidence is consistent with expectation for the geometry of the calorimeter modules.

The observed longitudinal development of hadronic showers agreed well

with the general parametrization of Bock et. al. The transverse profile was found to be fitted best by the sum of two modified Lorentzians. Both the transverse and longitudinal shower shapes agreed with the shapes observed in the Monte Carlo. Many different methods were investigated for determining the positions of the centroids of hadronic showers. Best results were obtained when all layers of the ECEM and ECIH calorimeter modules were included in a center-of-gravity type of calculation, and specific weights were used for each of the summed calorimeter towers. The tower weights that provided best resolutions were proportional to the energies for the ϕ coordinate, and to logarithms of the energies for the r coordinate. The magnitudes of the optimized thresholds for hadrons also indicated that the tails of the transverse energy distributions could be ignored in calculations of position, as was the case for electromagnetic showers. Because of shower fluctuations in the development of hadronic showers, methods for determining shower centers that involved fits to the average shower shape in each layer of the calorimeter gave considerably worse results than center-of-gravity methods. The energy dependence of the hadronic position resolution was $\sigma(r \cdot \phi) = (54.9 \pm 1.3)E^{-0.551 \pm 0.005}$ mm and $\sigma(r) = (49.4 \pm 1.9)E^{-0.502 \pm 0.008}$ mm. These results agree with general expectations. The dependence on angle of incidence is also as expected. However, the energy dependence of the position resolution in the current D-Zero Monte Carlo does not follow the idealized $E^{-1/2}$ behavior. This suggests that the fluctuations in hadronic showers are not handled properly as yet in the Monte Carlo.

Several of the results reported in this thesis have already been published (See references [52],[44]), and other aspects are still being developed for use

in the D-Zero collider program. A logarithmic weighting scheme is currently being used to determine the position of electromagnetic shower centroids. Information on pion separation, extracted from the transverse hadronic shower profiles, is being used in the design of detectors for the planned upgrade of D-Zero.

7.2 Jet Energy Response

The second part of the analysis in this thesis involved determining the energy response of the D-Zero calorimeter to hadronic jets. The energy scale for jets can be estimated from a sum of the energy response of the calorimeter to single electrons and single pions, convoluted with the particle content of jets. It was discovered that using the standard calculation of the transverse energy in a shower, namely $E_{TR} = \sum_i E_i \sin\theta_i$ leads to a bias towards higher E_T for pion showers, especially at large values of pseudorapidity. The transverse energy of jets calculated by summing simulated single particle spectra, with jet cones of R=0.7, reproduced the energy dependence for jets generated in the calorimeter using ISAJET. The calculated overall calorimeter response is about 7% high because energy deposited outside of the cone was not taken into proper account. The calorimeter's energy response to jets, calculated using single particle spectra from the test beam differed somewhat from that using purely Monte Carlo. To use the test beam as input for calculating the jet energy expected in the collider environment, the following corrections will have to be implemented:

1) The Monte Carlo will have to be tuned to match the 1990 and 1991 test beam data in order to determine the low-energy response of the end

calorimeter.

2) Because the particle content of jets cannot be measured directly in D-Zero, a reliable simulation will have to be formulated that best models the fragmentation of jets.

3) The effects due to energy sharing between nearby jets, energy leakage from the underlying event (spectator constituents), and energy deposited outside the jet cone must be measured in each event.

The resulting calculated jet energy should then provide an accurate description of the dynamics of the collision and lead to the determination of the character of the interactions among constituents. The corrections we have found in this thesis provide a first step towards that goal.

Our analysis indicates the first-order corrections that must be applied to reconstructed jets in order to compare the cross section with phenomenology. A similar method to the one described is currently being used to determine jet energy non-linearities and resolution in D-Zero collider data. Further analyses are currently being undertaken to better understand the low energy response of the calorimeter [80] and the effects of jet energy uncertainties on measuring the jet cross section [74].

REFERENCES

[1] F. Dydak, Proceedings of the XXV International Conference on High Energy Physics, Singapore (1990)

[2] E. Eichten *et al.*, Supercollider Physics, Rev. Mod. Phys. **56**, (1984) 579.

[3] F. Abe *et al.*, Phys. Rev. Lett. **62** (1989) 1825.

[4] A. Clark, "Experimental Aspects of Hadron Collider Physics", Techniques and Concepts of High Energy Physics VI, edited by T. Ferbel, (Plenum Press, 1991) 71.

[5] R. K. Ellis, N. J. Stirling, "QCD and Collider Physics", Proceedings of the 1988 CERN School of Physics, CERN 91-01 (1991) 135.

[6] D. Green, FNAL Collider Physics on an Abacus, FN-433 2020.000, June 1986.

[7] M. Shapiro, Proceedings of the 17th SLAC Summer Institute, SLAC-PUB-5219 (1990).

[8] S. Ellis, Z. Kunszt and D. Soper, Phys. Rev. Lett. **64** (1990) 2121.

[9] J. Morfin, Fermilab preprint, Fermilab-Conf-90/155 (1990).

[10] UA1 Collaboration, G. Arnison *et al.*, Phys. Lett. **B177** (1986), 244.

[11] UA2 Collaboration, J. Appel *et al.*, Z. Phys. **C30** (1986), 341.

[12] G. Fogli *et al.*, Z. Phys. **C40** (1988) 379.

[13] ALEPH Collaboration, D. Decamp *et al.*, Phys. Lett. **B236** (1990) 511,

DELPHI Collaboration, P. Abreu *et al.*, Phys. Lett. **B242** (1990) 536,

OPAL Collaboration, M. Akrawy *et al.*, Phys. Lett. **B236** (1990) 364.

[14] H. Georgi *et al.*, Phys. Rev. Lett. **40** (1978) 692.

[15] UA1 Collaboration, G. Arnison *et al.*, Phys. Lett. **B147** (1984), 241.

[16] UA2 Collaboration, P. Bagnaia *et al.*, Phys. Lett. **B129** (1983), 130.

[17] L. Pondrom, Proceedings of the 15th International Conference on High Energy Physics, Singapore (1990)

[18] A.R. Clark *et al.*, Nucl. Inst. & Meth. **A315** (1992) 193.

[19] A. Zylberstein, "The Transistion radiation Detector for the D-Zero Experiment", Proceedings of the 7th Annual Conference on Proton-Antiproton Physics, Fermilab (1988)

[20] T. Behnke, "The Central Drift Chamber for the D-Zero Experiment: Design, Construction and Test", PhD thesis, SUNY Stony Brook 1989

[21] J. Bantly, "The D0 Detector Forward Drift Chamber Performance and Physics Capability in the 1990 FNAL Testbeam Run", PhD thesis, Northwestern University 1992

[22] R. Wigmans, "Calorimetry in High Energy Physics", Techniques and Concepts of High Energy Physics VI, edited by T. Ferbel, (Plenum Press, 1991) 325.

[23] Y. S. Tsai, Rev. Mod. Phys. **46** (1974) 815.

[24] E. Storm & H.I. Israel, Nucl. Data Tables **7** (1970) 565.

[25] L. Pages *et. al.*, Atomic Data **4** (1972) 1.

[26] C. Fabjan, "Calorimetry in High Energy Physics", Experimental Techniques in High Energy Physics, edited by T. Ferbel, (Addison-Wesley, 1987) 257.

[27] E. Longo & I. Sestili, Nucl. Inst. & Meth. **128** (1975) 283.

[28] U. Amaldi, "Fluctuations in Calorimetry Measurements", Experimental Techniques in High Energy Physics, edited by T. Ferbel, (Addison- Wesley, 1987) 325.

[29] G. A. Akopdjanov *et. al.*, Nucl. Inst. & Meth. **140** (1977) 441.

[30] Y. B. Bushnin, *et. al.*, Nucl. Inst. & Meth. **106** (1973) 493.

[31] E. Gabathuler, *et. al.*, Nucl. Inst. & Meth. **157** (1978) 47.

[32] J. P. DeWulf, *et. al.*, Nucl. Inst. & Meth. **A252** (1986) 443.

[33] J. Ranft, Particle Accelerators **3** (1972) 129.

A. Baroncelli, Nucl. Inst. & Meth. **118** (1974) 445.

T. A. Gabriel, *et. al.*, Nucl. Inst. & Meth. **134** (1976) 271.

[34] R. K. Bock, *et. al.*, Nucl. Inst. & Meth. **186** (1981) 533.

[35] M. G. Catanesi, *et. al.*, Nucl. Inst. & Meth. **A260** (1987) 43.

[36] F. Binon *et. al.*, Nucl. Inst. & Meth. **188** (1981) 507.

[37] R. Wigmans, Nucl. Inst. & Meth. **A259** (1987) 389.

[38] D. Bollini *et. al.*, Nucl. Inst. & Meth. **171** (1980) 237.

[39] T. Akesson *et. al.*, Nucl. Inst. & Meth. **A262** (1987) 243.

[40] G. d'Agostini *et. al.*, Nucl. Inst. & Meth. **A274** (1989) 134.

[41] E. Bernardi *et. al.*, Nucl. Inst. & Meth. **A262** (1987) 229.

[42] D. Hitlin, "SLD Liquid Argon Prototype Tests", Proc. of the Workshop on Compensated Calorimetry, Pasadena, 1985, CALT-68-1305.

[43] A. N. Diddens, *et. al.*, Nucl. Inst. & Meth. **178** (1980) 27.

[44] H. Aihara *et al.*, "The Design, Construction and Performance of the D0 End Calorimeter Electromagnetic Module", Lawrence Berkeley Laboratory Report LBL-31378 (To be published in Nucl. Instr. & Meth.).

[45] P. Bhat *et al.*, "1990 Test Beam Performance and Studies", D0 Note 1076, Fermilab, unpublished.

[46] J. F. Bartlett, *et al.*, "The EPICS System: an Overview", Fermilab-TM-1244-fiche (1984)

[47] S. J. Durston *et al.*, "1990 Test Beam Performance Studies", D0 Note 1078, Fermilab, unpublished.

[48] M. Abolins *et al.*, Nucl. Instr. & Meth. **A280** (1989) 36.

[49] M. Tartaglia *et al.*, "1990 Test Beam Performance and Studies", D0 Note 1076, Fermilab, unpublished.

[50] CAMAC system, Atomic Energy Comission report TID-25875, Washington D.C.

[51] G.C.Blazey, "Monitoring Liquid Argon Purity at D-Zero", Proceedings of the International Conference on Calorimetry in High Energy Physics, Fermilab, Oct 1990, edited by D. Anderson *et al.* (World Scientific,1991) p 101.

[52] S. Abachi *et al.*, Beam Tests of the D-Zero Uranium Liquid Argon End Calorimeters, Fermilab-Pub-92/159, (To be published in Nucl. Instr. & Meth. A).

[53] R.D. Schamberger, Nucl. Phys. B (Proc. Suppl.) **23A** (1991) 191.

[54] M. Demarteau, "D-Zero Calorimeter Electronics Performance", Proceedings of the International Conference on Calorimetry in High Energy Physics, Fermilab, Oct 1990, edited by D. Anderson *et al.* (World Scientific,1991) p 91.

[55] P. Franzini, Nucl. Instr. & Meth. **A289** (1990) 438.

[56] V. Radeka, S. Rescia, Nucl. Instr.& Meth. **A265** (1988) 228.

[57] B. Gibbard, "Working With COOR's Configuration Files", Version 4.3, D0 internal memo COOR-CONFIGURATIONS.MEM.

[58] B. Gibbard, "'Taker' A Generic Human Interface for D-Zero Data Taking", Version 4.2, D0 internal memo TAKER.MEM.

[59] R. Brun *et al.*, "ZEBRA-KERNEL Data Management System", CERN 85-6 (1985)

[60] B. Klima and H. Prosper, "EXAMINE", D0 Note 944, Fermilab, unpublished.

[61] J. F. Bartlett *et al.*, "User Reference Manual for D0 Control Data Acquisition Services", D0 Note 866, Fermilab, unpublished.

[62] D. Norman *et al.*, "1990 Test Beam Performance and Studies", D0 Note 1077, Fermilab, unpublished.

[63] P. Franzini, "Uses and Limitations of the Test Pulse", D0 Note 750, Fermilab, unpublished.

[64] D. Owen, *et al.*, "1990 Test Beam Performance and Studies", D0 Note 1077, Fermilab, unpublished.

[65] J. Kourlas, "Comparison of Pulser and Calorimeter Signals in the D0 Electronics", D0 Notes 936,970, Fermilab, unpublished.

[66] L. Bugge, Nucl. Instr. & Meth. **A242** (1986) 228.

[67] A. Spadafora, "Derivation of Corrected Center of Gravity Method and Comments on its Application", D0 Note 1449, Fermilab, unpublished.

[68] M. Demarteau, "Electron Position Resolution in CCEM Modules", D0 Note 842, Fermilab, unpublished.

[69] F. James and M. Roos, "MINUIT - Function Minimization and Error Analysis", CERN Program Library D506, unpublished.

[70] M. De Palma, *et al.*, Nucl. Instr. & Meth. **219** (1984) 87.

[71] D. Norman, "Parametrization of the Longitudinal Development of Hadron Showers in the D0 End Calorimeter", D0 Note 1136, Fermilab, unpublished.

[72] N. Graf, "Improvements to the Calorimeter Electron Position Algorithm", D0 Note 1352, Fermilab, unpublished.

[73] T.C. Awes, *et al.*, Nucl. Instr. & Meth. **A311** (1992) 130.

[74] R. Astur, "A Study of the Ability of the D0 Detector to Measure the Single Jet Inclusive Cross Section", PhD thesis, Michigan State University 1992

[75] J. Huth, "Jet Energy Measurement: CDF Experience", Proceedings of the SSC Calorimetry Workshop, Tuscaloosa, Al (1989)

[76] F. E. Paige and S. D. Protopopescu, ISAJET event generator, Brookhaven National Laboratory, unpublished.

[77] N. Wainer, "Jet Results from CDF", Proceedings of the 25th Moriand Conference, Savoie, France, (1991)

[78] P. Draper, S. Durston and N. Amos, "Eta-dependent Effects Due to Shower Size, D0 Note 1162, Fermilab, unpublished.

[79] N. Hadley, "Jet Size", D0 Note 1037, Fermilab, unpublished.

[80] R. Hirosky, "Response of D-ZERO U-LAr Calorimeters at Low Energies and their response with Oxygen Contamination", PhD thesis, University of Rochester 1993

[81] D. May and G.C. Blazey, "The Dependence of Jet Energy Scale on Fragmentation Functions", D0 Note 1173, Fermilab, unpublished.

[82] A. Jonckheere, Proceedings of the Workshop on Detector and Event Simulation for the SSC, Argonne National Lab (1987)

[83] R. Brun, *et al.*, GEANT program manual, CERN

[84] J. Womersley, "The D-Zero Monte Carlo", Proceedings of the XXVI International Conference on High Energy Physics, Dallas (1992)

[85] W.R. Nelson, "Structure and Operation of the EGS4 Code System", Proceedings of the Conference on Monte Carlo Transport of Electrons and Photons, Erice (1987)

APPENDIX A

MONTE CARLO SIMULATIONS IN D-ZERO

Monte Carlo simulations are used by the D-Zero experiment to develop an overall understanding of the response of the apparatus to specific physics processes. These simulations are used to gauge any systematic effects, and have in the past influenced the design of the detector [82]. It is important to have an accurate simulation of the apparatus so that any observed experimental results can be interpreted properly, even when test data may not be available. One such case is the low-energy response of the ECEM and ECIH calorimeter modules. A comparison of data from test-beam studies with results from simulations can provide an understanding of the full response of the D-Zero detector.

A.1 Event Simulation

Two types of simulations are currently used at D-Zero; namely event generation and detector simulation. The most commonly used event generator program is ISAJET [76]. This program simulates proton-antiproton collisions from the stand point of QCD, and provides the user with the four-vectors of the final state partons and their fragment particles. One can set kinematic limits on the energy and production angles of the final-state partons that

result from the initial-parton hard scattering process. The fragment remnants of the proton and antiproton are also simulated, and are superimposed on to the hard-scattering in the event. The entire event's energy is rescaled at the end of the process to force energy conservation. The interaction vertex of any event is chosen from a Gaussian distribution that models that observed for collision points at the Fermilab Tevatron. In this thesis, ISAJET was used to generate 50 GeV E_T jets for the analysis of the jet-energy scale in Chapter 6.

A.2 Detector Simulations

Determining the detector response of D-Zero is the most complex and computing-limited part of the Monte Carlo simulation. Particles generated in ISAJET are tracked through a model of the detector using the CERN program GEANT [83]. GEANT contains the full geometrical configuration of the detector, and it simulates the physics processes that occur when particles interact within the detector elements. Particles interact, are degraded in energy and are tracked until their energies reach a given cut-off value, at which point all of the remaining energy is deposited at that location. The detector is modeled through volumes of material that approximate its structure. When all the details of the detector are included in the Monte Carlo simulation, GEANT requires a large amount of CPU time to track the many particles produced throughout the calorimeter [84]. A full "plate-level" simulation of the calorimeter, namely where particles are tracked through all the absorber and readout planes of the calorimeter, is therefore particularly demanding of CPU time. One solution is to model the layers of the calorimeter as if they were homogeneous blocks that contained a mixture of the appropriate mate-